Reviews in Mineralogy & Geochemistry
Vol. 89 pp. 243-292, 2023
Copyright © Mineralogical Society of America

The Structure and Evolution of the Lunar Interior

Jeffrey C. Andrews-Hanna
Lunar and Planetary Laboratory,
University of Arizona, Tucson, AZ, 85721, USA
jcahanna@arizona.edu

Renee C. Weber
Marshall Spaceflight Center
Huntsville, AL, 35808, USA

Ian Garrick-Bethell
Department of Earth and Planetary Sciences
University of California, Santa Cruz, CA, USA

Alexander J. Evans
Department of Earth, Environmental, and Planetary Sciences
Brown University, Providence, RI, 02912, USA

Walter S. Kiefer
Lunar and Planetary Institute/USRI
Houston, TX, 77058, USA

Robert E. Grimm
Southwest Research Institute
Boulder, CO, 80302, USA

James T. Keane
Division of Geological and Planetary Sciences
California Institute of Technology, Pasadena, CA, 91125, USA

Matthieu Laneuville
Earth Life Science Institute, Tokyo Institute of Technology
Tokyo, 145–0061, Japan

Yoshiaki Ishihara
National Institute for Environmental Studies
Tsukuba, Ibaraki, Japan

Shunichi Kamata
Department of Earth and Planetary Sciences
Hokkaido University, Hokkaido, Japan

Isamu Matsuyama
Lunar and Planetary Laboratory,
University of Arizona
Tucson, AZ, 85721, USA

1529-6466/23/0089-0006$10.00 (print)
1943-2666/23/0089-0006$10.00 (online)
http://dx.doi.org/10.2138/rmg.2023.89.06

1. INTRODUCTION AND OVERVIEW

The internal structure of the Moon, from surface to core, preserves a record of its evolution from accretion to present-day. The structure of the Moon is unique in the Solar System by virtue of its small core radius relative to its planetary radius, plagioclase-rich crust, and highly heterogeneous crustal distribution of heat producing elements. This bulk structure is largely a consequence of the accretion of the Moon from a circum-terrestrial impact-generated debris disk, and its subsequent differentiation from a magma ocean. However, the present-day Moon exhibits strong departures from the simple spherically symmetric stratified interior expected at the end of magma ocean crystallization. The observed structure, on scales ranging from meters to thousands of kilometers, is a result of the long and complicated evolution of the Moon, including effects of impacts, volcanism and magmatism, and tectonism. Thus, the physical structure of the Moon is intimately tied to its differentiation from a magma ocean (see Gaffney et al. 2023, this volume), the composition and evolution of its crust (see Elardo et al. 2023, this volume), its history of volcanism (see Head et al. 2023; Shearer et al. 2023, both this volume) and tectonism (see Nahm et al. 2023, this volume), and the effects of impacts of all scales (see Osinski et al. 2023, this volume).

Our understanding of the lunar structure and interior has significantly advanced over the last decade as a result of the availability of new spacecraft and Earth-based observational data, new analyses of lunar samples, and re-analyses of previously collected in-situ and orbital data. Of particular significance to the lunar structure and interior are the new gravity and topography data returned by a series of international missions. High-resolution global gravity data returned by the Gravity Recovery and Interior Laboratory (GRAIL) mission (Zuber et al. 2013), the Kaguya mission (Namiki et al. 2009), and the Chang'e 1 mission (Jianguo et al. 2010) provided enormous improvements in data quality and resolution relative to previous datasets. High-resolution topography data returned by the Lunar Orbiter Laser Altimeter (LOLA) instrument onboard the Lunar Reconnaissance Orbiter (LRO) (Smith et al. 2010), the Laser Altimeter (LALT) instrument on the Kaguya spacecraft (Araki et al. 2009), and the Laser AltiMeter (LAM) on the Chang'E-1 spacecraft (Ping et al. 2009) similarly improved upon previous datasets. Together, the GRAIL and LOLA datasets provide the highest resolution global coverage of any geophysical dataset relevant to lunar interior structure, and exceed the resolution of comparable global datasets for any object in the Solar System. New insights have also been gleamed from new subsurface radar sounding data (Ono et al. 2009), continued analyses of Apollo seismic and electromagnetic data (e.g., Weber et al. 2011; Grimm 2013), and ongoing collection and analysis of lunar laser ranging data (Williams et al. 2014). At the same time, continued analyses of lunar samples have led to new revelations regarding lunar structure, including evidence for water in the interior (e.g., Saal et al. 2008) and for a long-lived lunar dynamo (e.g., Weiss and Tikoo 2014; Wieczorek et al. 2023, this volume).

In this review, we focus on the physical structure of the lunar interior as revealed by a variety of geophysical datasets, and how this structure relates to lunar evolution. This physical structure is largely manifest as spatial variations in physical properties, including seismic velocity, density, and electrical conductivity. These variations in physical properties are in turn the results of either variations in the physical state of the materials (e.g., porosity and temperature), or variations in composition (e.g., crust vs. mantle). We first review models of the structure of the Moon after the solidification of the magma ocean, which inform our interpretations of geophysical data. We then examine the structure of the crust and upper mantle with a focus on evidence from gravity, topography, and seismic analyses, but also taking into consideration compositional constraints from surface remote sensing. Some aspects of lunar geodynamics related to specific structures are discussed along with those structures. Next, we review the structure of the deep interior, from mantle to core, as revealed by analyses of seismic, gravity, and electromagnetic data. Finally, we discuss the present thermal state and thermochemical evolution of the Moon.

2. LUNAR STRUCTURE AS A CONSEQUENCE OF THE MAGMA OCEAN

The first order structure of the Moon is an outcome of the crystallization of the lunar magma ocean and its differentiation into a core, mantle, and crust (see Gaffney et al. 2023, this volume). The details of the post-magma ocean structure of the Moon are sensitive to the assumptions regarding the composition, depth of the magma ocean (shallow or complete), and crystallization process (fractional or equilibrium), each of which is imperfectly known. Nevertheless, a suite of magma ocean crystallization models for a range of assumptions produce consistent outcomes (e.g., Snyder et al. 1992; Elkins-Tanton et al. 2011; Charlier et al. 2018).

The initial depth of the magma ocean remains poorly constrained, with models of its subsequent evolution typically considering values between 400 and 1000 km. One possible constraint on the depth of the magma ocean comes from the predicted crustal thickness in comparison with the inferred mean crustal thickness. Models of crystallization of a magma ocean lead to a predicted crustal volume of 8.2–8.9% of the volume of the magma ocean (Snyder et al. 1992; Elkins-Tanton et al. 2011). More recent work based on new experimental work results in a plagioclase crust volume that is 10% (Rapp and Draper 2018) or 12% (Charlier et al. 2018) of the magma ocean volume. Revised estimates of the mean crustal thickness of 34–43 km (Wieczorek et al. 2013) would then scale to a magma ocean thickness of 510–890 km for crustal fractions of 8.2–8.9%, or 340–606 km for crustal fractions of 10–12%. Increasing the retained interstitial liquid in the cumulates and imperfect plagioclase floatation (Elkins-Tanton et al. 2011; Rapp and Draper 2018) can both result in an increase in the required magma ocean thickness and may be able reconcile the crustal thickness with a global magma ocean. Recent experimental work has found that much thicker crusts are predicted for a dry magma ocean, and a water content of 270–1650 ppm may be required to explain the inferred crustal thickness from a magma ocean depth of 400–1000 km (Lin et al. 2017a,b). The above calculations neglect the fact that the crust is not composed entirely of pure anorthosite (Hawke 2003; Korotev et al. 2003; Ohtake et al. 2009; Yamamoto et al. 2012; Cheek et al. 2013), with a contribution from more mafic minerals in both the upper and lower crust, favoring somewhat shallower magma oceans. For a plagioclase content of 76–95% (Korotev et al. 2003; Cheek et al. 2013), the required volume of the magma ocean would be reduced by 5–24%, and the depth would be reduced by 13–44% relative to a 1000-km-deep magma ocean case.

However, complete melting of the Moon is a likely outcome of more recent models of lunar formation by a single giant impact (Canup 2012; Ćuk and Stewart 2012; Canup et al. 2020) which favor a disk of hotter ejecta in Earth orbit than predicted by previous models (Canup and Asphaug 2001; Canup 2004). Rapid accretion of the inner Moon from cooler material outside the Roche limit followed by slower addition of hotter volatile-depleted material from inside the Roche limit could result in a cooler and more volatile rich deep interior (Salmon and Canup 2014; Canup et al. 2015). Timescales of lunar formation of 100–1000 years (Salmon and Canup 2012, 2014) may also allow sufficient radiative cooling to prevent full Moon melting (Pritchard and Stevenson 2000). Depending on the nature of the Moon-forming impact (Canup 2004, 2012; Ćuk and Stewart 2012; Rufu et al. 2017), the rate of disk cooling (Salmon and Canup 2014) and the details of lunar accretion (Pritchard and Stevenson 2000; Salmon and Canup 2014), the post-magma ocean structure may have included a deep reservoir of cooler material that did not participate in the magma ocean (Solomon and Chaiken 1976; Solomon 1977). This postulated primitive deep interior may have contained water and other volatiles (Saal et al. 2008), with important implications for mantle convection and geodynamics (Evans et al. 2014). Nevertheless, it remains to be demonstrated that a solid interior is a possible outcome of current Moon formation models.

Magma ocean crystallization would first generate olivine cumulates followed by orthopyroxene cumulates (Snyder et al. 1992), or olivine and orthopyroxene mixed throughout (Elkins-Tanton et al. 2011; Lin et al. 2017a), all of which are negatively buoyant relative to

the evolving melt. After crystallization of ~68–90% of the magma ocean, plagioclase begins to crystallize and rise to the surface to generate a floatation crust (Snyder et al. 1992; Elkins-Tanton et al. 2011; Lin et al. 2017a,b). The final stages of magma ocean crystallization would have resulted in a residuum layer rich in incompatible elements such as potassium (K), rare earth elements (REE) and phosphorus (P) (ur-KREEP, where "ur" is the German prefix for "primeval"; Warren and Wasson 1979) sandwiched between the underlying dense oxides (including ilmenite) and the overlying less dense plagioclase and pyroxenes.

In their simplest form, models of magma ocean evolution predict a spherically symmetric compositionally stratified interior. However, the present-day Moon exhibits additional lateral and vertical variations in structure. Several processes have been proposed to generate these variations, both contemporaneous with and following magma ocean crystallization. The first opportunity to break the symmetry of a post-magma ocean Moon arises in the overturn of the cumulate mantle. The predicted cumulate stratigraphy is, at least in part, buoyantly unstable, and some degree of overturn and mixing is expected (Spera 1992; Hess and Parmentier 1995). Because the late-formed ilmenite-bearing cumulates have a higher bulk density than the underlying lunar interior as a whole, overturn might have first taken the form of a spherical harmonic degree one Rayleigh–Taylor instability in which the over-dense cumulates migrated toward one hemisphere while the underlying less dense interior migrated toward the opposite hemisphere, thereby attaining a lower potential energy configuration (Parmentier et al. 2002). This instability only occurs if the viscosity of the ilmenite-bearing cumulates is more than 3 orders of magnitude less than the underlying cumulates (Parmentier et al. 2002), which is supported as a possibility by experimental data on the ilmenite rheology (Dygert et al. 2016). Some mixing of the ilmenite-bearing cumulates into the deeper interior is likely required to explain the source region of the titanium-rich basalts and picritic glasses, which necessitates the presence of ilmenite in the mantle at depths of up to 500 km (Elkins-Tanton et al. 2002, 2011).

If this migration and overturn of dense ilmenite-bearing cumulates did occur, some or all of the KREEP-rich material may have been entrained, allowing for KREEP to be concentrated on the lunar nearside and/or transported to greater to depths within the mantle (Zhong et al. 2000; Parmentier et al. 2002). Furthermore, if this overturn was directed toward the sub-Earth hemisphere (either by chance, or by some unknown forcing) or a subsequent reorientation of the Moon occurred, it would provide a natural explanation for the enhanced concentration of KREEP-rich material on the lunar nearside (see Electronic Annex [EA]-6-1; Jolliff et al. 2000; Wieczorek and Phillips 2000). Alternatively, KREEP may have become concentrated within the PKT simply as a result of the accumulation of the final dregs of the magma ocean beneath the thinner nearside crust (Warren and Wasson 1979), though the reason for the crustal asymmetry remains unknown (see discussion below). Decompression melting of pyroxene-bearing cumulates during the overturn of magma ocean cumulates would provide a viable explanation for the timing and composition of early intrusions into the lunar crust (Elardo et al. 2011; Elkins-Tanton et al. 2011). The sinking, and possible later rising (Zhong et al. 2000), of ilmenite and its geodynamic implications are discussed in greater detail later in this chapter.

In summary, at the end of the magma ocean crystallization and overturn, the structure of the crust and mantle likely consisted of a plagioclase-rich crust, overlying an upper mantle dominated by olivine and orthopyroxene. The mantle would likely have been compositionally stratified, with different compositional zoning before and after overturn, possibly resulting in discrete changes in density with depth that may persist to the present. The present-day surface concentration of KREEP-rich material and Ti-rich basalts on the nearside (see EA-6-1 and EA-6-2 suggest that the late-stage magma ocean products rich in ilmenite and KREEP may have become concentrated on the nearside. This magma ocean residuum would have initially formed beneath the crust, but may have undergone a history of sinking and possibly rising driven by compositional and thermal buoyancy, respectively. Additionally, the lower

mantle may or may not contain material arising from the Moon-forming impact(s) that did not take part in the magma ocean. The consequences of magma ocean crystallization and the possible overturn of magma ocean cumulates have significant implications for all aspects of the structure and evolution of the lunar interior.

3. SHALLOW STRUCTURE: CRUST AND UPPERMOST MANTLE

The structure of the crust and uppermost mantle are constrained by an abundance of geophysical data, remote sensing observations, and lunar samples. Remote sensing data provides an important constraint on the composition of the crust both at the surface and at depth, the latter through analyses of impact craters and central peaks. Seismic data provide constraints on the thickness of the crust and vertical density structure of the crust and mantle at a small number of locations. Gravity and topography data provide the highest resolution global coverage of any geophysical dataset relevant to the structure of the crust. Given assumptions regarding the density of the crust and mantle and the mean thickness of the crust, gravity and topography data can be inverted to yield models of the thickness of the crust. Gravity can also be used to constrain lateral and vertical variations in the density of the crust (e.g., due to variations in composition or porosity), as well as the properties of discrete density anomalies embedded within the crust (e.g., igneous intrusions). Gravity and topography data additionally reveal the compensation state of the crust, with isostasy and support by the lithosphere both playing important roles. Collectively, these datasets provide a detailed view of the vertical and lateral variations in the composition, density, porosity, thickness, and compensation state of the crust over a broad range of scales (Fig. 1).

Here, we first review the bulk physical properties of the lunar crust as revealed by surface remote sensing and geophysical data. We next examine the details of the crustal structure as revealed by models derived from gravity, topography, and seismic data, including variations in the thickness, density, and porosity of the crust. Crustal structures are subdivided based on scale into global patterns that are only evident upon considering the entire planet, regional-scale structures that affect regions comparable in scale to the lunar radius, meso-scale structures that have a pronounced effect on the thickness of the crust at scales resolved by crustal thickness models, and small-scale structures embedded within the crust that affect crustal density without substantially modifying crustal thickness. Across all scales, the history of the Moon since the solidification of the magma ocean is recorded in the structure of its crust.

3.1 Bulk properties and vertical structure of the crust

3.1.1. Compositional constraints. The first clues regarding the physical structure of the crust come from remote sensing constraints on the composition of the crust and its vertical and lateral variability. This topic is explored in more detail elsewhere (see Elardo et al. 2023, this volume), but is briefly reviewed here as it provides an important constraint for the interpretation of geophysical data. To first order, the lunar crust can be subdivided into three distinct geochemical terranes (Jolliff et al. 2000): the Procellarum KREEP terrane (PKT), the feldspathic highlands terrane (FHT), and the South Pole-Aitken terrane (SPAT).

Across much of the FHT, the surface is dominated by a mixed feldspathic layer that is several kilometers (Hawke 2003) to 10 km in thickness (Yamamoto et al. 2012), which may be represented by feldspathic meteorites containing 76–89% plagioclase (Korotev et al. 2003). This mixed layer is in many places underlain by a pure anorthosite layer that is exposed in impact craters and central peaks, typically in locations associated with deeply excavating impact basins (Hawke 2003; Ohtake et al. 2009; Yamamoto et al. 2012; Cheek et al. 2013; Donaldson Hanna et al. 2014). The lower crust of either the lunar nearside or the entire Moon may consist of more mafic noritic rocks, as indicated by mixing models for the origin of the

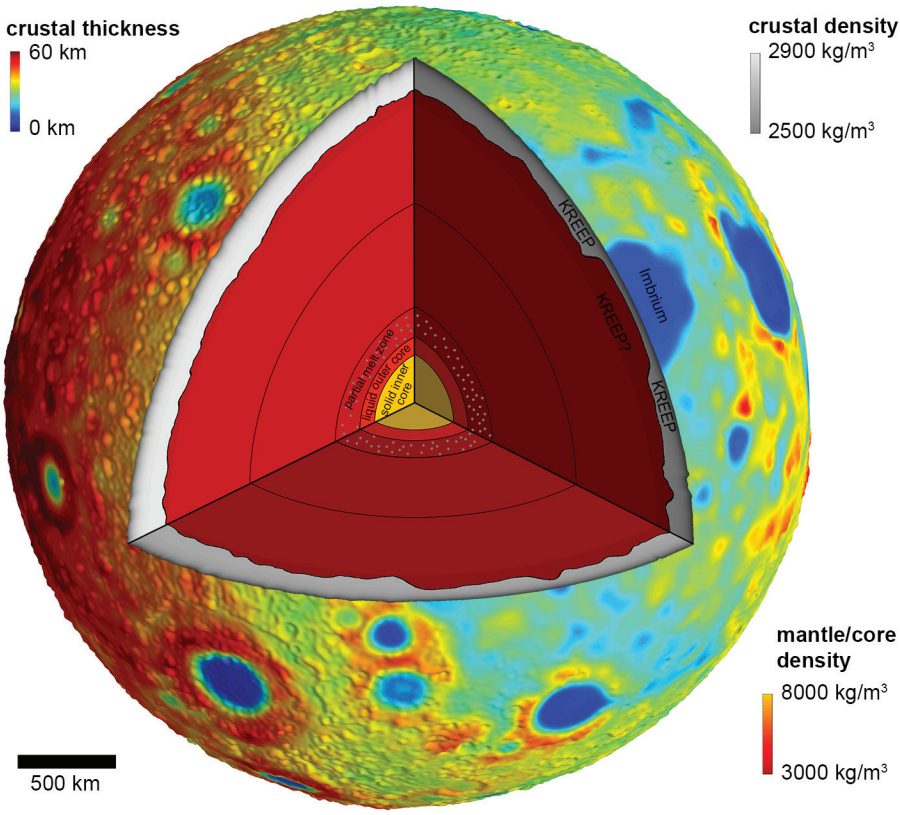

Figure 1. Schematic cross-section of the lunar interior. Surface color map shows crustal thickness (Wieczorek et al. 2013) projected onto LOLA topography for shading (Smith et al. 2010). The relief along the surface and crust–mantle interface in the cutaways is exaggerated by a factor of 5. The **grayscale coloring** of the crust shows the exponential farside density profile (Besserer et al. 2014), which is here assumed to also be representative of the sub-mare nearside crust. The **red coloring** below the crust shows the density of the mantle and core based on seismic inversions, and the **black lines** in the interior indicate seismic transitions, including a possible mid-mantle transition at a depth of 750 km (Lognonné et al. 2003; Weber et al. 2011). The **stippled shading** indicates the partial melt zone that is inferred in some studies to exist above the outer core. Globe projection is centered on 15° N, 295° E, with cutaways extending from the north pole to the equator at 250° E and 340° E, the latter passing through the Imbrium basin and Procellarum region.

low-potassium Fra Mauro formation impact melt breccias (Korotev 2000). Although central peaks of craters reveal the crust to be generally more mafic closer to the crust–mantle interface, the trend is weak and plagioclase-rich crust from great depths is also observed, arguing against a simple vertically stratified crust (Cahill et al. 2009). Instead, the lower crust may be laterally heterogeneous (Taylor and Wieczorek 2014; Martinot et al. 2018).

Several of the largest impact basins on the Moon are expected to have excavated into the upper mantle (Miljković et al. 2015). Some of the impact basins with the thinnest crust beneath their central depressions have ejecta blankets with olivine exposures (see EA-6-3), which have been interpreted as indicating an olivine-rich upper mantle following magma ocean overturn (Yamamoto et al. 2010). However, olivine is notably absent in the ejecta and on the floor of the largest impact basin: South Pole–Aitken (SPA). The formation of the 2500-km diameter SPA basin very likely excavated lunar mantle (Miljković et al. 2015; Melosh et al. 2017). The absence of olivine may indicate that this impact occurred before the overturn of the cumulate

mantle when olivine would have been less abundant (but not absent) in the uppermost mantle (Nakamura et al. 2009; Melosh et al. 2017). The absence of a clear KREEP-rich signature in the SPA ejecta outside of the basin and the low Th-concentration within the basin relative to the PKT (Jolliff et al. 2000), in contrast with the clear KREEP-rich signature of the Imbrium ejecta (Haskin 1998), suggest that the SPA-forming impact occurred either after the concentration of KREEP on the nearside (e.g., Parmentier et al. 2002), or, less likely, before KREEP had become sufficiently concentrated beneath the lunar crust during magma ocean solidification. In the former interpretation, the timing of the basin-forming impact may be constrained to be after the migration of ilmenite and KREEP to the nearside, but before overturn of the cumulate stratigraphy of the bulk of the solidified magma ocean. In contrast, a more recent analysis suggested that the elevated Th concentrations inside the rim in the northwestern part of the basin may reveal the presence of KREEP-rich ejecta derived from the upper mantle, indicating that KREEP was present below the crust at the time of the impact (Moriarty et al. 2021).

Thus, remote sensing evidence for the structure of the crust and upper mantle indicates a structure that varies vertically, with a simplified structure consisting of a several-to-10-km-thick upper mixed layer, overlying a pure anorthosite layer, and an increasingly mafic but variable crust at depth. This crust overlies an upper mantle that was the outcome of magma ocean crystallization and overturn, and may have varied in composition in both space and time. Lateral compositional heterogeneity is also observed at scales ranging from 1000-km-scale terranes to the small-scale heterogeneity of the upper mixed layer. These vertical and lateral compositional variations are likely associated with variations in physical properties, with implications for interpretations of geophysical datasets.

3.1.2. Seismic constraints. While analyses of gravity and topography data are powerful tools for analyzing spatial variations in relative crustal thickness, they are strongly dependent upon assumptions. Seismic data provide independent, and arguably more direct, local constraints on the structure of the crust, specifically the crustal thickness and vertical variations in seismic velocity at the Apollo landing sites (see reviews by Toksöz 1979; Lognonné and Mosser 1993; Lognonné and Johnson 2015; Garcia et al. 2019). Despite broad agreement in recent seismic studies, some major differences persist between models, including the thickness of the crust, the number and depth ranges of discrete layers, and the *P* and *S* velocities in those layers.

The shallow structure of the upper crust is revealed by the active seismic experiments on Apollo 14, 16, and 17 (see review by Toksöz 1979). The near-surface layers are characterized by low seismic velocities, with a ~4–12 m thick layer of unconsolidated regolith with a *P*-wave velocity of ~100 m/sec. At deeper levels, the Apollo 17 active seismic experiment was uniquely suited to examine the top several kilometers of crust owing to the long baseline between the seismic sources and the array (Cooper et al. 1974), but early analyses of this data underestimated the thickness of the upper low velocity layer due to a timing problem in the data (Nakamura 2011). Correcting for this timing error, the regolith is underlain by a zone of increasing *P*-wave velocities from 300–1000 m/sec down to >3.3 km depth (Fig. 2; Cooper et al. 1974; Toksöz 1979; Nakamura 2011), interpreted as representing the fractured and brecciated megaregolith consisting primarily of basin ejecta and heavily impact-damaged rocks. This thickness corresponds with the expected thickness of the Serenitatis ejecta blanket, which itself must have been emplaced upon some manner of ancient megaregolith. The megaregolith likely varies greatly in thickness across the Moon, largely due to the spatial variations in ejecta thickness from the large impact basins (Aggarwal and Oberbeck 1979; Warren and Rasmussen 1987; Petro and Pieters 2008). A global megaregolith of varying thickness can explain the variation in seismic coda properties from seismic sources of varying source distance and depth (Blanchette-Guertin et al. 2012). Given that the majority of the topographic relief at wavelengths at which densities can be estimated by gravity (spherical harmonic degrees >100; see below) is less than 3 km in amplitude, this low velocity and low density megaregolith layer

may feature prominently in the low densities inferred from analyses of gravity and topography data (Wieczorek et al. 2013; Besserer et al. 2014). This megaregolith layer may coincide with the mixed feldspathic layer observed in remote sensing data, though one estimate of the thickness of that compositional layer of ~10 km (Yamamoto et al. 2012) significantly exceeds the estimated thickness of the megaregolith (Petro and Pieters 2008).

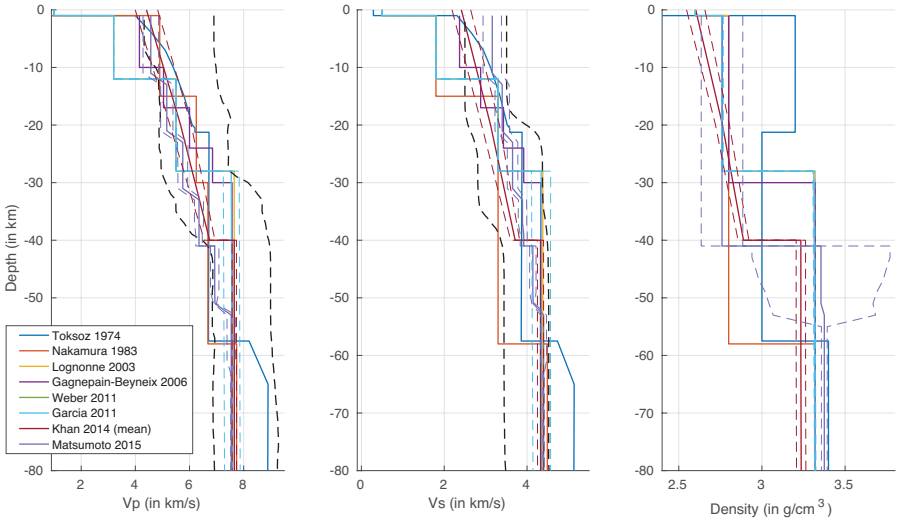

Figure 2. A comparison of multiple models for seismic *P*- and *S*-wave velocities and density through the crust and upper mantle. **Dashed lines** indicate the 1σ range, or (for the **black lines**) the 50% of the models with the highest probability density (Khan and Mosegaard 2002). [Reprinted by permission of Springer Nature, from Garcia et al. (2019) Space Sci Rev 215:50, Fig. 4, p. 13., copyright 2019]

A number of studies have supported an increase in seismic velocity through the upper crust, and a possible discrete increase in velocity at the transition to the lower crust (Fig. 2). Early analyses indicated a seismic discontinuity at 20 km depth, with higher velocities below that extending to the base of the crust at ~60 km depth (Toksöz et al. 1974; Toksöz 1975, 1979). More recent analyses (Lognonné et al. 2003; Gagnepain-Beyneix et al. 2006) support an increase in velocity at 15 km depth, with a bimodal velocity distribution between that depth and the base of the crust at 30 ± 2.5 km, possibly reflecting lateral heterogeneity associated with magmatism, impact-induced fractures, or variability in the terranes sampled by the data. Similarly, the model of Khan and Mosegaard (2002) shows an increase in velocity between 6 km and 14 km in depth, with high values persisting to the base of the crust at a somewhat deeper value of 38 km due to a higher seismic velocity. The increase in velocity with depth through the top ~15–20 km of the crust is consistent with density models based on the wavelength-dependent correlation between gravity and topography data, as discussed below (Besserer et al. 2014).

The strongest seismic constraints on the thickness of the crust come from analysis of the artificial impacts (Saturn IVB booster stages, and the lunar modules after return of the astronauts to the command modules in orbit), meteorite impacts, and moonquakes. Recent re-analysis of Apollo seismic data (Khan et al. 2000; Khan and Mosegaard 2002; Lognonné et al. 2003; Chenet et al. 2006; Fig. 2) predict a lower average crustal thickness than the original post-Apollo analyses (Toksöz et al. 1972, 1974). However, it is important to note that the inherent difficulties in reading definitive seismic arrival times from lunar data (e.g., Nakamura 2005) mean that all seismically-derived crustal thickness estimates retain some level of uncertainty, which are passed to subsequent analyses and interpretations.

Lateral variability in crustal structure as determined by seismic data is dictated by ray coverage. Rays originating in the interior (e.g., from deep moonquakes and most shallow moonquakes) only sample the crust once, and hence only constrain structure at the stations where they arrive. The four primary passive stations were deployed at the Apollo 12, 14, 15, and 16 landing sites, and data recorded by the gravimeter at Apollo 17 were later shown to have recoded deep moonquakes (Kawamura et al. 2015). Rays originating from the surface (e.g., from artificial impacts and meteorite impacts) sample the crust twice, once at the source and once at the station, and analysis of those data have been used to place a limited number of more distant constraints on crustal thickness (Chenet et al. 2006). Recent reanalysis of shallow moonquakes suggests a portion of them may have occurred at the surface, also making them potentially fitting for such analyses (see Nahm et al. 2023, this volume). Estimates based on both gravity and seismic data are the most reliable, since they rely on fundamentally different datasets and assumptions from one another. The general agreement between the crustal thickness constraints from recent independent analyses of the seismic data (Khan and Mosegaard 2002; Lognonné et al. 2003; Chenet et al. 2006), and between seismic inversions and gravity-based crustal thickness models (Chenet et al. 2006; Wieczorek et al. 2013) lends strong support to the basic results, with thicknesses at the Apollo seismic stations in the range of 30–40 km, an increase in crustal thickness toward the lunar farside as sampled by meteorite impacts, and a mean crustal thickness of ~34–43 km based on gravity models constrained by the seismic observations. The details of lateral variations in crustal thickness predicted by analyses of gravity and topography data are discussed in more detail in the following sections.

3.1.3. Gravitational constraints. The density of the crust can be measured either directly from lunar samples or indirectly from gravity data. Measured densities of a number of anorthositic rocks from the Apollo sample collection yielded densities of 2200–2840 kg/m^3 and porosities of 3–20%, with a mean bulk density of 2600 kg/m^3 and a mass-weighted mean of 2560 kg/m^3 (Kiefer et al. 2012). Density determined from gravity–topography admittance modeling using pre-GRAIL data between spherical harmonic degrees 32 and 70 for a number of areas primarily located in the farside highlands predicted higher densities, with a range of best-fit values 2640–3010 kg/m^3 likely representing deeper levels of the crust (Huang and Wieczorek 2012). High-resolution GRAIL gravity models revealed a strong correlation between gravity and topography beyond degree ~100 (Zuber et al. 2013), allowing precise determination of the density of the upper crust. The average bulk density of the lunar highlands between spherical harmonic degrees 150 and 310, corresponding to half-wavelength resolutions of 36 km to 18 km, was found to be 2550 kg/m^3, leading to an average porosity of 12% based on remote sensing constraints on the mineral grain density (Wieczorek et al. 2013). At higher degrees, the average surface density and porosity of the farside highlands are 2320 ± 60 kg/m^3 and 20 ± 2%, respectively (Goossens et al. 2020). The surface densities determined from topography and gravity data over scales <10 km are somewhat lower than measured for lunar rocks (Kiefer et al. 2012), supporting the presence of a high porosity megaregolith layer, while densities at longer wavelengths are comparable to the measured rock densities indicating that the bulk of the upper crust is comprised of fractured and brecciated, yet largely competent, rock. This inference is consistent with interpretations of lunar seismic data as supporting a megaregolith layer overlying the fractured crust (Toksöz et al. 1974; Rasmussen and Warren 1985).

The variation of the best-fit effective density as a function of spherical harmonic degree (Fig. 3) can be explained by models in which the density increases and porosity decreases with depth (Fig. 1; Besserer et al. 2014; Han et al. 2014; Goossens et al. 2020). The vertical variation of density depends on model assumptions regarding the dependency (linear or exponential) of porosity on depth. Analyses yield linear density gradients in the range of 10–40 kg/m^3/km (Besserer et al. 2014) or 27 ± 11 kg/m^3/km (Goossens et al. 2020). Alternatively, porosity can be represented with *e*-folding depths of 15–25 km (Besserer et al. 2014) or 17 ± 15 km

(Goossens et al. 2020) within the non-SPA farside highlands, though a wide range in depth scales are permissible (Han et al. 2014). These results suggest an increase in density with depth that extends through the mixed feldspathic layer and into the underlying pure anorthosite (Yamamoto et al. 2012). Given that average grain densities should decrease across this transition, this supports decreasing porosity as the cause of the gravity signature.

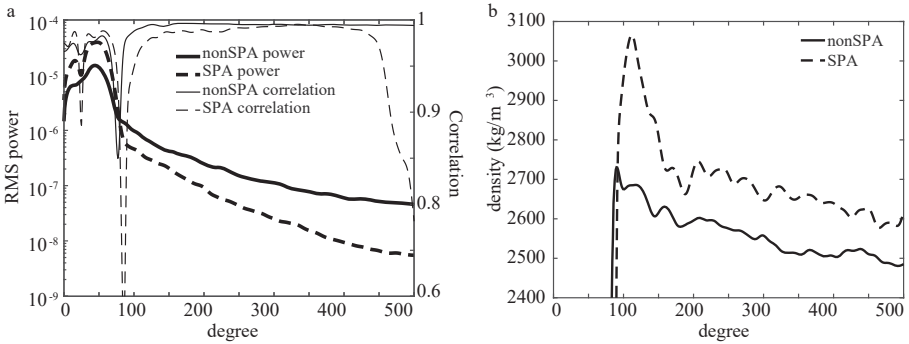

Figure 3. a Localized power spectra and correlation for the farside highlands outside of the South Pole-Aitken basin (20° cap centered on 45° N 200° E) and for the South Pole-Aitken basin (20° radius spherical cap centered on 55° S 190° E). **b** Effective density spectra over the farside highlands and South Pole-Aitken basin. Localizations were carried out to maximum spherical harmonic degree of 600, using 10 optimally concentrated tapers with a bandwidth of 98. The differences in the power spectra for the farside highlands and South Pole-Aitken basin result from differences in both density and elevation.

The GRAIL-derived density and porosity models are broadly consistent with the increase in seismic velocity through the crust, but the gravity data are not able to uniquely resolve a discrete step at the base of the megaregolith as inferred in seismic velocity models (Toksöz 1979; Khan and Mosegaard 2002; Lognonné et al. 2003). The correlation between the low density upper crust and the mixed feldspathic layer overlying the pure anorthosite at mid-crustal depths may be explained by the extensive impact damage suffered by the crust during an early period of declining bombardment (Morbidelli et al. 2012) while the magma ocean was capped by a thin plagioclase floatation crust. Impact excavation into the underlying magma ocean, combined with the brecciation and impact-induced churning of the thin forming crust would continue until either the bombardment rate dropped or the base of the thickening crust dropped below the mean level of impact excavation and damage. Alternatively, the low density mixed feldspathic layer may be explained by a global blanket of basin impact ejecta, though predicted ejecta thicknesses are too small (Petro and Pieters 2008). If instead the upper mixed feldspathic layer were a result of the floatation of both plagioclase and pyroxene during magma ocean crystallization (Elkins-Tanton and Bercovici 2014), then no direct relationship between the composition and porosity structure would be indicated.

The correlation between gravity and topography is low over the range of spherical harmonic degrees of interest for crustal thickness modeling ≲80; Fig. 3), indicative of varying amounts of isostatic and/or flexural compensation of topography at long wavelengths. Early global models of the lunar crustal thickness assumed uniform crust and mantle densities (Zuber et al. 1994), whereas later formulations considered the possibility of a vertically layered crust (Wieczorek and Phillips 1998), or a crust with lateral variations in density (Wieczorek et al. 2013). A density of 2550 kg/m^3 (Wieczorek et al. 2013) is likely reasonable for the bulk upper crust, although the variation of the effective density with spherical harmonic degree, and the modeled horizontal and vertical variations in density make the choice of a single crustal density for crustal thickness modeling non-trivial. For that crustal density, it is possible to

satisfy local constraints on the crustal thickness from analyses of Apollo seismic data (Khan and Mosegaard 2002; Lognonné et al. 2003; Chenet et al. 2006) in a global crustal thickness model with a mean crustal thickness of 34 km and a mantle density of 3220 kg/m^3, or a mean crustal thickness of 43 km and a mantle density of 3150 kg/m^3. These reduced estimates of the mean crustal thickness relative to previous studies lead to estimated total abundances of aluminum and other refractory elements that are comparable to their concentrations in the Earth, with important implications for lunar formation (Taylor and Wieczorek 2014).

3.1.4. Constraints from geodetic data. The thickness and density of the crust are also constrained by the mass and moment of inertia of the Moon. GRAIL gravity data greatly reduced the uncertainty on the mass of the Moon (so much so that the uncertainty in the gravitational constant G is now the limiting factor; Williams et al. 2014) and provide the degree-2 gravity coefficients J_2 and C_{22}, which, combined with lunar laser ranging, allow calculation of the mean moments of inertia. Inversions of lunar structure typically also incorporate tidal potential and displacement Love numbers k_2 and h_2 and seismic data, but the predicted crustal properties are less sensitive to these data. While some studies have assumed the crustal properties (e.g., Williams et al. 2014) or just the crustal thickness (Garcia et al. 2011) to focus on the deep interior, others have inverted for both crustal thickness and mean density (Matsumoto et al. 2015; Matsuyama et al. 2016), arriving at similar solutions. Matsuyama et al. (2016) found a mean crustal thickness of 41 (+8, −11) km with a mean density of 2736 (+43, −74) kg/m^3. The mean crustal thickness agrees well with the preferred mean value of between 34 and 43 km from GRAIL crustal thickness models tuned to match the local nearside seismic constraints (Wieczorek et al. 2013). The crustal density is somewhat higher than predictions for the upper crust based on GRAIL data (Wieczorek et al. 2013; Besserer et al. 2014) and may be representative of the mean density throughout the crustal column, though this density is not strongly preferred by the moment of inertia inversions.

3.2. Global-scale patterns

3.2.1. Global-scale crustal thickness variations. The largest scale variations in crustal thickness are associated with the global asymmetry, which closely follows a spherical harmonic degree 1 pattern with a nearside–farside difference of 17.5–19.4 km (see EA-6-4 and EA-6-5; Wieczorek et al. 2013). This aspect of lunar structure is best referred to as an asymmetry rather than a dichotomy, as the Moon exhibits a continuous and gradational variation in crustal thickness and topography between the nearside and farside, rather than two distinct provinces of different crustal thickness. The specific amplitude of this crustal asymmetry is sensitive to assumptions of crustal density (and its variation with depth), mantle density, and the possibility of degree-1 variations in the densities of the crust and mantle. For example, the global asymmetry in heat flow associated with the PKT (see discussion below; Grimm 2013; Laneuville et al. 2013; Wieczorek and Phillips 2000) may cause thermal anomalies that persist to the present day, which would lead to higher temperatures and a lower density of the nearside mantle, causing the nearside crustal thickness to be overestimated. At the same time, the higher heat flow experienced by the PKT may have resulted in the thermal annealing of crustal pore space and a greater fraction of intrusions within the crust of the PKT, both of which could lead to a greater crustal density at depth that may bias uniform-density crustal models to underestimate the crustal thickness within the PKT. Nevertheless, this global asymmetry in crustal thickness is also supported by seismic analyses (Chenet et al. 2006) and appears to be a real and dominant aspect of the structure of the lunar crust. This asymmetry was likely established early and has had a profound effect on all subsequent lunar evolution, including the structure of impact basins (Miljković et al. 2013), the history of volcanism (Head and Wilson 1992, 2017), and the Moon's orientation (Siegler et al. 2016).

The global crustal asymmetry has yet to be satisfactorily explained, though a number of models have been proposed. Given the origin of the anorthositic crust through floatation above

a crystallizing magma ocean, an explanation for the crustal asymmetry involving asymmetric magma ocean crystallization is attractive (Wasson and Warren 1980). Alternatively, asymmetric magma ocean convection patterns could have led to greater thickening of the crust in one hemisphere (Loper 2002). Earth-shine (the illumination of the Moon by the hot early-Earth) on the proto-lunar disk may have led to radial zonation in the disk and an asymmetry in the forming Moon (Roy et al. 2014), although rapid convection within the magma ocean may stir and homogenize the Moon on short timescales. Later effects of Earth-shine on the Moon itself were likely minimal (Wasson and Warren 1980).

Stevenson (1980) proposed that the asymmetry could be explained by an ancient Moon with a shallow magma ocean underlain by a deep mantle of cold undifferentiated primordial material of average lunar density. Subsequently, iron is expected to differentiate from the partially molten outer layer and accumulate above the undifferentiated less dense lower mantle, leading to a gravitational instability that would be resolved by the differentiated iron amassing in a lens above the undifferentiated lower mantle in one hemisphere (presumed to be the farside). Consequently, this would shift the center of figure of the undifferentiated lower mantle towards the nearside hemisphere relative to the lunar center of figure, establishing a hemispheric asymmetry in the depth of the magma ocean with greater depths on the lunar farside. This mechanism provides a simple means of generating a hemispheric asymmetry early in lunar evolution. A possible means of producing a long-lasting asymmetry from this state is by the greater accumulation of early-formed lower density cumulates above the iron lens, which would later rise and underplate the farside crust and could displace the late-stage ilmenite-bearing cumulates and urKREEP material to the nearside hemisphere. Alternatively, the crustal asymmetry could be a byproduct of the proposed degree-1 Rayleigh–Taylor instability of the late-formed over-dense ilmenite-bearing cumulates (Parmentier et al. 2002), though a specific mechanism for generating the crustal asymmetry through this process is lacking.

Several different models have invoked giant impacts to explain the hemispheric asymmetry. One model invokes a giant impact to excavate the crust within a nearside mega-basin, with the basin and its ejecta deposit providing a reasonable fit to the global asymmetry (Byrne 2007). Such an impact must have occurred while the crust was still forming, and would be expected to cover the farside in ejecta derived from the crust, the remaining magma ocean, and possibly the underlying cumulate mantle. To first order, this model may be consistent with a deep layer of pure anorthosite (Yamamoto et al. 2012) beneath an upper mixed layer (Hawke 2003) that could represent ejecta of the basin. Impact excavation of the lunar nearside could also explain the observed concentration of KREEP, if KREEP-rich crustal material excavated by the impact slumped back into the basin (Zhu et al. 2019). Hydrocode models of such an impact provide good fits to the global asymmetry in topography and crustal thickness. However, this model requires a very large (Ceres-sized) impactor to strike the Moon after the formation of the crust, which is difficult to reconcile with constraints on the late addition of material to the Moon based on highly siderophile elements (Bottke et al. 2010). This model also predicts that the upper ~10 km of the farside highlands should be composed dominantly of orthopyroxene from the mantle, which conflicts with remote sensing constraints (see discussion above).

Some fraction of the excess topography and crustal thickness of the farside highlands may represent a thick ejecta deposit from the oblique South Pole-Aitken basin impact. The excess volume in the highlands is comparable to the volume excavated from within SPA (Zuber et al. 1994). Impact simulations suggest that at least some fraction of the highlands is expected to be SPA ejecta, though not likely enough to explain the farside crustal thickening (Melosh et al. 2017). Moreover, the farside thickening of the crust is not symmetric about the long axis of the basin, and similar quasi-downrange crustal thickening is not observed in crustal thickness models around the similarly sized and shaped Hellas and Utopia basins on Mars (Neumann et al. 2004), nor around the larger Borealis basin on Mars (Andrews-Hanna et al. 2008).

Alternatively, the thick crust of the farside has been suggested to be a result of accretion of material during a low-velocity impact (Jutzi and Asphaug 2011). In this scenario, a ~1200-km-diameter second moon orbiting the Earth in one of the L4 or L5 Lagrange points could be stable for 10's of Myr before impacting the Moon at the subsonic mutual escape velocity of the two bodies. Models of such a low velocity impact predict accretion of the crust and mantle of the impactor onto the Moon in a layer up to 120 km thick, with crustal material from the projectile remaining at the surface. In order to reconcile this model with the observed plagioclase-rich crust of the lunar farside (Jolliff et al. 2000; Hawke 2003; Ohtake et al. 2009; Yamamoto et al. 2012), the projectile must have also possessed a thick feldspathic crust, which is consistent with the expectation that smaller objects should have proportionally thicker plagioclase floatation crusts formed from their magma oceans (Elkins-Tanton 2012). If this body was composed of material derived from the proto-lunar disk, the crust and mantle resulting from differentiation of its magma ocean might be geochemically and isotopically indistinguishable from the Moon. However, it is difficult to reconcile this model with the observed crustal thickness distribution, which includes a prominent degree-1 asymmetry in addition to near symmetric degree-2 bulges in crustal thickness on the nearside and farside (Garrick-Bethell et al. 2010; see below). The greatest challenge to this model may be the prediction that projectile mantle material should be exposed or buried at shallow depth in a ring at the periphery of the accreted material, which has not been observed. Moreover, if the projectile experienced a similar process of differentiation from a magma ocean, as required to generate an anorthositic crust, it should have also crystallized a layer of KREEP-rich material beneath that crust, for which there is no evidence on the lunar farside.

Superposed on the crustal asymmetry is a prominent spherical harmonic degree-2 pattern of two quasi-symmetric and antipodal crustal thickenings approximately centered on the nearside and farside (EA-6-5; Garrick-Bethell et al. 2010, 2014). This pattern is most clearly expressed on the farside highlands (Garrick-Bethell et al. 2010), which are one of the oldest portions of the crust (Wilhelms 1987), but is also manifest in a region of thicker crust on the nearside west of the Nectaris basin (Garrick-Bethell et al. 2014). The signal's peak-to-trough amplitude as measured on the lunar farside is ~6 km, which is too large to be due to a frozen tidal-rotational bulge (see discussion below). The topography and gravity together indicate that this pattern is a result of a degree-2 variation in crustal thickness. This degree 2 pattern may be explained by analogy to Europa, in which the decoupling of the solid ice shell from the interior by a subsurface ocean is thought to result in increased tidal strains and a degree-2 pattern in both tidal heating and shell thickness (Ojakangas and Stevenson 1989). If the early crust of the Moon was decoupled from the deeper interior by a magma ocean, the Moon may have undergone a similar phase of enhanced tidal heating, leading to a spherical harmonic degree-2 pattern of crustal thickening. The early, more proximal orbit of the Moon about the Earth may have been sufficient to produce the observed degree-2 crustal thickness structure (Garrick-Bethell et al. 2010).

In summary, the Moon exhibits pronounced long-wavelength crustal structure at spherical harmonic degrees 1 and 2, which likely date back to the formation of the crust. Such ancient structures are inherently difficult to explain, since much of the smaller scale structure from those times has been lost. The degree-two pattern is plausibly interpreted as a result of tidal heating effects on crustal production. However, there is no strong evidence in favor of any one mechanism for generating the degree-1 asymmetry. Ultimately, it must be acknowledged that this most fundamental aspect of lunar structure remains unexplained.

3.2.2. Global-scale compensation: The fossil figure. The long-wavelength (spherical harmonic degree-2), triaxial figure of the Moon is expected to be largely controlled by the Moon's response to rotation and tides. However, the observed tidal–rotational deformation of the Moon is more than two orders of magnitude larger than predicted assuming the Moon's present spin/orbit configuration and hydrostatic equilibrium. This excess deformation has been ascribed to a "fossil figure", a remnant shape that froze into place early in lunar history,

likely when the Moon was hotter and much closer to the Earth, and therefore subject to stronger rotational and tidal potentials (Jeffreys 1961). Fossil figures have also been proposed for a number of other bodies in the Solar System (Porco et al. 2005; Castillo-Rogez et al. 2007; Daradich et al. 2008; Matsuyama and Manga 2010; Robuchon et al. 2010). If understood, the lunar fossil figure could be extremely valuable in deducing the Moon's thermal, rotational, and orbital evolution as well as the early geophysical properties of the Earth (which control the rate at which the Moon's orbit evolves outward).

The problem of the lunar fossil figure was first identified more than 200 years ago by Laplace (1798), who used observations of the precession of the Moon's axis made by Cassini (for a review, see Eckhardt 1981) to constrain the Moon's moments of inertia. Laplace parameterized the oblateness via the moment of inertia ratio $(C - A)/C$, which is nearly equal to the modern canonical libration parameter $\beta = (C - A)/B$, where A, B, and C are the minimum, intermediate, and maximum moments of inertia, respectively. Laplace calculated this ratio to be 5.99×10^{-4}, which is remarkably close to the current accepted value of 6.310×10^{-4} (Williams et al. 2014), and found this value to be an order of magnitude larger than the expected hydrostatic value for the Moon's current tidal-rotational state. Sedgwick (1898) proposed that the observed oblateness could be explained if the Moon had cooled while it was closer to the Earth, thereby freezing in a fossil figure. This explanation is compatible with Darwin's hypothesis that the Moon formed closer to the Earth and subsequently migrated outward (Darwin, 1880).

Subsequent work, however, showed that the ratio of the libration parameters α/γ, where $\alpha = (C - B)/A$, $\gamma = (B - A)/C$, do not match the match the ratio of 0.25 predicted for a low-eccentricity synchronously rotating Moon regardless of where the freezing of the fossil figure took place (Jeffreys 1915, 1937, 1948, 1961, 1976; Kopal 1967). A similar ratio may also be expressed as the expected ratio of the degree-2 spherical harmonic gravity or topography coefficients, $C_{2,0}/C_{2,2} = -10/3$, or -0.96 in normalized coefficients, compared with the observed normalized coefficient ratio from GRAIL of -2.6210 (Konopliv et al. 2014). This discrepancy could be resolved if the lunar fossil figure originated during a 3:2 resonance of spin period to orbit period, or during a high-eccentricity synchronous orbit (Garrick-Bethell et al. 2006). However, subsequent work showed that this scenario is unlikely from orbital dynamics and thermal perspectives (Meyer et al. 2010).

The above studies assumed a rigid Moon since the time the fossil bulge was acquired, but the actual magnitude of the fossil bulge depends on the thickness of the lithosphere maintaining that fossil figure (Lambeck and Pullan 1980; Zhong and Zuber 2000). An elastic lithosphere thickness of 50 km reduces the inferred Earth–Moon distance at the time of freeze-in by ~25% compared to the case of infinite rigidity (Matsuyama 2013). Taking into consideration the time-dependent thickening of the lithosphere during lunar orbital evolution, a fossil figure that formed 100–200 Myr after magma ocean crystallization would retain 25–50% of the maximal hydrostatic value when freeze-in started (Qin et al. 2018).

Several studies have considered whether geologic processes since freeze-in could explain any discrepancy in α/γ from its expected value, such as long-wavelength patterns in mantle convection (Kopal 1965; Runcorn 1967). The lunar gravity power spectrum shows excess power at degree-2, suggesting that the fossil figure dominates over random geologic effects (Lambeck and Pullan 1980). The gravity, topography, and crustal thickness at spherical harmonic degree-2, after correcting for the later effects of impact basins, may be understood as the sum of two early processes: the freeze-in of a fossil figure maintained by the lithosphere, and an earlier tidal heating process which produced a degree-2 pattern in the Moon's crustal thickness as discussed above (Fig. 4; Garrick-Bethell et al. 2010, 2014). An alternative correction for the contribution of lunar basins resulted in a fossil figure consistent with freeze-in when the Moon was in a synchronous, low-eccentricity ($e \sim 0.2$) orbit at a radius of 15–17 Earth radii, and was inconsistent with higher-order spin/orbit resonances (Fig. 4; Keane and Matsuyama 2014).

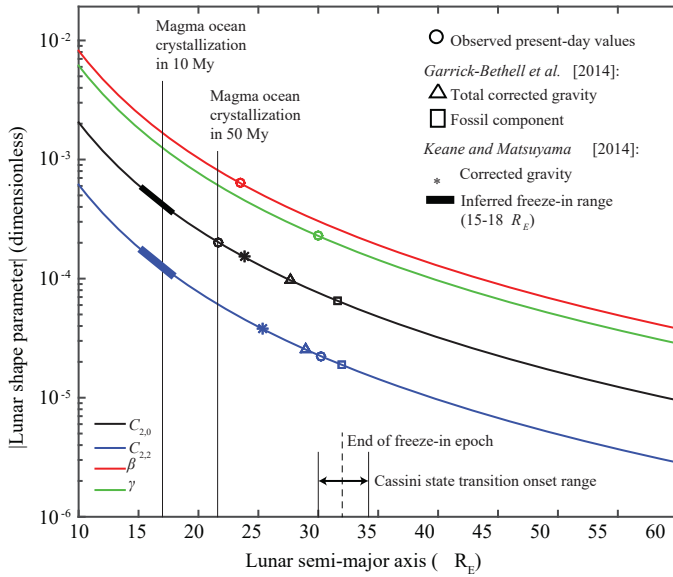

Figure 4. Spherical harmonic degree-2 gravity coefficients (unnormalized) and libration parameters at various semi-major axes in lunar history, assuming a synchronously locked homogenous Moon at zero eccentricity with zero strength (k_2 = 1.5). The observed values are plotted on their implied freeze-in semi-major axis. A self-consistent fossil-bulge solution would place all parameters at the same semi-major axis. Values correcting for large lunar basins from GB14 are shown along with value due to the fossil bulge alone. Values correcting for large lunar basins from KM14 are shown along with their inferred semi-major axis of freeze-in assuming elastic thicknesses of 25–50 km. A range of plausible onsets of the Cassini state transition is shown (Ward 1975; Siegler et al. 2011), after which the Moon may be reshaped. The inferred end of the freeze-in epoch from Qin et al. (2018) is shown as a dashed line. Libration parameters γ and β are dependent on each other, hence they fall at the same semi-major axis

The lunar figure may also retain a record of the Moon's past orientation. The orientation of the Moon and the location of the rotation axis and tidal pole (i.e., sub/anti-Earth points) are controlled by the lunar figure, and more precisely, the orientation of the Moon's principal axes of inertia. A change in the orientation of the principal axes, as could arise from a variety of large-scale geological and geophysical processes, results in the reorientation of the body in inertial space—a process known as true polar wander. For example, the formation of the South Pole-Aitken basin may have resulted in ~15° of true polar wander, while smaller impact basins resulted in less than ~1° of true polar wander each (Keane and Matsuyama 2014). The formation and evolution of the Procellarum KREEP terrane may also have resulted in ≳ 5° of true polar wander, as supported by interpretations of the distribution of hydrogen near the lunar poles (Siegler et al. 2016). If the degree-2 crustal thickness pattern is used to identify the earliest tidally locked reference frame of the Moon, it leads to the inference of 35° of true polar wander since crust formation (Garrick-Bethell et al. 2014).

Evidence for true polar wander is also recorded in magnetic paleopole locations (Runcorn 1983), though magnetic paleopoles alone cannot distinguish between true and apparent polar wander without additional constraints (e.g., Besse and Courtillot 2002). Magnetic paleopoles have been determined in several recent studies (e.g., Hood 2011; Takahashi et al. 2014), and are discussed in more detail in Wieczorek et al. (2023, this volume).

In summary, the fossil figure of the Moon as recorded in its moments of inertia and the associated degree-2 gravity coefficients provide strong support for the freeze-in of a rotationally and tidally deformed state when the Moon was much closer to the Earth in its

early evolution. The observed moments of inertia do not match expectations for the simple freeze-in of the shape of a synchronously rotating body in a low eccentricity orbit. However, the discrepancies may be explained by a combination of the effects of a degree-2 pattern in crustal thickness associated with early tidal heating, the effects of the numerous large impact basins, and true polar wander since the fossil figure was emplaced.

3.3. Regional-scale structure of the crust: South Pole-Aitken, Procellarum, and the maria

3.3.1. Crustal terranes: South Pole-Aitken and Procellarum. Beyond the spherical harmonic degree 1 and 2 patterns, the next largest structures in the lunar crust are the South Pole-Aitken impact basin and the Procellarum region (see EA-6-5). The basin is markedly elliptical in shape (Garrick-Bethell and Zuber 2009), as expected for giant impact basins (Andrews-Hanna and Zuber 2010), and encloses a compositionally distinct crustal terrane (Jolliff et al. 2000). Although the crust on the basin floor is thin (10–15 km in the basin center), it only approaches 0 km in thickness within smaller superposed basins (e.g., Apollo and Poincare basins; Potter et al. 2018), and the crust over most of the basin floor is markedly thicker than that found within a number of smaller basins outside of SPA (e.g., Crisium and Moscoviense basins; Wieczorek et al. 2013). The floor of SPA is characterized by a higher grain density (Huang and Wieczorek 2012) than the highlands, consistent with the mafic mineralogy both at the surface (Jolliff et al. 2000) and at depth (Cahill et al. 2009). SPA similarly has a higher bulk crustal density and steeper density gradient than the highlands (Wieczorek et al. 2013; Besserer et al. 2014; Goossens et al. 2020), with a best-fit surface density of 2411 ± 117 kg/m^3 and density gradient of 49 ± 23 kg/m^3/km (Goossens et al. 2020). The crust beneath the SPA basin floor likely originated from a combination of differentiation of the impact melt pond (Hurwitz and Kring 2014; Vaughan and Head 2014; Uemoto et al. 2017) and flow of crust into the basin during the collapse of the transient cavity (Stewart 2012; Potter et al. 2018). The gravity signature of the basin also suggests the presence of a deep mass anomaly beneath the basin, possibly associated with iron from the projectile or a mantle density anomaly (James et al. 2019).

Even larger than SPA, a giant Procellarum impact basin has been proposed to be responsible for the low topography, thin crust, and unique composition of the Procellarum KREEP terrane (Cadogan 1974; Whitaker 1981). The similar pyroxene-rich mineralogy of the crust in Procellarum and South Pole-Aitken has also been interpreted as evidence for a Procellarum impact basin (Nakamura et al. 2012). However, analyses of the structure of the region as revealed by gravity data found that the structures interpreted as arcuate basin rim and ring segments are instead part of a large quasi-rectangular set of magmatic-tectonic structures (Andrews-Hanna et al. 2014; see discussion below). The structure of the crust in this region does not show any clear evidence for an impact basin, and can largely be explained by the superposition of the degree 1 and degree 2 crustal thickness variations with the higher degree signature of the magmatic-tectonic border structures (Andrews-Hanna 2016). However, the above arguments alone do not necessarily rule out the possible existence of such a basin.

Regardless of its origin, the subsurface structure of the PKT remains in question. The crust within the PKT is clearly thinner than the global average (Wieczorek et al. 2013). However, the elevated temperatures in the crust and mantle as a result of the high concentrations of heat producing elements should cause thermal uplift affecting the gravity and topography (Grimm 2013; Laneuville et al. 2013), which complicates interpretations of the crustal structure. The true size and extent of the PKT also remains in question. The surface is clearly enriched in KREEP-rich material (Lawrence et al. 1998; Jolliff et al. 2000; Chen et al. 2015), but the vertical and lateral distribution of KREEP in the subsurface is unknown. Ejecta from the Imbrium basin dominates much of the observed surface distribution of thorium (Haskin 1998). An absence of similar Th enrichments around other basins (including SPA, Serenitatis, Crisium, and Nectaris) indicates that the target crust within their excavation cavities was not similarly

enriched in KREEP (Jolliff et al. 2000). However, this interpretation depends upon the poorly constrained vertical distribution of KREEP relative to the excavation depths of the impacts, and the resulting mixing ratio of KREEP in the ejecta. The exceedingly weak magnetic fields in a nearside magnetic low within the PKT may reflect the subsurface distribution of KREEP-rich material, concentrated within an area ~1/3 of the size of the PKT itself (Wieczorek 2018).

3.3.2. Maria. The basaltic maria covering much of the nearside and isolated patches of the farside are a substantial component of the upper crust. Earlier studies used geological evidence in the form of volcanically embayed craters (De Hon and Waskom 1976; De Hon 1978), finding thicknesses generally < 1.5 km outside of the major impact basins. However, geophysical analyses indicated the possibility of much thicker maria within the basins (Solomon and Head 1980). Gravitational evidence for buried craters provide an added constraint on the mare thickness, leading to a mare volume range of 1.1–3 × 10^7 km^3, or mean thicknesses of 1.5–4 km over the areas analyzed (Evans et al. 2016). Gong et al. (2016) used localized gravity spectra under the assumption that the buried crust beneath the maria resembles typical lunar highlands and that a correlation exists between the sub-mare relief and the surface topography, and found an average thickness of 0.7 (–0.6, +0.9) km for the western maria. The thickness of the maria were also mapped using gravity and topography in a two-layer crustal thickness model (Fig. 5; Andrews-Hanna et al. 2014) yielding a volume of 8.8 × 10^6 km^3 and a mean thickness of 1.6 km, which are lower bounds since flexure was neglected in that model. Of that volume, 34% resides within the centers of the Imbrium, Serenitatis, Crisium, Humorum, and Nectaris basins, which collectively comprise 14% of the surface area of the maria but have a predicted mean thickness of 4 km. The above studies each used very different approaches and arrived at different and sometimes contradictory maps of mare thickness. Nevertheless, there is general agreement in the result that the average nearside mare thickness is on the order of 1 km, being much thicker within the large basins and thinner elsewhere. These geophysical estimates compare well with the earlier geological estimate of 1 × 10^7 km^3 (Head and Wilson 1992). The smaller-scale structure within the maria and a variety of other smaller intrusive bodies are discussed in more detail in the sections below.

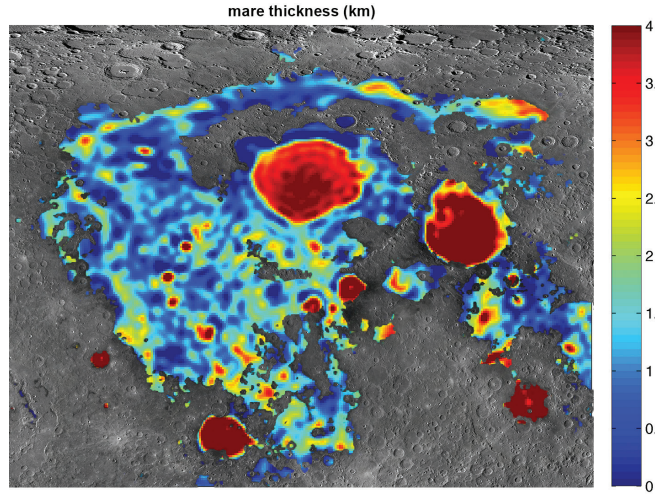

Figure 5. One model of the mare thickness over the nearside Procellarum region. This model assumes the feldspathic crust was isostatic prior to mare infilling, but neglects the effect of flexure and thus underestimates mare thickness (Andrews-Hanna et al. 2014). Background image is a LRO Wide Angle Camera image mosaic.

Some maria may not exhibit the characteristic albedo difference relative to the highlands as a result of an overlying layer of feldspathic impact ejecta. Two different approaches for using gravity data to constrain this cryptomare volume yielded ranges of 4.2–6.6 × 10^5 km^3, and 1.8–2.8 × 10^6 km^3 (Sori et al. 2016). The first lower estimate based on gravity anomalies relative to the expected isostatic gravity field is the preferred value, while the latter higher estimate based on filtered Bouguer gravity may treat some regions of thinner crust as being associated with cryptomare.

3.4. Mesoscale structure of the crust: Impact basins and ancient tectonics

3.4.1. Crustal structure of impact basins. At scales of hundreds of kilometers, crustal thickness variations on the Moon are dominated by the signatures of impact basins (Zuber et al. 1994; Neumann et al. 1996; Wieczorek and Phillips 1999; Wieczorek et al. 2013). The details of lunar basin formation and modification are explored in more detail elsewhere (Osinski et al. 2023, this volume), and we here focus on the manifestation of impact basins within the structure of the crust and upper mantle. The largest impact basins have a substantial effect on the crustal structure (EA-6-5), and are generally characterized by a central positive Bouguer anomaly (EA-6-6; Neumann et al. 2015), arising from the thinning of the crust and uplift of mantle within the excavated crustal cavity (Wieczorek and Phillips 1999; Wieczorek et al. 2013) as observed at Nectaris (Fig. 6). These positive Bouguer anomalies are observed at basin diameters greater than ~200 km (Neumann et al. 2015), and are generally confined to within the innermost major ring, which is roughly half the diameter of the outermost major ring in most cases (Wieczorek and Phillips 1999; Neumann et al. 2015; Baker et al. 2017). These innermost major ring structures are interpreted as peak-rings formed when the outward-collapsing central uplifts overran the inward-collapsing rims of the excavation cavities (Collins 2002; Baker et al. 2016). Although mantle uplift likely dominates the Bouguer anomalies of the larger multi-ring basins, for the smaller peak-ring basins such as Mendeleev (Fig. 6) we cannot rule out the possibility that the source of the Bouguer gravity signal could include a substantial contribution from the uplift of dense deep crustal material, as is the case for the Chicxulub basin on Earth (Vermeesch and Morgan 2008; Christeson et al. 2009; Gulick et al. 2013). Models of basin structure with a lower crust of greater density may be more accurate (Wieczorek and Phillips 1999; Andrews-Hanna et al. 2018), but are under-constrained. The central zone of thinned crust and uplifted mantle is surrounded by an annulus of negative Bouguer gravity

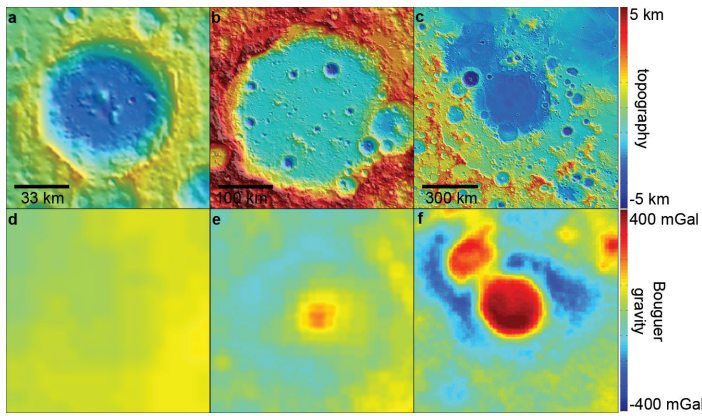

Figure 6. Topography (**top**) and Bouguer gravity (**bottom**, with a high pass filter at degree 10 and low-pass filter at degree 300) for the **a** Lobachevskiy crater, **b** Mendeleev, and **c** Nectaris, showing the progression in geophysical expression from complex crater, to peak ring basin, to multi-ring basin. Each panel is 3× greater in horizontal scale than the panel to the left. Nectaris is superimposed over the pre-existing Asperitatis basin to the northwest.

indicating the presence of thickened crust within the ejecta blanket (Wieczorek and Phillips 1999). The diameter of this annulus provides a useful criterion for defining the size of the basin for comparison with numerical models (Potter et al. 2012).

The Orientale basin is often taken as the archetype of a multiring basin, given its status as the youngest and best-preserved large impact basin. The similarly aged Imbrium basin is largely buried beneath the nearside maria, while the structures of older basins have been substantially modified by viscous relaxation, mare volcanism, and excavation by subsequent impacts. Orientale has only a thin (< 0.2 km) central mare, and minor mare deposits ponded within its rings (Head 1974; Whitten et al. 2011). Orientale is characterized by a minor inner ring and three major rings: the Inner Rook, Outer Rook, and Cordillera. The modeled crustal thickness is less than 10 km within the inner ring, increasing abruptly at the Inner Rook ring to a maximum of ~60 km (Wieczorek et al. 2013). The decrease in crustal thickness away from the basin outside of the Inner Rook is consistent with the decrease in the thickness of the ejecta blankets observed around smaller craters (Wieczorek and Phillips 1999).

The topographic expression of ring scarps around Orientale and other lunar basins have long been interpreted as representing ring-like faults extending into the subsurface (Hartmann and Kuiper 1962; Head 1977). The patterns of uplift around the ring scarps are well matched by elastic dislocation models of faults penetrating to at least mid-crustal levels (Nahm et al. 2013). Both azimuthally-averaged pre-GRAIL analyses (Andrews-Hanna 2013; Kattoum and Andrews-Hanna 2013) and high-resolution crustal thickness models from GRAIL (Zuber et al. 2016; Andrews-Hanna et al. 2018) show clear evidence for ring faults at the Outer Rook and Cordillera crossing the crust–mantle interface (Fig. 7). Displacements across the ring faults in the subsurface (Andrews-Hanna et al. 2018) are comparable to the relief across the scarps at the surface (Nahm et al. 2013) and in agreement with models of basin ring formation (Johnson et al. 2016). As discussed further below, the gravity gradients at the Outer Rook and portions of the Cordillera ring indicate the presence of ring dikes intruded into the ring faults (Andrews-Hanna et al. 2018).

The ejecta blanket surrounding Orientale has a notably lower density and higher porosity than its surroundings (Wieczorek et al. 2013), unlike older basins that have experienced more degradation due to impact-induced seismic shaking (Kreslavsky and Head 2012) and to the direct effects of smaller superposed impacts (Milbury et al. 2015). The ejecta blanket of Orientale also exhibits pronounced radial gravity anomalies associated with radial density anomalies within the ejecta blanket (Jansen et al. 2019), in some cases associated with catenae and chains of secondary craters (Guo et al. 2018). These anomalies are interpreted as resulting from the secondary projectile material (Orientale basin ejecta) that remains within the secondary craters and catenae as a result of the low velocity of the secondary impacts, as well as radially extended variations in density of the ejecta deposit as a whole (Jansen et al. 2019). Globally, ejecta from lunar basins contributes substantially to the thickness (Petro and Pieters 2008) and density variability (Jansen et al. 2019) of the lunar megaregolith, and may contribute to magnetic anomalies in the upper crust as well (Wieczorek et al. 2012; Gong and Wieczorek 2020).

The crustal structure of a given basin is affected by the impactor properties, target properties, impact geometry and speed, and subsequent modification, and thus provides a window into lunar evolution. Impacts into warmer crust produce larger basins (Potter et al. 2012), and thus the nearside–farside asymmetry in basin sizes may be explained by hemispheric variations in heat flow (Miljković et al. 2013). The temperature and thickness of the crust also affect the structure of the surrounding ring system (Potter et al. 2013; Johnson et al. 2016).

Subsequent to their formation, ancient mid-sized lunar basins may have undergone varying degrees of viscous relaxation (Mohit and Phillips 2006). The present-day structure of basins coupled with models of basin relaxation can be used to constrain lateral variations in the heat flux and abundance of crustal radioactivity, supporting a cool highlands crust without an underlying

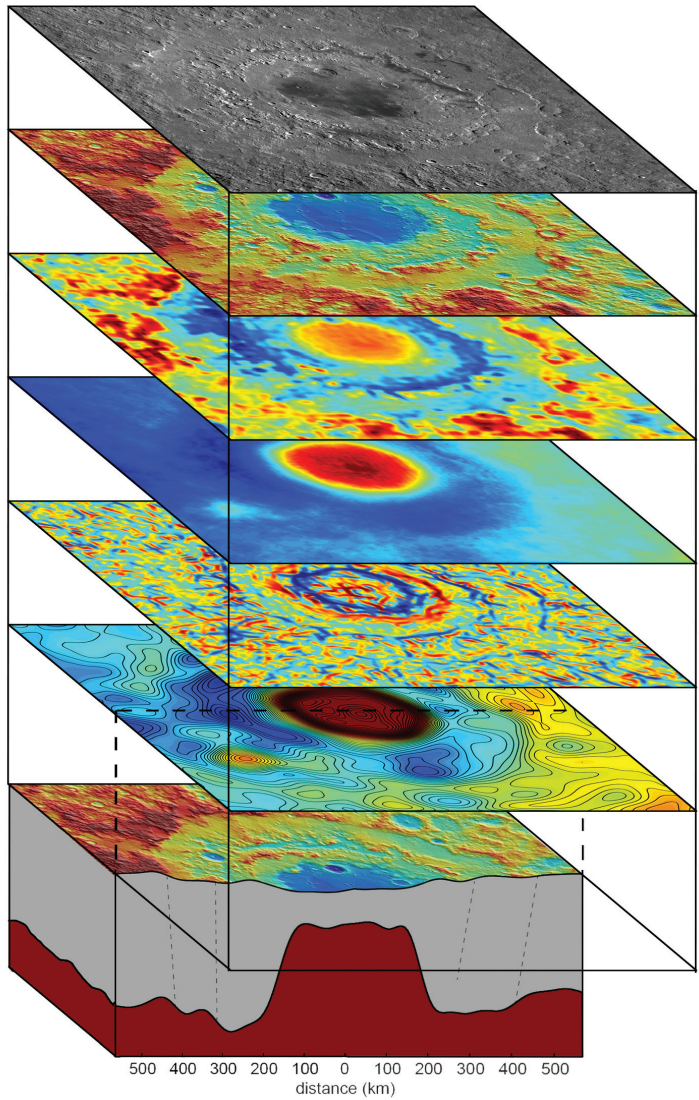

Figure 7. Orientale basin as seen in (from top to bottom) WAC image mosaic, LOLA topography, GRAIL free air gravity, GRAIL Bouguer gravity, GRAIL gravity gradient, and a contour plot of the relief along the crust–mantle interface. The **cutaway** at the bottom includes average profiles through the crust from the NW and SE quadrants of the basin, with ring faults shown as **dashed lines**.

layer enriched in heat producing elements as is inferred beneath the Procellarum KREEP terrane on the nearside (Kamata et al. 2013). Numerical modeling of the viscoelastic deformation of impact basin structure indicates that substantial relaxation of the central mantle uplift occurs only when the temperature at the base of the crust exceeds 1500 K, which may only be achievable within ~50 Myr after the solidification of the lunar magma ocean (Kamata et al. 2015).

Even some basins with the most degraded surface expressions show clear subsurface structure in the gravity data (Neumann et al. 2015). The structure of these ancient basins is preserved in part because of the difficulty of removing the central crustal thinning by viscous

relaxation (Mohit and Phillips 2006; Kamata et al. 2013), and in part because dikes intruded into the ring faults create a density anomaly that persists long after the surface expression of the rings has been destroyed by subsequent impacts (Andrews-Hanna et al. 2018). For example, the ancient Fowler–Charlier basin, which has very little topographic expression and no evidence for rings at the surface, is nevertheless characterized by a clear positive Bouguer anomaly (Neumann et al. 2015) as well as an outer ring structure in gravity gradient maps (Andrews-Hanna et al. 2018). Similarly, despite being strongly overprinted by the younger Schrodinger basin, the ancient Amundsen–Ganswindt basin has an unambiguous gravitational signature of a peak-ring basin (Neumann et al. 2015; Baker et al. 2017). Thus, it can be concluded that impact basins leave indelible marks in the geophysical record of the crustal structure, with the exception of those basins formed immediately following the magma ocean solidification, and the inventory of post-magma ocean lunar basins is now largely complete.

Using the presence of a circular positive Bouguer anomaly as a diagnostic criterion, GRAIL data reveal three previously unknown impact basins, confirm an additional 13 proposed basins, and find no support for 71 basins proposed based on interpretations of subtle expressions in geological or pre-GRAIL geophysical data (Neumann et al. 2015). GRAIL and LOLA data together have led ~18 complex craters to be re-classified as peak-ring basins based on their crustal structure (Neumann et al. 2015; Baker et al. 2017). Existing catalogs of lunar basins (Neumann et al. 2015) place a strong constraint on the bombardment history of the Moon since the stabilization of the crust at the end of the lunar magma ocean.

3.4.2. Mascons. The positive Bouguer anomalies associated with impact basins (Fig. 6e,f) require some amount of deep compensation of the basin topography, but can occur for basins in any state of compensation, whether isostatic, sub-isostatic, or super-isostatic. In contrast, a basin with an anomalous central mass concentration ("mascon"), as originally defined, is one with a positive free air gravity anomaly within its center (EA-6-7; Muller and Sjogren 1968), indicating that the crust beneath the basin floor is above the level predicted for a state of isostasy (i.e., is super-isostatic). A definition of mascons based on the isostatic state may be most useful, since perfect isostasy for an impact basin entails a modest negative gravity anomaly, whereas a basin with a surface depression and zero gravity anomaly is slightly super-isostatic and thus does possess an excess mass concentration (Reindler 2001; Andrews-Hanna 2013). Many of the nearside mascons are dominated by the effects of flexurally supported mare fill within the basin centers (Solomon and Head 1979, 1980; Williams and Zuber 1998). However, early farside gravity data revealed the presence of mascons in some basins with little or no mare infill (Zuber et al. 1994; Neumann et al. 1996), which is likely representative of the compensation state of the basins shortly after the impacts that formed them. Most mascon basins are surrounded by prominent negative gravity anomalies (Sjogren and Smith 1976; Zuber et al. 1994), revealing the presence of a sub-isostatic annulus (Andrews-Hanna 2013). The Orientale mascon (Fig. 7) can be explained if the basin was initially characterized by an isostatic center surrounded by an annulus within which the crust was both thickened by the ejecta and left in a sub-isostatic state by the impact, and the subsequent isostatic uplift of the annulus and its flexural coupling with the basin center resulted in uplift of the basin floor to produce the observed mascon (Andrews-Hanna 2013; Melosh et al. 2013). Hydrocode modeling has shown that the annulus surrounding the excavated cavity is indeed left in a sub-isostatic state following the impact, and the subsequent viscoelastic evolution of the basins can reproduce the observed structure and gravity anomalies (Melosh et al. 2013; Freed et al. 2014).

3.4.3. Ancient tectonics in the Procellarum region. In addition to the lunar basins, a set of crustal thickness anomalies of comparable scale are found bordering the nearside Procellarum KREEP terrane (Andrews-Hanna et al. 2014). Individually, these structures are expressed as linear to arcuate positive gravity anomalies with widths of ~100 km and lengths of 100s to >1000 km. Collectively, these structures form a quasi-rectangular pattern ~2600 km across

that encompasses the Procellarum KREEP terrane. As such, the Procellarum border structures are one of the dominant features in gravity and gravity gradient maps, and collectively are the largest single crustal structure on the Moon (exceeding even the South Pole-Aitken basin in size). Inversions of the gravity data predict subsurface structures consisting of narrow zones of thinned crust and uplifted mantle overlain by maria that are thicker than the surroundings (see Fig. 5). These structures are consistent with the presence of volcanically flooded rift valleys, though closely-spaced swarms of dikes can also fit the data. The arcuate shapes, branching patterns, and the intersections of structures at 120° angles are all consistent with the behavior of continental rift zones on Earth, Mars, and Venus (Hauber et al. 2010). If these structures are buried rift zones, they are the only such structures on the Moon indicative of large-strain lithosphere-scale extensional tectonism, and the only tectonic features not related to impacts that have substantially modified the structure of the lunar crust.

3.5. Small-scale structure of the crust: Impacts, intrusions, and more

A variety of features observed in the gravity field are interpreted as structures embedded within the crust, though not affecting the thickness of the crust at scales resolved by existing models. These features reflect the multitude of processes that have modified the physical properties of the crust since its formation. Although both structures within the crust and variations in relief along the crust–mantle interface can exist across all scales, the instability of global crustal thickness models for spherical harmonic degrees greater than ~80 (Wieczorek et al. 2013) indicates that the gravity field at scales smaller than ~70 km is dominated by the effects of density anomalies embedded within the crust rather than relief along the crust–mantle interface.

3.5.1. Craters. At scales smaller than basins, simple and complex craters have minimal effect on the deep structure of the crust, since they excavate only a small fraction of the crustal column and do not impart deflections to the crust–mantle interface or positive Bouguer anomalies (Fig. 6; Neumann et al. 2015; Baker et al. 2017). Nevertheless, craters of all sizes show a systematic gravitational signature as a result of their effect on the density of the underlying crust (Soderblom et al. 2015). A trend of increasingly negative Bouguer anomalies with increasing crater size between diameters of 20 and 200 km, reaching a value of −15 mGal at a diameter of 93 km before leveling off, reveals the generation of impact-induced porosity below the crater floors. The fact that individual craters show any anomaly at all demonstrates that the crust over the range of depths sampled (up to and exceeding ~8 km) has not reached a steady-state level of impact damage (Soderblom et al. 2015). Hydrocode models show that impacts into porous targets can either create or destroy porosity, depending on the target porosity (Milbury et al. 2015). Systematic differences in crater gravity anomalies in regions of different porosity (Soderblom et al. 2015), and between the lunar highlands, maria, and the South Pole-Aitken basin (Bierson et al. 2016) support previous inferences of differences in bulk density, grain density, and porosity between these regions (Wieczorek et al. 2013; Besserer et al. 2014). However, the gravitational signatures of craters are only evident when analyzing large numbers of craters in aggregate, with the scatter about the trend of Bouguer anomaly as a function of crater diameter (±25 mGal) being comparable in magnitude to the trend itself (Soderblom et al. 2015). Thus, while craters of all sizes dominate the free air gravity (Zuber et al. 2013), they comprise a comparatively small fraction of the Bouguer anomaly.

Although the lunar maria have much lower densities of impact craters at the surface (Hiesinger et al. 2003, 2010), buried craters within these regions comprise an important component of the structure of the crust. Despite deficits in the numbers of smaller craters, a population of numerous buried craters is observed in the gravity data as quasi-circular mass anomalies or QCMAs (Evans et al. 2016; Sood et al. 2017), confirming the presence of an ancient cratered surface underlying the volcanic plains. The combined abundance of craters and QCMAs also provide important constraints on the relative and absolute ages of a number of lunar terranes and basins (Evans et al. 2018a).

3.5.2. Volcanic and magmatic structures. One of the most prominent short-wavelength signatures in the lunar gravity field is in the form of a large number of exceedingly long linear gravity anomalies that are most clearly observed in gravity gradient maps (Fig. 8; Andrews-Hanna et al. 2013). These randomly oriented linear gravity anomalies are both narrower and less organized than the PKT border anomalies discussed above. The long, linear, positive gravity anomalies are most simply explained by the presence of dike-like intrusive bodies. Inversions of the gravity data yielded typical widths of 7–80 km, suggesting that the individual structures may be more similar to dense swarms of parallel dikes or to single larger scale intrusions than to typical dikes. One of the largest of these, on the northern farside, has a modeled volume of 1.5–2.9 × 10^5 km^3, assuming density contrasts of 800–550 kg/m^3.

A number of prominent, narrow, ring-shaped gravity and gravity gradient anomalies are observed in association with the rings of many impact basins, interpreted as ring dikes intruded into the basin ring faults (Andrews-Hanna et al. 2018). At Orientale, the Outer Rook ring dike continuously encircles the basin, despite the limited and discontinuous evidence for eruptive activity in the form of mare ponds to the east and a pyroclastic deposit to the west. Notably, the volume of this dike of 2.4 × 10^5 km^3 is 84 times greater than the volume of all surface mare ponded within the rings, and 18 times the volume of all maria associated with the basin (Head 1974; Whitten et al. 2011). Other similar circular gravity structures are found in association with the rings of a number of other basins (e.g., Nectaris; Fig. 8), suggesting that this intrusive activity played a substantial role in the magmatic evolution of the Moon, and features prominently in the structure of the crust.

Evidence for intrusive activity is also found in the form of floor-fractured craters (Fig. 8; Schultz 1976), interpreted as forming due to intrusions of magma beneath the floors of impact craters (Jozwiak et al. 2015) in response to the unloading of the lithosphere by the crater (Michaut and Pinel 2018). A global survey revealed 206 floor-fractured craters with diameters between ~10 and 210 km (Schultz 1976), commonly characterized by shallow depths and uplifted crater floors due to the intrusion of magma below the crater floor (Jozwiak et al. 2015). Analysis of topography and gravity data support a typical intrusion thickness of 0.5 km with a density contrast of ~900 kg/m^3, consistent with intrusion of dense basalt into the porous crust (Thorey et al. 2015), leading to a volume of 1.7 × 10^4 km^3 for the largest floor-fractured crater intrusion.

Gravity data also reveal intrusions associated with volcanic constructs. The Marius Hills volcanic complex is a large field of volcanic domes within Oceanus Procellarum. Gravity data reveal two large free air anomalies in the area, one of which underlies the main dome complex (Kiefer 2013). Analyses of the gravity data support the interpretation of the two anomalies as disk-shaped intrusions with diameters of 160–180 km and 100–140 km, with minimum thicknesses of 3.0 and 6.2 km, respectively. These results yield an intrusive volume of 1.6 × 10^4 km^3, which exceeds the volume of extrusive material in the Marius Hills of 1.0 × 10^4 km^3. Alternatively, the data can be fit by a subsurface dike complex making up ~50% of the crustal volume (Deutsch et al. 2019), and the gravity data cannot distinguish between the these two possibilities. Rumker Mons may also be associated with an intrusive body (Chisenga et al. 2020).

The relationship between gravity and topography data also provides a constraint on the density of volcanic constructs. Densities derived for Gruithuisen Delta and Gruithuisen Gamma (2150 kg/m^3) are much lower than expected for basaltic lavas, and suggest that these edifices are either extremely porous or, more likely, composed of lower density felsic materials with substantial porosity (Kiefer et al. 2016). These low densities are consistent with remote sensing evidence for more highly silicic compositions of these constructs based on the position of the Christiansen feature (Glotch et al. 2010).

In summary, gravity data now provide clear evidence for large-scale intrusions within the crust, and enable us to quantify the dimensions of these bodies and their contribution to the lunar crust. This geophysical evidence provides a record of intrusive activity throughout lunar history.

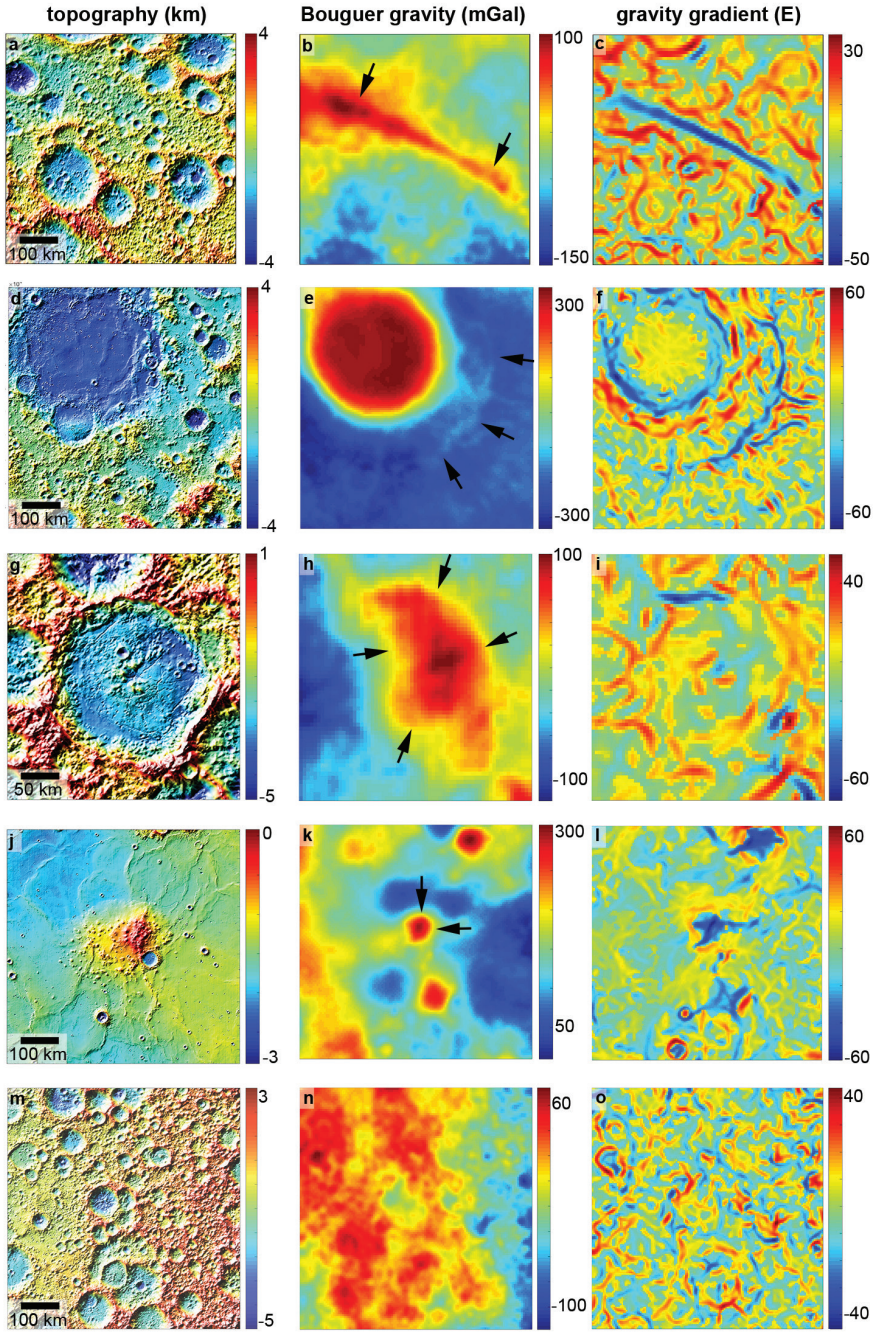

Figure 8. Topography (**left**, km), Bouguer gravity (**center**, mGal), and gravity gradients (**right**, Eötvös) over a sampling of small-scale structures embedded within the lunar crust. Panels show a linear intrusion (**a–c**; centered on 65° N 180° E), the Nectaris ring dike in the southeast quadrant of the basin (**d–f**; centered on 20° S, 38° E), the floor-fractured crater Humboldt (**g–i**; centered on 27° S 81° E), the Marius Hills and associated intrusion (**j–l**; centered on 13° N 307° E) and a non-descript region of farside highlands showing lacking any known large structures but displaying random variability in the gravity (**m–o**; centered on 20° N 120° E).

The evolving style of intrusive activity may reflect the evolving stress field in the lithosphere. The ancient randomly oriented linear intrusions indicate an isotropic extensional stress regime in the lithosphere during the pre-Nectarian. Since the Nectarian, large dike-like structures visible in the gravity field are limited to basin rings, where they could take advantage of flexural stresses around mascon basins and preferred zones of ascent along the ring faults. Less common are large-scale intrusions associated with volcanic constructs, such as that beneath the Marius Hills. Elsewhere, sills associated with floor fractured craters are consistent with a horizontally compressional stress field. The increasing compressive stress also could have inhibited later extrusive volcanic eruptions (Head and Wilson 1992; Wilson and Head 2017). The late peak in dominantly nearside extrusive volcanism may have been controlled by the unique thermal and geodynamic evolution of the Procellarum region (Laneuville et al. 2013).

3.5.3. Structure within the maria. The small-scale structure within the lunar maria is primarily in the form of the layering of the individual flows making up the units. This layering is observed directly in the walls of collapse pits and skylights, with observed layer thicknesses of 3–14 m (Robinson et al. 2012). Radar sounders provide a complimentary dataset on the layering within the mare, as they are unable to resolve individual meter-scale flows, but their depth penetration allows identification of layering accompanied by contrasts in dielectric constant at depths of up to several kilometers. A re-analysis of the Apollo 17 Surface Electrical Properties Experiment found a thin low-density regolith with a rapid density gradient in the top 30 m, transitioning to intact but fractured basalt at a depth of ~300 m (Grimm 2018). The Apollo Lunar Sounder Experiment on board the Apollo 17 Command and Service Module first revealed layering within the maria (Phillips et al. 1973), with layer interfaces at depths of 0.9 and 1.6 km beneath Mare Serenitatis and 1.4 km beneath Mare Crisium (Peeples et al. 1978). More recent analyses from the Lunar Radar Sounder aboard the Kaguya spacecraft identified layering within the top several hundred meters within Mare Imbrium, Mare Crisium, and Oceanus Procellarum (Ono et al. 2009). In Serenitatis, correlation of the layering to surface units led to the inference that this layering represents a hiatus in the volcanism of 110–170 Myr, during which a regolith layer may have developed on the paleo-surface (Ono et al. 2009). Collectively, these observations indicate mare stratigraphy consisting of layering on the scale of individual flows with thicknesses of meters to tens of meters, along with major interfaces at depths ranging from hundreds of meters to kilometers.

In addition to this layering, lava tubes have long been inferred to exist within the lunar maria based on the interpretation that some sinuous rilles formed as collapsed lava tubes (Hurwitz et al. 2013) and the recent identification of skylights (Haruyama et al. 2009; Robinson et al. 2012). In addition to three skylights within the maria, ~150 steep-walled pits have been identified in impact melt deposits with diameters up to 100 m, indicating substantial large-scale void space within those deposits as well (Robinson et al. 2012). Supporting geophysical evidence for intact lava tubes now exists from both gravity and radar data. While numerous sinuous gravity gradient anomalies are observed across all terrains, the majority of these are likely just expressions of the random small-scale variability in the gravity (see next section). However, the alignment of one such sinuous gravity anomaly with the end of Schröter's Rille is consistent with the presence of a large intact lava tube (Chappaz et al. 2017). This inference is consistent with mechanical models indicating that large lunar lava tubes can remain open beneath a thin rock roof (Blair et al. 2017). Possible evidence for open lava tubes has also been identified in radar sounding data (Kaku et al. 2017). While open lava tubes and cavernous void space may be a volumetrically small component of the structure of the maria and impact melt deposits, they provide potentially important sites for human exploration.

3.5.4. Background variability. Surprisingly, the dominant signal in the high degree (>80) Bouguer gravity data from GRAIL is in the form of pervasive, small-scale, and seemingly random gravity anomalies (Jansen et al. 2017). These anomalies are most clearly seen in

filtered gravity or gravity gradient maps (Fig. 8), in which they are comparable in magnitude to many discrete structures of comparable size such as the linear intrusions, ring dikes around basins, and lava tubes. This small-scale variability poses a major challenge to studies of the structure of the crust, since it contaminates, and potentially overwhelms, the signal of all structures smaller than ~70 km in scale. This variability can be circumvented by techniques such as averaging across large numbers of similar structures (e.g., as done for craters by Soderblom et al. 2015), or averaging along lines or axes of symmetry (e.g., as done for the linear gravity anomalies by Andrews-Hanna et al. 2013). However, other discrete small density anomalies without known locations or symmetries (e.g., lava tubes or intrusions) may be lost in this variability despite the high quality and resolution of the data.

This background variability is also an important signal in its own right, providing information about the small-scale heterogeneity of the upper crust. Inversions of the small-scale gravity anomalies find they are consistent with small-scale density anomalies with magnitudes of ±100–200 kg/m^3 at scales of 10's of km embedded within the top ~20 km of the crust (Jansen et al. 2017). These anomalies can be attributed to variations in the porosity of the crust, with likely contributions from variations in crustal composition and from the presence of small intrusive bodies. Taken together, small scale gravity and density anomalies, large-scale lateral variations in crustal density (Wieczorek et al. 2013), vertical variations in density (Besserer et al. 2014), and a range of densities at the scale of hand samples returned by the Apollo astronauts (Kiefer et al. 2012) provide evidence for lateral and vertical variations in the density of the crust of 100's of kg/m^3 at scales ranging from centimeters to 1000's of kilometers. In this sense, the Moon provides important lessons for the study of other planets for which an abundance of samples and high-resolution gravity data do not exist—density variability at all scales is the rule rather than the exception.

4. DEEP STRUCTURE: MANTLE AND CORE

The deep interior structure is primarily revealed by seismic analyses of deep moonquakes, combined with geodetic data from lunar laser ranging and gravity analyses. The structure of the upper mantle is perhaps best revealed by analyses of seismic travel times, while the lower mantle and core are better revealed by geodetic data. For a recent review of lunar seismology, see Lognonné and Johnson (2015). Precision laser ranging to reflectors on the lunar surface provides information on the lunar orbit, rotation, and solid-body tides. Lunar rotational variations exhibit strong sensitivities to the moments of inertia and gravity field, while weaker variations (including tidal) exhibit sensitivity to the interior structure, physical properties, and energy dissipation. Energy dissipation is typically measured using the quality factor (Q), with a value that depends on the timescale, from seismic, to monthly and annual tidal timescales. All inferences of the deep interior structure are affected by the distribution of the surface-based geophysical observations over a narrow region of the nearside, and thus much of the discussion in this section is strictly applicable only to the nearside.

4.1. Upper mantle structure

A number of studies have noted a possible seismic discontinuity at a depth of ~400–750 km. Early analyses of travel time data found evidence for a substantial decrease in shear velocity in a transition zone between 400 and 480 km depth, accompanied by a modest decrease in P wave velocity, interpreted as being indicative of a change in the composition of the mantle (Goins et al. 1981). Subsequent studies using a different subset of moonquakes instead found evidence for an increase in velocities at 500–560 km depth (Fig. 9; Nakamura et al. 1982; Khan et al. 2000). An independent inversion of a smaller number of moonquakes found velocities decreasing gradually with depth in the upper mantle, before a larger increase in P wave velocity at a depth of ~750 km (Lognonné et al. 2003; Gagnepain-Beyneix et al. 2006).

However, exclusion of the 5 deepest moonquakes in Lognonné et al. (2003) yielded a shallower discontinuity at ~500 km similar to previous studies, leading to the conclusion that the increase in *P* wave velocity may be either discrete or gradational, and occurs at a depth that is poorly constrained. It should be noted that these models constrained the velocities to be constant within thick layers, and thus any changes in velocity will appear as discontinuities regardless of their true form. Disagreements between different models in the structure of the mid-mantle may be largely attributed to the poor ray coverage at these depths, as well as uncertainty in picking arrival times from the data (Lognonné and Johnson 2015).

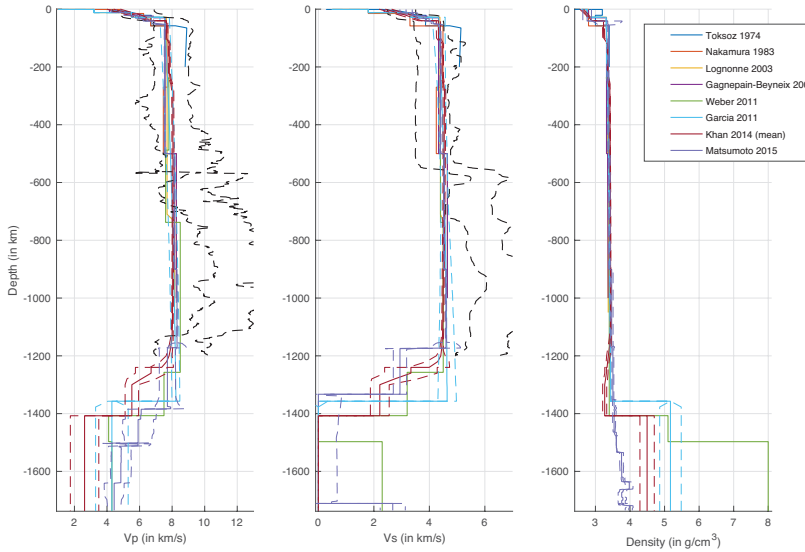

Figure 9. A comparison of multiple models for seismic p- and s-wave velocities and density through from the surface to center of the planet. **Dashed lines** indicate the 1-σ range, or (for the **black lines**) the 50% of the models with the highest probability density (Khan and Mosegaard 2002). [Used by permission of Springer Nature, from Garcia et al. (2019), Space Sci Rev, Vol. 215:50, Fig. 4, p. 13.]

A thermochemical and physical model derived from joint inversions of seismic data along with constraints on the lunar mass and moments of inertia (Khan et al. 2007), found a lower velocity upper mantle down to 250 km depth, but no significant change in *P* wave velocity at greater depths and only a slight decrease in *S* wave velocity due to increasing temperatures at depth. A compositional increase in density at ~500 km depth without an increase in velocity is possible, associated with an increased fraction of garnet in the models (Khan et al. 2007). A model based on inversion of mass, moment of inertia, Love number, and electromagnetic data predicted variations in mantle mineralogy in the upper ~300 km of the mantle, needed to reproduce inferred gradients in seismic velocity and electrical conductivity, but nearly constant seismic velocities below ~300 km depth (Khan et al. 2014). An alternative inversion of seismic and geodesic constraints favored a continuous increase in seismic velocity through the mantle, but this cannot be taken as a strong argument against a discontinuity since that model assumed a uniform mantle composition (Garcia et al. 2011) and results in the prediction of an inverted temperature profile (Kuskov et al. 2014). An analysis of the thermal and compositional structure of the mantle based on multiple seismic models found that the lower mantle below ~750 km depth must be enriched in Ca and Al relative to the upper mantle in order to predict plausible temperature distributions with depth based on the seismic velocity models (Kuskov et al. 2014, 2019).

Thus, most studies support some change in properties of the lower mantle, but there is continued disagreement regarding the depth, nature, and magnitude of that change. The transition occurs at a depth of 500–750 km, may be either gradational or discrete, and could even involve a change in density without a change in seismic velocity. Thus, the "500-km seismic discontinuity" may not occur at 500 km, may not require a change in seismic velocity, and may not be a discontinuity. This structure, if real, is perhaps best referred to as the mid-mantle transition. The details of this transition are clearly sensitive to the chosen datasets, events, arrival times, and methodology.

If a transition at 500–750 km depth exists, it may indicate a change in composition (Goins et al. 1981; Kuskov et al. 2019) or phase (Nakamura 1983; Hood 1986). A natural interpretation is that this seismic transition represents the maximum depth of the lunar magma ocean (Nakamura 1983; Lognonné et al. 2003). This interpretation is supported by the compositional model of Kuskov et al. (2014, 2019), with the enriched lower mantle interpreted as primitive material that did not take part in the magma ocean. As discussed above, some models of magma ocean crystallization combined with estimates of the present-day crustal thickness support a range of magma ocean thicknesses of ~340–890 km, encompassing the range in depths of the mid-mantle transition from multiple seismic analyses (500–750 km). Alternatively, it is noteworthy that models of the overturn of the post-magma ocean cumulates predict a strong density increase (~200–300 kg/m^3) within the overturned cumulate pile at a depth of ~700 km for a 1000-km-deep magma ocean, representing the overturned orthopyroxene, clinopyroxene, and dense oxides (including ilmenite) that crystallized during late crustal formation (Elkins-Tanton et al. 2011). If only the magma ocean cumulates participated in the overturn, the mid-mantle transition might represent this oxide-enriched layer sitting at the base of the overturned cumulate pile but above the underlying primitive lower mantle, and the seismic transition may occur at a depth several hundred kilometers above the base of the magma ocean. If the ilmenite-bearing cumulates sank to the core–mantle boundary (Zhong et al. 2000; Parmentier et al. 2002; Stegman et al. 2003), then a seismic discontinuity at the transition from the remaining magma ocean cumulates to the underlying primitive mantle may again be several hundred kilometers shallower than the initial magma ocean. Clearly, considerable uncertainty exists in seismic interpretations, models of magma ocean crystallization, and any relationships drawn between the two.

Alternatively, the mid-mantle seismic discontinuity may represent the maximum depth of melting of the mare basalt source regions (Wieczorek and Phillips 2000), which is also compatible with the transition from depleted upper mantle to fertile lower mantle (Kuskov et al. 2014). Some thermochemical evolution models predict convection to be limited to depths below ~500–800 km with conductive heat transport at shallower levels (see summary below), and thus a transition at this depth range from stratified magma ocean cumulates to a more homogenous mixed lower mantle might also be expected. At this point, both the existence of and explanation for a mid-mantle transition remain elusive.

4.2. Lower mantle structure

Due to the dearth of seismic ray paths penetrating below ~1200 km depth, structure models derived from primary *P* and *S* wave arrivals are not well constrained in the deep interior, and vary widely between studies (Fig. 9). Early seismic studies suggested the presence of a partial melt layer at the base of the mantle as a possible explanation for the high attenuation of *S* waves at depths below ~1000 km (Nakamura et al. 1974). This interpretation is supported by a reanalysis of Apollo seismic data (Weber et al. 2011), which used array analysis techniques to identify reflections from deep interfaces associated with the core. That study found reflections bounding a low velocity region interpreted as a partial melt zone between radii of 480 ± 15 km and the core–mantle boundary at 330 ± 20 km. The velocity reductions are consistent with melt fractions of 5–30% in this layer (Weber et al. 2011). The tidal response of the Moon to the Earth has also

been used to support a partial melt zone. Models of the tidal love numbers (k_2, k_3, and h_2) and dissipation Q (Harada et al. 2014, 2016) support a low-viscosity partial melt layer extending out to 540–560 km radius. Inversions using mass, MOI, seismic data, k_2, Q, and electromagnetic sounding data support a partial melt layer with a thickness of 150–200 km extending out to a radius of ~490 km with a density of 3250–3450 kg/m^3 due to elevated concentrations of FeO and TiO_2 (Khan et al. 2014). A low viscosity and high density partial melt layer may be consistent with the presence of ilmenite bearing cumulates enriched in heat producing elements that may have existed above the core–mantle boundary early in lunar history (Stegman et al. 2003) and may persist to the present day (Zhang et al. 2017; Mallik et al. 2019).

Not all analyses require or support the existence of this partial melt layer. A low-velocity (and low-rigidity) layer that is distinct from the overlying mantle is not required to explain the seismic and monthly Q and the tidal Love numbers k_2 and h_2 (Nimmo et al. 2012). Karato (2013) found that the electrical conductivity and tidal Q of the Moon can be explained by mantle water contents similar to the Earth's asthenosphere without invoking partial melt. Melt fractions above 1% may be difficult to keep entrained in the mantle (Karato 2013), though a neutrally buoyant melt or melt trapped along grain boundaries could be stable (Weber et al. 2011). Inversions using mass, MOI, k_2 and h_2 found no preference for the inclusion of a transition zone above the core, and concluded that if such a layer exists, it has a rigidity comparable to the rest of the mantle (Matsuyama et al. 2016). One inversion of seismic data, mass, moment of inertia, and monthly and annual Q factors found evidence for a layer of low viscosity and high density material above the core, but could not conclude whether it was molten or not (Matsumoto et al. 2015). The density of this highly dissipative layer was estimated to be ~3500 kg/m^3, consistent with ilmenite-rich material formed at the top of the mantle during magma ocean solidification that sank to the core–mantle boundary during mantle overturn (Elkins-Tanton et al. 2011). The thermodynamic–seismic inversion of Kuskov et al. (2014) argued that the combination of P and S wave velocities, density, and temperature inferred from seismic analyses are incompatible with partial melt in the lower mantle. Thus, although multiple geophysical analyses support or are compatible with the presence of a low-velocity and highly dissipative partial melt layer extending from the core–mantle boundary to a radius of 480–560 km, a number of studies find that partial melt is either not required by or not compatible with the data, and challenges remain to explain the existence of partial melt in the deep lunar mantle.

4.3. Moonquakes

Moonquakes not only provide important seismic sources for probing interior structure, their very existence has important implications for the deep structure of the Moon. Deep moonquakes have hypocenter depths of 750–1200 km, primarily on the nearside with the exception of some moonquake nests located near the limb (Khan and Mosegaard 2002; Lognonné et al. 2003; Nakamura 2003). The relative lack of observed seismicity from the Moon's farside indicates either that the farside is aseismic, or that the center of the Moon is highly attenuating, possibly due to the presence of a partial melt region in the lower mantle (Nakamura 2005). Either scenario is possible, given the highly asymmetric compositional and thermal structure of the lunar interior (Wieczorek and Phillips 2000; Laneuville et al. 2013), and evidence for a partial melt zone above the core (Weber et al. 2011). The correlation of deep moonquake cluster hypocenters with the locations of mare basalts on the surface has been used to argue that deep moonquakes delineate the present-day locations of ilmenite cumulate and olivine–orthopyroxene mixtures, representing potential source regions for the maria (Qin et al. 2012). These mixtures could contain high concentrations of volatiles compared to the overlying material, permitting partial melting due to decreased solidus temperatures.

The mechanism responsible for the deep moonquakes remains controversial. It is perhaps noteworthy that the uppermost extent of the deep moonquake distribution (747 km;

Nakamura 2005) corresponds approximately with one estimate of the depth of the mid-mantle transition (750 km; Lognonné et al. 2003), hinting at a possible relationship between the two. The lowermost extent of deep moonquakes of ~1200 km is consistent with amplified tidal strain rates above a liquid outer core (Lognonné and Johnson 2015; Kawamura et al. 2017) or partially molten mantle layer (Harada et al. 2016). Despite the high temperatures at those depths, brittle failure and seismicity rather than ductile deformation may be favored due to the high tidal strain rates (Kawamura et al. 2017). The partial melt itself may cause cracking at the base of the mantle (Harada et al. 2016). Alternatively, the presence of volatiles may permit a processes known as dehydration embrittlement (Frohlich and Nakamura 2009). Weber et al. (2009) suggested the possibility of a pressure/temperature material phase transition leading to a failure process known as transformational faulting, which is demonstrated via laboratory experiments for the olivine/spinel transition on Earth (Burnley and Green 1989; Frohlich 2006). However, if this process occurs on the Moon, it must be for some other phase transition, because pressures are too low for the olivine/spinel transformation.

4.4. Mantle structure—electromagnetic constraints

Electromagnetic (EM) sounding of the interior of the Moon was accomplished by simultaneous measurement of the magnetic field distant from the Moon using Explorer 35 and at the surface at the Apollo 12 and Apollo 15 sites (see Sonett 1982, for a review). Simultaneous measurement of magnetic fields close to and far from a body (the magnetic transfer function) is the simplest way to separate the source and induced fields and determine the electrical conductivity of the object. Because the outer portions of the Moon are both extremely dry and relatively cold, electrical conductivity is so low that EM signals even at the highest recorded frequency (~30 mHz) penetrate a few hundred kilometers before inducing measurable eddy currents. Hence there are large uncertainties in the electrical properties of the lunar crust and uppermost mantle. Conversely, the lowest frequencies (<0.1 mHz) fully penetrate the Moon but are relatively insensitive to the innermost quarter or so of the radius at the accuracy of the Apollo-Explorer data. As a result, the lower part of the upper mantle, as well as most of the lower mantle, are well-constrained from this first-generation EM-sounding experiment.

Conductivity-depth profiles for the Moon vary because different workers (e.g., Sonnett et al. 1972; Dyal et al. 1976; Hood et al. 1982; Khan et al. 2006; Grimm 2013) used different source signals (direct exposure to the solar-wind magnetic field, measurement in the lunar wake cavity, or fluctuations in Earth's magnetotail), methodologies (time vs frequency domain), bandwidths, or model assumptions. Nonetheless, the overall trends are consistent (see Fig. 15 of Banerdt et al. 2014), with conductivity increasing exponentially over a factor of about 100 between depths of ~400 and ~1200 km.

In the absence of interconnected fluids or metal, electrical conductivity is controlled by the point-defect chemistry of minerals, with a strong temperature dependence (see Tyburczy 2007, for a review). Aluminum substitution in orthopyroxene was originally favored to explain the relatively high conductivity of the lunar mantle while maintaining subsolidus temperatures (Hood and Sonett 1982), but the inferred amount of alumina likely is inconsistent with the Moon's bulk composition and plausible partition coefficients (Grimm 2013). A higher iron content (magnesium number ~80 in olivine), or trace quantities of water can also produce high enough electrical conductivity to match the EM sounding data (Grimm 2013). The presence of partial melt can also greatly increase the conductivity, but, aside from a possible deep partial melt zone and perhaps the sources of young irregular mare patches (Braden et al. 2014), melt is not expected within the majority of the lunar mantle today (Grimm 2013; Laneuville et al. 2013). For a given composition, the conductivity profile can be related to the temperature profile, anchored to the surface temperature and constrained to lie below the solidus (Hood and Sonett 1982; Khan et al. 2006). As discussed further below, the high conductivities imply a warm mantle.

Lateral heterogeneity in electrical conductivity was inferred by Schubert et al. (1974) from the polarized response above 5 mHz at Apollo 15 compared to Explorer 35. Schubert and colleagues suggested this was due to Mare Imbrium or Mare Serenitatis, but we can now identify the likely source of heterogeneity as the PKT. The orientation of the induced magnetic field roughly radial to PKT is consistent with eddy currents circulating around the anomalous region at depths up to a few hundred kilometers.

4.5. Core

Despite the low bulk density of the Moon, multiple datasets show clear evidence for the presence of a small metallic core. Although a dense core composed of late-stage magma ocean cumulates, including ilmenite and Fe-rich cumulates, is possible (Hess and Parmentier 1995; de Vries et al. 2010), geophysical constraints favor a metallic iron core. The Lunar Prospector magnetometer detected an induced moment in the Earth's geomagnetic tail, supporting the existence of a conducting metallic core of radius 340 ± 90 km, or 1 to 3% of the lunar mass (Hood et al. 1999). An induced magnetic field detected by the magnetometer on the Kaguya spacecraft resulted in a core radius estimate of 290 (−120, +60) km, with an upper bound of 400 km (Shimizu et al. 2013).

Two studies searched for seismic reflections from the deep interior in the Apollo seismic data by filtering, shifting, and stacking seismograms, similar to array processing techniques in terrestrial seismology (Garcia et al. 2011; Weber et al. 2011). Both studies found evidence for a core based on these reflections. The latter study found a fluid outer core and solid inner core with radii of 330 ± 20 km and 240 ± 10 km, respectively, overlain by a partial melt layer extending to 480 ± 15 km radius as discussed above (Figs. 1 and 9; Weber et al. 2011). While these models are affected by a tradeoff between the radii of the layers and the assumed velocity above each interface, the seismically determined core radius agrees well with the earlier core radius determined from magnetic data (Hood et al. 1999). The strong attenuation of seismic waves in the deep interior and/or the limited distribution of farside moonquakes, combined with the paucity of seismic station coverage offered by Apollo, prohibits identification of core-transmitted phases containing information on the physical properties of the core.

One analysis of the mass, moment of inertia, and Love numbers supported a fluid outer core radius of 200–380 km, and solid inner core radius of 0–280 km (Williams et al. 2014). An inversion of the same data found inner core and outer core radii of 134 (+41, −128) km and 265 (+97, −71) km, respectively, or radii of 203 (+146, −62) km and 373 (+25, −43) km if the model is assumed to not contain a lower mantle transition layer (Matsuyama et al. 2016). A similar inversion without a transition layer yielded radii of 166 (+121, −80) km and 314 (+47, −38) km for the inner and outer core, respectively (Matsumoto et al. 2015). Although some studies cannot rule out fully molten cores (Williams et al. 2014; Matsuyama et al. 2016), core crystallization may be required to explain the presence of a lunar dynamo in the past (see Wieczorek et al. 2023, this volume).

5. THERMAL AND GEODYNAMIC EVOLUTION

The structure of the Moon is intimately related to its thermal and geodynamic evolution. As with the physical structure, constraints on the thermal state are hampered by the limited distribution of surface measurements on the nearside. The thermal and geodynamical evolution of the Moon through time is illuminated by thermochemical evolution models, which rely heavily on assumptions regarding the vertical and lateral distribution of heat producing elements and the density structure of the mantle, and must satisfy constraints from the history of volcanism and of the magnetic dynamo. Thus, uncertainties regarding the depth of the magma ocean, the nature of magma ocean cumulate overturn, the present-day density structure of the

mantle, and the structure of the Procellarum KREEP terrane map directly into uncertainties in lunar thermal and geodynamic evolution. Nevertheless, the past decade has seen substantial advances in our understanding the thermal state and thermochemical evolution of the Moon.

5.1. Lunar heat flow and subsurface temperatures

5.1.1. Surface measurements. The most direct observational constraint on the thermal structure of the Moon is the measured value of the near-surface heat flow. The Heat Flow Experiment (HFE) was successfully deployed at Apollo 15 and 17. The HFE used boreholes drilled to depths of 1.5–2.5 meters, and a probe with thermocouples at a variety of depths. The temperature in the upper ~1 m of the borehole strongly varies due to changing solar illumination over the course of the lunar day and year, resulting in diurnal and annual thermal waves that can be used to estimate the thermal diffusivity and conductivity (the latter calculated using the measured density and heat capacity of the drill core samples that were returned to Earth) (Langseth et al. 1972, 1973, 1976). The derived thermal conductivities from annual variations are ~0.01 W m^{-1} K^{-1}, with some variations among the four boreholes. Larger values of thermal diffusivity and conductivity were calculated from transient changes in regolith temperature due to active heating, but measure over a smaller volume and are more affected by compaction of the lunar regolith during drilling of the HFE borehole (Langseth et al. 1976; Grott et al. 2010) Future heat flow experiments opting to use active heaters to constrain the thermal diffusivity must either use longer duration heating (Grott et al. 2010) or narrower probes that do not as greatly affect the physical properties of the surrounding regolith (Nagihara et al. 2014). Below ~1-meter depth, the temperature is less variable with time, and the vertical temperature gradient and thermal conductivity can be used to determine the heat flow from the interior. Based on data through the end of 1974, the heat flow was calculated as 21 mW m^{-2} at the Apollo 15 landing site and 14 mW m^{-2} at the Apollo 17 landing site (Langseth et al. 1976). Nagihara et al. (2018) recently recovered and calibrated previously unanalyzed HFE data from 1975 to 1977. This newly restored data shows a systematic long-term warming trend as a result of astronaut-induced perturbations to the thermal properties of the regolith, but this would have little effect on the heat flow determined from early measurements.

With the existence of only two in-situ heat flow measurements for the Moon, and evidence that the distribution of heat-producing elements varies widely across the lunar surface (Jolliff et al. 2000), models that place these measurements in the context of regional variations in lunar structure are of crucial importance. Both the Apollo 15 and 17 landing sites were located near the rims of major impact basins, where the differences in thermal conductivity between high porosity, low conductivity highland rocks and low porosity, high conductivity mare basalt can act as a thermal shunt and locally enhance the heat flow (Warren and Rasmussen 1987). Based on their estimate of the magnitude of this effect at the Apollo 17 HFE site, Warren and Rasmussen (1987) estimated that 12 mW m^{-2} may be a more representative regional heat flow average. Perhaps more significantly, heat flow values at Apollo 15 and to a lesser extent at Apollo 17 are likely elevated by proximity to the Procellarum KREEP Terrane, within which high concentrations of heat producing elements in the crust and/or upper mantle likely lead to higher heat flow (Wieczorek and Phillips 2000). The Apollo 15 and 17 HFE observations can be fit by a model with 10 km of KREEP-basalt at the base of the crust (Wieczorek and Phillips 2000). However, the predicted temperatures in the mantle may be divergent with other geophysical constraints (Grimm 2013; see below). The most detailed model of laterally varying lunar heat flow is that of Siegler and Smrekar (2014), who modeled thermal conduction in the upper 150 km of a 2700 by 1500 km region encompassing the Imbrium and Serenitatis basins. They incorporated lateral variations in crustal radioactive heating using crustal thickness derived from GRAIL gravity and thorium measured by the Lunar Prospector Gamma Ray Spectrometer, and included the effects of basin ejecta on lateral variations in near-surface thermal conductivity. Their preferred models, constrained by the Apollo 15 and 17 HFE data, suggest that the heat flow out of the lunar mantle

in the Imbrium/Serenitatis region is 9–13 mW m^{-2}, which is consistent with a mantle whose radiogenic element content is similar to Earth's. However, this estimate is sensitive to the size, thickness, and radiogenic element concentration of the KREEP-rich material at depth.

5.1.2. Constraints on mantle temperatures. Seismic models also provide insight into mantle temperatures, after either assuming or solving for the mantle compositional structure. Temperatures in the upper mantle derived from multiple seismic models between ~250–500 km depth range from 600–1050 °C, and predicted temperatures at depths of 500–750 km depth generally range from 950–1200 °C (Lognonné et al. 2003; Gagnepain-Beyneix et al. 2006; Khan et al. 2007; Kuskov et al. 2014), though a range as wide as 650–1500 °C is predicted by one study (Kuskov et al. 2014). However, temperature models based on seismic data are strongly sensitive to the assumed composition (e.g., Kuskov et al. 2014). Some preliminary attempts at seismic tomography using *P* and *S* wave arrivals from a variety of seismic signals have been undertaken (Zhao et al. 2012). Those models are under-constrained, but do predict a low-velocity zone in the upper mantle beneath the PKT that is consistent with geodynamic expectations of elevated temperatures in this region (Laneuville et al. 2013) and some travel-time inversions (Khan et al. 2014).

Electromagnetic data provide an independent constraint on mantle temperature, but require careful consideration of mantle mineralogy as well as trace chemistry (see earlier discussion). The high electrical conductivity of the lunar nearside requires elevated temperatures, with temperatures of up to 1100 °C from 250–500 km depth, and of 600–1300 °C from 500–750 km depth (Hood et al. 1982). An independent inversion of electromagnetic data yielded temperatures of approximately 450–1000 °C from 250–500 km depth, and 600–1200 °C from 500–750 km depth. A later inversion of both geodetic and electromagnetic data found temperatures of 1000–1200 °C from 250–500 km depth, and 1200–1300 °C from 500–750 km depth (Khan et al. 2014). However, that study did not account for the effect of varying the Al content in orthopyroxene, or the Fe content in olivine, which has a large effect on conductivity.

Mantle temperatures can also be constrained by the inferred temperatures in the mare basalt source regions at the time of the eruptions of ~1300–1600 °C between 250–500 km at the time of those eruptions (Elkins-Tanton et al. 2004). Analysis of the youngest known basalt samples (~3 Ga) also offers an insight into temperature evolution of the mantle source. Elardo et al. (2015) have shown that at ~3 Ga, melting still occurred within the same mantle depth range that produced crystalline mare basalt for the previous ~1 Ga. Temperatures at the time of the mare eruptions may have been 150 °C cooler than those of today due to the slow warming beneath the PKT (Wieczorek and Phillips 2000), though that model neglected the advection of heat due to melt extraction. For more details about magmatic constraints on temperature, see Shearer et al. (2023, this volume).

Thermal models assuming a 10-km-thick layer of KREEP basalt at the base of the crust predict present-day temperatures of ~1100–1400 °C and 1400–1500 °C over depth ranges of 250–500 km and 500–750 km, respectively (Wieczorek and Phillips 2000; Laneuville et al. 2013). These temperatures are in accord with the mare basalt source region temperatures, and the models also match the measured surface heat flow (see above). Predicted temperatures for the farside mantle (with no KREEP layer) are 500–900 °C from 250–500 km depth, and 900–1300 °C from 500–750 km depth. However, thermal models indicate that a 10-km-thick KREEP layer below the crust in the PKT predicts overly high electrical conductivities for any composition (Grimm 2013). A large concentration of KREEP beneath the crust of the PKT may also result in gravity and topography anomalies that are difficult to reconcile with observations (Grimm 2013), though the topography may be partially offset by thinning of the nearside crust (Laneuville et al. 2013). It may be possible to satisfy constraints from gravity and topography as well as electrical conductivity in a model with some combination of a somewhat lesser amount of KREEP distributed throughout the crust, a thick insulating megaregolith, an

elevated concentration of heat producing elements in the mantle, and/or an enhancement in the electrical conductivity of the mantle due to an elevated iron or hydrogen content (Grimm 2013). Similarly, the heat flow from the upper mantle of 3.8–4.7 mW m^{-2} based on seismic models (Kuskov et al. 2014) is much lower than both the measured surface heat flow from the Apollo HFE and the upper mantle heat flow from thermal models (Siegler and Smrekar 2014).

In summary, some constraints on mantle temperature from geophysical data predict somewhat lower nearside temperatures than those inferred from thermal models and from the mare basalt source regions, though all approaches allow for a wide range of values. Thus, despite an abundance of geophysical and surface remote sensing data and substantial progress in inverting these datasets separately and in combination, there remains substantial uncertainty in the thermal structure of the nearside crust and mantle, which is strongly dependent upon the vertical and lateral distribution of radiogenic elements within and beneath the PKT, and the vertical and lateral variations in thermal conductivity. Additional geophysical data from both within and outside of the PKT may be required to resolve this matter.

5.2. Thermochemical evolution

5.2.1. The thermal state of the Moon following the magma ocean. The geodynamic evolution of the Moon, from accretion to present day, remains a controversial and poorly understood topic. Uncertainty in the course of lunar evolution throughout its history is rooted in the uncertainty regarding both the giant impact(s) responsible for its formation and the details of its accretion, since the evolution of the Moon through time is sensitive to the initial depth of the magma ocean and the thermochemical state of the interior after its solidification. The earliest geodynamic and thermochemical evolution is discussed above in the context of the global-scale patterns of crustal structure and compensation, and is only briefly reviewed here. The earliest thermal evolution of the Moon may have involved a substantial component of tidal heating when the Moon was much closer to the Earth, with the heat generated within a floating plagioclase crust above the final remnants of the magma ocean dominating over radiogenic heat for the first 10^4 years of lunar evolution (Meyer et al. 2010; Elkins-Tanton et al. 2011; Tian et al. 2017). This tidal heating may have led to a spherical harmonic degree-2 pattern of crustal thickness (Garrick-Bethell et al. 2010, 2014). Following the crystallization of the magma ocean, the cumulates may have been buoyantly unstable, leading to some form of gravitationally driven overturn (Warren 1985; Spera 1992; Hess and Parmentier 1995; Elkins-Tanton et al. 2011). This overturn may have first taken the form of a spherical harmonic degree-one Rayleigh–Taylor instability, concentrating the dense ilmenite-rich cumulates and KREEP-rich late stage magma ocean products beneath the crust in one hemisphere before they sank into the interior (Parmentier et al. 2002).

The thermal state at the end of the magma ocean phase is strongly dependent upon the depth of the magma ocean, with models of a shallow magma ocean predicting a cool interior overlain by the warmer magma ocean cumulates, while models of a global magma ocean predict a hotter interior throughout (Solomon and Chaiken 1976; Solomon 1977). Thermal equilibration following crystallization of a shallow magma ocean would lead to an early phase of extension followed by modest contraction, consistent with the small net global contraction recorded at later times in the wrinkle ridges and young lobate scarps (Solomon and Chaiken 1976; Solomon 1977; Watters et al. 2010) and the global set of ancient dike-like intrusions indicating a horizontally extensional stress state in the pre-Nectarian (Andrews-Hanna et al. 2013). In contrast, complete melting of the Moon leads to the prediction of substantial global contraction in contrast with the tectonic constraints (Solomon and Chaiken 1976). However, as noted above, avoiding complete melting of the Moon may be difficult given recent models of more energetic Moon-forming impacts (Canup 2012; Ćuk and Stewart 2012; Lock et al. 2018). Alternatively, while it remains to be tested, the formation of the Moon from multiple impacts (Rufu et al. 2017) might be capable of avoiding a completely molten Moon. Sinking of KREEP-

rich material with the ilmenite to the core–mantle boundary provides an alternative mechanism to cause an early period of global warming and expansion (Zhang et al. 2013a). Although the details remain uncertain, at the end of magma ocean crystallization and overturn, the lunar interior is expected to have been in a state of pronounced thermal disequilibrium, with a thermal inversion between cool dense ilmenite-rich cumulates above the core–mantle boundary, and warm buoyant olivine- and orthopyroxene-rich cumulates beneath the crust (Elkins-Tanton et al. 2011; Evans et al. 2014), as well as a possible cool undifferentiated lower mantle. An early period of global expansion could also be the result of the evolving density of the interior during magma ocean crystallization, or a later net increase in volume during the overturn and subsequent partial melting of the magma ocean cumulates (Elkins-Tanton and Bercovici 2014).

5.2.2. Thermochemical evolution of the lunar interior. The thermal and compositional evolution of planetary interiors are commonly investigated through the use of fluid dynamical thermochemical evolution models, which jointly solve conservation equations of mass, momentum, and energy (see review by Ricard 2007). Such models, when appropriately constrained by information derived from surface and remote sensing observations, can provide valuable insights into how the lunar interior evolved from a fractionally crystallized magma ocean to its present state. Investigations of the lunar interior evolution generally focus on elucidating the history of lunar volcanism, the asymmetric thermal evolution between the nearside and farside hemispheres, and the persistence of a lunar core dynamo. These investigations apply inferred constraints from a variety of sources, including magma ocean models (see Gaffney et al. 2023, this volume), the high titanium content of some mare basalts, the surface distribution of heat producing elements, the measured heat flow at the surface, the protracted history of mare volcanism and intrusive activity (see Head et al. 2023, this volume; Shearer et al. 2023, this volume), seismic data, and the magnetization of lunar materials and history of the dynamo (see Wieczorek et al. 2023, this volume) to understand which predictions are most compatible with lunar observations.

The initial density stratification in the mantle can strongly affect its subsequent thermochemical evolution. Models of magma ocean overturn predict a density gradient throughout the mantle due to variations in Mg# and mineralogy, with the post-overturn density increasing by 110–360 kg/m^3 from the top of the mantle to the layer immediately above the ilmenite-bearing cumulates (Elkins-Tanton et al. 2011). These stably stratified compositional density variations in the mantle would have resisted convection. In one model including a density-stratified upper mantle with a post-magma-ocean inverted temperature profile, convection was inhibited altogether in the upper mantle (Evans et al. 2014). Convection in that model was limited to a deep lower mantle layer above the core with reduced viscosity due to either the presence of melt or a local enrichment in water. However, that model neglected the enhanced concentration of heat producing elements beneath the PKT, which would have led to a local increase of the subsurface temperature and hence a lower viscosity beneath the PKT that could have sustained prolonged regional convection (Laneuville et al. 2013). Alternatively, convection and mixing of the solid cumulates may have occurred prior to magma ocean solidification, depending on the assumed magma ocean depth and cumulate viscosity (Maurice et al. 2017, 2020).

Most models of lunar mantle convection have not included initial post-magma-ocean density stratification, with the possible exception of a dense layer of ilmenite-bearing cumulates above the core–mantle boundary (e.g., Spohn 2001; Ziethe et al. 2009; Laneuville et al. 2013; Scheinberg et al. 2015; Zhang et al. 2017). Models assuming a homogeneous mantle predict present-day convection at depths below ~600 km (Ziethe et al. 2009; Scheinberg et al. 2015) and convection at shallower depths earlier in time (Spohn 2001; Ziethe et al. 2009), with heat transport dominantly by conduction through the upper mantle. Inclusion of enhanced radiogenic heating beneath the PKT in an otherwise compositionally uniform mantle results in shallower convection on the nearside (Laneuville et al. 2013), but present-day convection in that model is

limited to depths below 600 km and 800 km on the nearside and farside, respectively. For models that predict present-day convection, the velocities are less than 1 cm/year (Ziethe et al. 2009; Laneuville et al. 2013). Given the potential importance of compositional density gradients in the mantle, the fundamental mode of heat transport of the mantle (convective or conductive) as a function of depth and time depends on the depth of the magma ocean, the details of magma ocean crystallization, the efficiency of density segregation during overturn, and the vertical and lateral distribution of heat producing elements, each of which is poorly constrained.

Putting aside the above uncertainty, one of the strongest observational constraints by which models of lunar thermochemical evolution can be tested is the timing of mare volcanism. Several models assuming convection in a homogeneous mantle successfully predict protracted genesis of mare basalts, predominantly between 3.9 and 3.1 Ga (Spohn 2001; Ziethe et al. 2009). The models predict melt in the mantle capable of persisting to ~2 Ga, but have difficulty explaining mare volcanism as late as 1.2 Ga (Hiesinger et al. 2003, 2010, 2011) and locally as late as < 100 Ma (Braden et al. 2014). However, the above models did not consider the likely enhanced concentration of heat producing elements beneath the PKT, which would lead to regionally elevated temperatures and a longer duration of volcanism. A model of conductive heat transfer beneath the PKT predicts partial melt to persist to the present-day (Wieczorek and Phillips 2000). In the thermochemical convection model of Laneuville et al. (2013), with a KREEP-rich layer beneath the crust of the PKT and taking into account thermal effects of melt extraction, enhanced nearside mantle melting was predicted at depths of up to 600 km until ~200 Ma. The lowering of the melting temperature by the presence of KREEP could also increase the volume and duration of volcanism in this region (Elardo et al. 2020).

For models with enhanced radiogenic heating beneath the PKT, the rates of melt generation exceed the inferred rate of volcanism by several orders of magnitude (Wieczorek and Phillips 2000; Laneuville et al. 2013), but there are large uncertainties in both the efficiency of melt extraction from the mantle and the ratio of intrusive magmatism to extrusive volcanism. The late peak in mare volcanism is not predicted in some models (Wieczorek and Phillips 2000; Ziethe et al. 2009), but is predicted by Laneuville et al. (2013) as a result of the build-up of heat beneath the PKT. However, too thick of a KREEP layer in the nearside mantle may lead to generation of too much melt beneath the crust, which would inhibit the eruption of magma from greater depths (Hess and Parmentier 2001). In general, the predicted magmatic history is affected by trade-offs between the initial temperature profile (a consequence of magma ocean crystallization and overturn) and the concentration and distribution of radioactive heat sources.

Zhong et al. (2000) proposed that a dense layer of ilmenite-bearing cumulates above the core mantle boundary with entrained KREEP-rich material would become warm and buoyant, rising in a spherical harmonic degree-1 diapir to explain both the time delay in the peak of mare volcanism and the concentration of volcanism on the nearside. Although that model was supported by later work (Zhang et al. 2013b), improved data on the ilmenite rheology (Dygert et al. 2016) and modeling of that rheology (Zhang et al. 2017) found that an upwelling of an ilmenite-bearing cumulate layer from the CMB is unlikely. Nevertheless, that model does predict a partially molten ilmenite-rich layer above the CMB consistent with some interpretations of the lower mantle transition zone (Weber et al. 2011; Khan et al. 2014). Future work is needed to consider cases with sequestration of some KREEP at the CMB while some remains near the surface, as well as the combined effects of density stratification in the mantle with regional concentration of heat producing elements in the PKT.

Paleomagnetic evidence for a strong dynamo field between 3.85 and 3.56 Ga, and a weaker field persisting until at least 2.5 Ga provides another constraint on the thermochemical evolution of the interior (Weiss and Tikoo 2014; Wieczorek et al. 2023, this volume). Using a thermochemical evolution model, Stegman et al. (2003) found that if a dense layer of ilmenite-bearing cumulates entrained KREEP material as it foundered to the core–mantle boundary,

the enhanced concentration of heat-producing elements within this layer would temporarily prevent core heat loss and thereby delay the onset of a convective core dynamo. After a few hundred million years, the ilmenite-bearing cumulates may become thermally buoyant due to radiogenic heating, and would rise back into the mantle, leading to a peak in the core heat loss and the surface intensity of the magnetic field at 3.9 Ga, consistent with the peak in paleointensities of lunar samples occurring at that time. However, as discussed above, more recent work has found that buoyant rise of the ilmenite-bearing cumulate layer from the CMB is unlikely (Dygert et al. 2016; Zhang et al. 2017).

Evans et al. (2014) used a mantle thermochemical evolution model coupled with parameterized core model to investigate the interior evolution of the Moon after overturn of the magma ocean cumulates, where the magma ocean was assumed to extend down to a depth of 1000 km. If the post-overturn magma ocean cumulates were underlain by a low viscosity lower mantle due to a local enrichment of water, a long-lived convective core dynamo could persist until 2.5 Ga, consistent with timescales of the latest paleomagnetic data (Weiss and Tikoo 2014; Tikoo et al. 2017). Using a more sophisticated parameterized core model that allowed for inner core crystallization and a heterogeneous core composition, but neglecting the compositional density variations in the mantle aside from a possible ilmenite layer above the CMB, Scheinberg et al. (2015) found that a convective core dynamo could persist until 1.6 Ga.

The longevity of the dynamos predicted by the above models are consistent with the lunar paleomagnetic record, however, the predicted dynamo magnetic field intensities of those models are too low by a factor of ~100 to reproduce the lunar paleomagnetic record. Processes other than thermochemical convection may have also contributed to the lunar dynamo, such as mechanical stirring of the liquid outer core by impacts (Le Bars et al. 2011) or precession of the spin axis (Dwyer et al. 2011). Yet analyses of the energy sources available to power the dynamo indicate that all of the aforementioned dynamo-generation mechanisms fall short of the energy needed based on simple scaling laws (Dwyer et al. 2011; Le Bars et al. 2011; Evans et al. 2018b), suggesting that using only the duration of the dynamo to constrain mantle thermochemical evolution models may be unreliable.

6. SUMMARY AND FUTURE DIRECTIONS

6.1. Summary

The internal structure of the Moon is unique in the Solar System as a result of its formation from an impact-generated debris disk and subsequent differentiation from a magma ocean. These two processes have long been recognized to provide an explanation for the small lunar core and plagioclase-rich crust. The details of the post-magma ocean lunar structure depend upon the depth of the magma ocean, the details of its crystallization, and the nature of the buoyant cumulate overturn. Beyond this first order structure, the interior structure of the Moon reflects a long history of modification by impacts, volcanism, and tectonism. Our understanding of lunar structure has advanced substantially in recent years, driven in large part by both new geophysical datasets and improved analyses of Apollo-era data. Nevertheless, several key fundamental questions regarding the structure and evolution of the lunar interior remain unanswered.

The structure of the crust is now resolved in unprecedented detail by gravity data from GRAIL (Wieczorek et al. 2013; Zuber et al. 2013), with added constraints from continued seismic analyses (e.g., Gagnepain-Beyneix et al. 2006). The low mean density of the upper crust and increase in density and seismic velocity with depth (e.g., Besserer et al. 2014) indicate extensive impact damage of the upper crust. The mixed feldspathic composition of this low density upper crust (e.g., Yamamoto et al. 2012) is consistent with ejecta from giant impact basins, extensive impact excavation and gardening of a thin still-forming floatation crust above a magma ocean during an early declining bombardment phase, and/or floatation of pyroxene as well as plagioclase in the magma ocean (Elkins-Tanton and Bercovici 2014).

The horizontal structure of the crust is dominated by the nearside–farside asymmetry in crustal thickness. Although a number of models have been proposed to explain this asymmetry, ranging from early magma ocean processes (Stevenson 1980; Wasson and Warren 1980) to giant impacts (Byrne 2007; Jutzi and Asphaug 2011), no one model has strong support. Superimposed on this asymmetry, the apparent spherical harmonic degree 2 pattern of crustal thickening may be a result of tidal heating during crustal formation (Garrick-Bethell et al. 2010, 2014). Rotational–tidal effects can also explain the fossil figure of the Moon, though debate continues regarding solutions invoking a high eccentricity synchronous orbit or a higher order resonance (e.g., a 3:2 spin–orbit resonance) (Garrick-Bethell et al. 2014; Keane and Matsuyama 2014).

At regional scales, the South Pole-Aitken basin is the largest unambiguous impact basin and an important structural and geochemical province (Jolliff et al. 2000; Garrick-Bethell and Zuber 2009). On the lunar nearside, the Procellarum region dominates the crustal structure and is associated with a strong geochemical anomaly in the form of the Procellarum KREEP terrane (Jolliff et al. 2000; Wieczorek and Phillips 2000). The concentration of KREEP-rich material within the PKT is clearly a result of late-stage magma ocean processes, though the subsurface structure and time evolution of the PKT remain poorly constrained. The concentration of KREEP on the nearside may be a simple effect of the crustal asymmetry on magma ocean crystallization (Warren and Wasson 1979), or may have formed through a degree-one instability (Parmentier et al. 2002). The Procellarum region has become even more enigmatic with the discovery of a quasi-rectangular set of structures surrounding the region of apparent magmatic-tectonic origin (Andrews-Hanna et al. 2014).

At intermediate scales, the structure of the crust is dominated by the effects of impact basins. New insights into the structure and compensation of impact basins (Neumann et al. 2015; Zuber et al. 2016; Andrews-Hanna et al. 2018) have shed light on both the origin of the basin rings (Potter et al. 2013; Johnson et al. 2016) and the origin of the mascon gravity anomalies present in many basins (Melosh et al. 2013; Freed et al. 2014).

The smallest scales resolved by the gravity data are dominated by structures embedded within the crust rather than variations in the thickness of the crust. Gravity data reveal intrusive bodies associated with volcanoes (Kiefer 2013; Kiefer et al. 2016), dike-like intrusions (Andrews-Hanna et al. 2013), and floor-fractured craters (Jozwiak et al. 2015; Thorey et al. 2015). Gravity data also place new constraints on the thickness of the lunar maria (Evans et al. 2016; Gong et al. 2016) to corroborate earlier geological constraints. However, the gravity anomalies of the smallest structures are likely masked in many places by the pervasive small-scale variability in the gravity field, which can be attributed to variations in the porosity and composition of the crust (Jansen et al. 2017).

Data from the Apollo seismometers, electromagnetic sounding, gravity, and lunar laser ranging constrain the structure of the mantle and core. Within the mantle, many studies favor a mid-mantle transition in physical and/or chemical properties between 500 and 750 km depth, which may be either discrete or gradational in nature (e.g., Khan et al. 2000, 2007; Lognonné et al. 2003; Gagnepain-Beyneix et al. 2006). However, the structure of the mantle at these depths is poorly constrained by existing seismic data (Lognonné and Johnson 2015). If real, this transition occurs at a depth that approximately corresponds with some predictions of the magma ocean thickness required to generate the observed crustal thickness (e.g., Charlier et al. 2018). Alternatively, a mid-mantle seismic transition may represent the depletion of the upper mantle due to mare volcanism, or may represent the transition from a convectively mixed lower mantle to a dominantly conductive upper mantle. A lower mantle transition zone of some sort is indicated by most studies extending from the core–mantle boundary to a radius of 480–560 km, with a number of studies arguing for a low-viscosity partial melt zone (e.g., Weber et al. 2011) and others finding that melt is not required (e.g., Matsuyama et al. 2016).

A liquid outer core exists with an outer radius of 290–400 km, while the presence of a solid inner core is less convincingly demonstrated, with radius estimates of 0–280 km (Weber et al. 2011; Williams et al. 2014; Matsumoto et al. 2015; Matsuyama et al. 2016).

6.2. Outstanding questions and future directions

The abundance of orbital and surface-based geophysical data provides more information on the interior structure of the Moon than is available for any other body besides the Earth. Yet as analyses of these data continue and our understanding of lunar structure is refined, a number of key questions remain unanswered and new questions continue to arise. The spherical harmonic degree one crustal asymmetry is one of the defining characteristics of the Moon and has affected nearly every aspect of its subsequent evolution, yet the cause of this asymmetry remains an open question. The nature and origin of the Procellarum KREEP terrane, including the lateral and vertical distribution of KREEP-rich material and their variation through time, is still poorly understood. The discovery of a quasi-rectangular set of magmatic–tectonic structures surrounding this province provides a strong argument against an impact origin, but opens up new questions regarding the geodynamic evolution of this province. While the crustal structure at intermediate scales, largely associated with impact basins, is reasonably well understood, new questions are arising regarding the smaller scale structures. Pervasive small-scale variability in the gravity field arising from upper crustal density anomalies hampers analyses of small-scale structures.

Fundamental questions also remain regarding the deep structure of the Moon. The existence and implications of a possible mid-mantle transition, and how that transition might relate to the lunar magma ocean or lunar geodynamics are critical issues for understanding the present-day structure, evolution, and origin of the Moon. The nature of the lower mantle transition and the possibility of a partial melt layer above the core are equally important and open questions. Uncertainties in the structure of the lunar mantle translate into uncertainties regarding the subsequent thermochemical evolution of the interior, including the depth, vigor, and time-history of mantle convection. Overshadowing all interpretations of the surface-based seismic, electromagnetic, and heat flow data is the problem of the narrow spatial distribution of Apollo landing sites on the nearside, and the question of whether the structure revealed by these data is representative of the whole Moon or is instead unique to the region surrounding the Procellarum KREEP terrane.

With the wealth of recent geophysical datasets and continued improvements in analyses of existing data, our understanding of lunar structure will continue to improve. Nevertheless, it is clear that surface-based geophysical data from a broader distribution of stations, and from the farside in particular, is a critical need to enable us to answer a number of fundamental questions regarding lunar structure and evolution (Mimoun et al. 2012; Neal et al. 2019). More sensitive seismometers can better constrain core size and properties (Yamada et al. 2013), refine interior structure models, and better locate shallow moonquakes (Neal et al. 2019). A broader distribution of heat flow measurements (Siegler and Smrekar 2014) and electromagnetic sounding (Grimm and Delory 2012) are critical for constraining the lateral distribution of heat producing elements.

The upcoming robotic and human exploration of the Moon provides new opportunities for deployment of surface geophysical instruments. Three of the missions currently in development for NASA's Commercial Lunar Payload Services include demonstrations of all four of the principal instruments of a Lunar Geophysical Network (Neal et al. 2020): two laser retroreflectors, two heat-flow probes, two electromagnetic sounders, and a seismometer. The Artemis III crewed mission may have a geophysical station (Weber et al. 2020). Planned European and Chinese robotic landers also include geophysical instruments. Magnetometers are manifested on several planned and in-development missions. Most of these instruments

are suited to operation at individual surface sites, with their results accumulated into a global database. The exception is seismology, which requires simultaneous operation of a network for optimum application. Seismometers must be able to survive for many years if deployed independently by individual agencies and programs. Alternatively, a coordinated network can be deployed as a single, shorter-duration mission, with the additional advantage of optimizing the sites for seismic coverage and geographic diversity. The data returned by these and other missions will shed new light on the lunar interior.

As we continue to probe and learn about the internal structure of the Moon, we will continue to learn about the origin and evolution of the Earth-Moon system. The Moon also bore witness to the bombardment history of the inner Solar System, and its structure preserves a record of that bombardment. The variety and high quality of geophysical data from the Moon also make it an important testing ground for comparing different datasets and evaluating assumptions made regarding planetary structure more generally. As such, new revelations regarding the structure of the Moon will continue to shed new light on the origin and evolution of the Moon, Earth, and Solar System more broadly.

ACKNOWLEDGMENTS

We are grateful to two anonymous reviewers who helped to improve the clarity and quality of the manuscript.

REFERENCES

Aggarwal HR, Oberbeck VR (1979) Monte Carlo simulation of lunar regolith and implications. Lunar Planet Sci Conf 10:6–8

Andrews-Hanna JC (2016) Re-evaluating the geophysical evidence for a Procellarum impact basin on the lunar nearside. LPI Workshop New Views Moon 2:6061. https://www.hou.usra.edu/meetings/newviews2016/pdf/6061.pdf

Andrews-Hanna JC (2013) The origin of the non-mare mascon gravity anomalies in lunar basins. Icarus 222:159–168

Andrews-Hanna JC, Zuber MT (2010) Elliptical craters and basins on the terrestrial planets. Geol Soc Am Spec Pap 465:1–13

Andrews-Hanna JC, Zuber MT, Banerdt WB (2008) The Borealis basin and the origin of the martian crustal dichotomy. Nature 453:1212–1215

Andrews-Hanna JC, Asmar SW, Head III JW, Kiefer WS, Konopliv AS, Lemoine FG, Matsuyama I, Mazarico E, McGovern PJ, Melosh HJ, Neumann GA, Nimmo F, Phillips RJ, Smith DE, Solomon SC, Taylor GJ, Wieczorek MA, Williams JG, Zuber MT (2013) Ancient igneous intrusions and early expansion of the Moon revealed by GRAIL gravity gradiometry. Science 339:675–678

Andrews-Hanna JC, Besserer J, Head III JW, Howett CJA, Kiefer WS, Lucey PJ, McGovern PJ, Melosh HJ, Neumann GA, Phillips RJ, Schenk PM, Smith DE, Solomon SC, Zuber MT (2014) Structure and evolution of the lunar Procellarum region as revealed by GRAIL gravity data. Nature 514:68–71

Andrews-Hanna JC, Head III JW, Johnson BC, Keane JT, Kiefer WS, McGovern PJ, Neumann GA, Wieczorek MA, Zuber MT (2018) Ring faults and ring dikes around the Orientale basin on the Moon. Icarus 310:1–20

Araki H, Tazawa S, Noda H, Ishihara Y, Goossens S, Sasaki S, Kawano N, Kamiya I, Otake H, Oberst J, Shum C (2009) Lunar global shape and polar topography derived from Kaguya-LALT laser altimetry. Science 323:897–900

Baker DMH, Head III JW, Collins GS, Potter RWK (2016) The formation of peak-ring basins: Working hypotheses and path forward in using observations to constrain models of impact-basin formation. Icarus 273:146–163

Baker DMH, Head III JW, Phillips RJ, Neumann GA, Bierson CJ, Smith DE, Zuber MT (2017) GRAIL gravity observations of the transition from complex crater to peak-ring basin on the Moon: Implications for crustal structure and impact basin formation. Icarus 292:54–73

Banerdt WB, Dehant V, Grimm R, Grott M, Lognonne P, Smrekar S (2014) Probing the interiors of planets with geophysical tools. *In*: Spohn T, Breuer D, Johnson T (eds) Encyclopedia of the Solar System. Elsevier, Amsterdam, p 1185–1204

Besse J, Courtillot V (2002) Apparent and true polar wander and the geometry of the geomagnetic field over the last 200 Myr. J Geophys Res Solid Earth 107:2300

Besserer J, Nimmo F, Wieczorek MA, Weber RC, Kiefer WS, McGovern PJ, Andrews-Hanna JC, Smith DE, Zuber MT (2014) GRAIL gravity constraints on the vertical and lateral density structure of the lunar crust. Geophys Res Lett 41:5771–5777

Bierson CJ, Phillips RJ, Nimmo F, Besserer J, Milbury C, Keane JT, Soderblom JM, Zuber MT (2016) Interactions between complex craters and the lunar crust : Analysis using GRAIL data. J Geophys Res Planets 121:1488–1497
Blair DM, Chappaz L, Sood R, Milbury C, Bobet A, Melosh HJ, Howell KC, Freed AM (2017) The structural stability of lunar lava tubes. Icarus 282:47–55
Blanchette-Guertin J-F, Johnson CL, Lawrence JF (2012) Investigation of scattering in lunar seismic coda. J Geophys Res Planets 117:E06003
Bottke WF, Walker RJ, Day JMD, Nesvorny D, Elkins-Tanton L (2010) Stochastic late accretion to Earth, the Moon, and Mars. Science 330:1527–1530
Braden SE, Stopar JD, Robinson MS, Lawrence SJ, van der Bogert CH, Hiesinger H (2014) Evidence for basaltic volcanism on the Moon within the past 100 million years. Nat Geosci 7:787–791
Burnley PC, Green II HW (1989) Stress dependence of the mechanism of the olivine–spinel transformation. Nature 338:753–756
Byrne CJ (2007) A large basin on the near side of the Moon. Earth Moon Planets 101:153–188
Cadogan PH (1974) Oldest and largest lunar basin? Nature 250:315–316
Cahill JTS, Lucey PG, Wieczorek MA (2009) Compositional variations of the lunar crust: Results from radiative transfer modeling of central peak spectra. J Geophys Res Planets 114:E09001
Canup RM (2004) Simulations of a late lunar-forming impact. Icarus 168:433–456
Canup RM (2012) Forming a moon with an earth-like composition via a giant impact. Science 419:1052–1055
Canup RM, Asphaug E (2001) Origin of the Moon in a giant impact near the end of the Earth's formation. Nature 412:708–712
Canup RM, Visscher C, Salmon J, Fegley B (2015) Lunar volatile depletion due to incomplete accretion within an impact-generated disk. Nat Geosci 8:918–921
Canup RM, Righter K, Dauphas N, Pahlevan K, Ćuk M, Lock SJ, Stewart ST, Salmon J, Rufu R, Nakajima M, Magna T (2023) Origin of the Moon. Rev Mineral Geochem 89:53–102
Castillo-Rogez JC, Matson DL, Sotin C, Johnson TV, Lunine JI, Thomas PC (2007) Iapetus' geophysics: Rotation rate, shape, and equatorial ridge. Icarus 190:179–202
Chappaz L, Sood R, Melosh HJ, Howell KC, Blair DM, Milbury C, Zuber MT (2017) Evidence of large empty lava tubes on the Moon using GRAIL gravity. Geophys Res Lett 44:105–112
Charlier B, Grove TL, Namur O, Holtz F (2018) Crystallization of the lunar magma ocean and the primordial mantle–crust differentiation of the Moon. Geochim Cosmochim Acta 234:50–69
Cheek LC, Donaldson-Hanna KL, Pieters CM, Head JW, Whitten JL (2013) The distribution and purity of anorthosite across the Orientale basin: New perspectives from Moon Mineralogy Mapper data. J Geophys Res Planets 118:1805–1820
Chen J, Ling Z, Li B, Zhang J, Sun L, Liu J (2015) Abundance and distribution of radioelements in lunar terranes: Results of Chang'E-1 gamma ray spectrometer data. Adv Space Res 57:919–927
Chenet H, Lognonné P, Wieczorek M, Mizutani H (2006) Lateral variations of lunar crustal thickness from the Apollo seismic data set. Earth Planet Sci Lett 243:1–14
Chisenga C, Yan J, Zhao J, Atekwana EA, Steffen R (2020) Density structure of the Rümker region in the northern Oceanus Procellarum: Implications for lunar volcanism and landing site selection for the Chang'E-5 mission. J Geophys Res Planets 125:e2019JE005978
Christeson GL, Collins GS, Morgan JV, Gulick SPS, Barton PJ, Warner MR (2009) Mantle deformation beneath the Chicxulub impact crater. Earth Planet Sci Lett 284:249–257
Collins GS (2002) Hydrocode simulations of Chicxulub crater collapse and peak-ring formation. Int J Sol Syst Stud 157:24–33
Cooper MR, Kovach RL, Watkins JS (1974) Lunar near-surface structure. Rev Geophys Space Phys 12:291–308
Ćuk M, Stewart ST (2012) Making the Moon from a fast-spinning Earth: A giant impact followed by resonant despinning. Science 338:1047–1052
Daradich A, Mitrovica JX, Matsuyama I, Perron JT, Manga M, Richards MA (2008) Equilibrium rotational stability and figure of Mars. Icarus 194:463–475
Darwin GH (1880) On the secular changes in the elements of the orbit of a satellite revolving about a tidally distorted planet. Phil Trans R Soc 171:713–891
De Hon RA (1978) Maximum thickness of materials in the western mare basins. Lunar Planet Sci Conf 9:229–231
De Hon RA, Waskom JD (1976) Geologic structure of the eastern mare basins. Proc Lunar Sci Conf 7:2729–2746
de Vries J, van den Berg A, van Westrenen W (2010) Formation and evolution of a lunar core from ilmenite-rich magma ocean cumulates. Earth Planet Sci Lett 292:139–147
Deutsch AN, Neumann GA, Head III JW, Wilson L (2019) GRAIL-identified gravity anomalies in Oceanus Procellarum: Insight into subsurface impact and magmatic structures on the Moon. Icarus 331:192–208
Donaldson Hanna KL, Cheek LC, Pieters CM, Mustard JF, Greenhagen BT, Thomas IR, Bowles NE (2014) Global assessment of pure crystalline plagioclase across the Moon and implications for the evolution of the primary crust. J Geophys Res 119:1516–1545
Dwyer CA, Stevenson DJ, Nimmo F (2011) A long-lived lunar dynamo driven by continuous mechanical stirring. Nature 479:212–214

Dyal P, Parkin CW, Daily WD (1976) Structure of the lunar interior from magnetic field measurements. Proc Lunar Sci Conf 6:3077–3095
Dygert N, Hirth G, Liang Y (2016) A flow law for ilmenite in dislocation creep: Implications for lunar cumulate mantle overturn. Geophys Res Lett 43:532–540
Eckhardt DH (1981) Theory of the libration of the Moon. Moon Planets 25:3–49
Elardo SM, Draper DS, Shearer CK (2011) Lunar Magma Ocean crystallization revisited: Bulk composition, early cumulate mineralogy, and the source regions of the highlands Mg-suite. Geochim Cosmochim Acta 75:3024–3045
Elardo SM, Shearer CK, Vander Kaaden KE, McCubbin FM, Bell AS (2015) Petrogenesis of primitive and evolved basalts in a cooling Moon: Experimental constraints from the youngest known lunar magmas. Earth Planet Sci Lett 422:126–137
Elardo SM, Laneuville M, McCubbin FM, Shearer CK (2020) Early crust building enhanced on the Moon's nearside by mantle melting-point depression. Nat Geosci 13:339–343
Elardo SM, Pieters CM, Dhingra D, Donaldson Hanna KL, Glotch TD, Greenhagen BT, Gross J, Head JW, Jolliff BL, Klima RL, Magna T, McCubbin FM, Ohtake M (2023) The evolution of the lunar crust. Rev Mineral Geochem 89:293-338
Elkins-Tanton LT (2012) Magma oceans in the inner solar system. Annu Rev Earth Planet Sci 40:113–139
Elkins-Tanton LT, Bercovici D (2014) Contraction or expansion of the Moon's crust during magma ocean freezing? Phil Trans R Soc A 372:20130240
Elkins-Tanton LT, Van Orman JA, Hager BH, Grove TL (2002) Re-examination of the lunar magma ocean cumulate overturn hypothesis: Melting or mixing is required. Earth Planet Sci Lett 196:239–249
Elkins-Tanton LT, Hager BH, Grove TL (2004) Magmatic effects of the lunar late heavy bombardment. Earth Planet Sci Lett 222:17–27
Elkins-Tanton LT, Burgess S, Yin QZ (2011) The lunar magma ocean: Reconciling the solidification process with lunar petrology and geochronology. Earth Planet Sci Lett 304:326–336
Evans AJ, Zuber MT, Weiss BP, Tikoo SM (2014) A wet, heterogeneous lunar interior: Lower mantle and core dynamo evolution. J Geophys Res Planets 119:1061–1077
Evans AJ, Soderblom JM, Andrews-Hanna JC, Solomon SC, Zuber MT (2016) Identification of buried lunar impact craters from GRAIL data and implications for the nearside maria. Geophys Res Lett 43:2445–2455
Evans AJ, Andrews-Hanna JC, Head JW, Soderblom JM, Solomon SC, Zuber MT (2018a) Reexamination of early lunar chronology with GRAIL Data: Terranes, basins, and impact fluxes. J Geophys Res Planets 123:1596–1617
Evans AJ, Tikoo SM, Andrews-Hanna JC (2018b) The case against an early lunar dynamo powered by core convection. Geophys Res Lett 45:98–107
Freed AM, Johnson BC, Blair DM, Melosh HJ, Neumann GA, Phillips RJ, Solomon SC, Wieczorek MA, Zuber MT (2014) The formation of lunar mascon basins from impact to contemporary form. J Geophys Res Planets 119:10.1002/2014JE004657
Frohlich C (2006) A simple analytical method to calculate the thermal parameter and temperature within subducted lithosphere. Phys Earth Planet Inter 155:281–285
Frohlich C, Nakamura Y (2009) The physical mechanisms of deep moonquakes and intermediate-depth earthquakes: How similar and how different? Phys Earth Planet Inter 173:365–374
Gaffney AM, Gross J, Borg LE, Donaldson Hanna KL, Draper DS, Dygert N, Elkins-Tanton LT, Prissel KB, Prissel TB, Steenstra ES, van Westrenen W (2023) Magmatic evolution I: Initial differentiation of the Moon. Rev Mineral Geochem 89:103–145
Gagnepain-Beyneix J, Lognonn P, Chenet H, Lombardi D, Spohn T (2006) A seismic model of the lunar mantle and constraints on temperature and mineralogy. Phys Earth Planet Inter 159:140–166
Garcia RF, Gagnepain-Beyneix J, Chevrot S, Lognonné P (2011) Very preliminary reference Moon model. Phys Earth Planet Inter 188:96–113
Garcia RF, Khan A, Drilleau M, Margerin L, Kawamura T, Sun D, Wieczorek MA, Rivoldini A, Nunn C, Weber RC, Marusiak AG, Lognonné P, Nakamura Y, Zhu P (2019) Lunar seismology: An update on interior structure models. Space Sci Rev 215:50
Garrick-Bethell I, Zuber MT (2009) Elliptical structure of the lunar South Pole-Aitken basin. Icarus 204:399–408
Garrick-Bethell I, Wisdom J, Zuber MT (2006) Evidence for a past high-eccentricity lunar orbit. Science 313:652–655
Garrick-Bethell I, Nimmo F, Wieczorek MA (2010) Structure and formation of the lunar farside highlands. Science 330:949–951
Garrick-Bethell I, Perera V, Nimmo F, Zuber MT (2014) The tidal–rotational shape of the Moon and evidence for polar wander. Nature 512:181–184
Glotch TD, Lucey PG, Bandfield JL, Greenhagen BT, Thomas IR, Elphic RC, Bowles N, Wyatt MB, Allen CC, Donaldson-Hanna K, Paige, DA (2010) Highly silicic compositions on the Moon. Science 329:1510–1513
Goins NR, Dainty AM, Toksöz MN (1981) Lunar seismology: The internal structure of the Moon. J Geophys Res 86:5061–5074
Gong S, Wieczorek MA (2020) Is the lunar magnetic field correlated with gravity or topography? J Geophys Res Planets 125:e2019JE006274
Gong S, Wieczorek MA, Nimmo F, Kiefer WS, Head JW, Huang C, Smith DE, Zuber MT (2016) Thicknesses of mare basalts on the Moon from gravity and topography. J Geophys Res Planets 121:854–870

Goossens S, Sabaka TJ, Wieczorek MA, Neumann GA, Mazarico E, Lemoine FG, Nicholas JB, Smith DE, Zuber MT (2020) High-resolution gravity field models from GRAIL data and implications for models of the density structure of the Moon's crust. J. Geophys Res Planets 125:e2019JE006086

Grimm RE (2013) Geophysical constraints on the lunar Procellarum KREEP Terrane. J Geophys Res Planets 118:768–777

Grimm RE (2018) New analysis of the Apollo 17 surface electrical properties experiment. Icarus 314:389–399

Grimm RE, Delory GT (2012) Next-generation electromagnetic sounding of the Moon. Adv Space Res 50:1687–1701

Grott M, Knollenberg J, Krause C (2010) Apollo lunar heat flow experiment revisited: A critical reassessment of the in situ thermal conductivity determination. J Geophys Res 115:E11005

Gulick SPS, Christeson GL, Barton PJ, Grieve RAF, Morgan JV, Urrutia-Fucugauchi J (2013) Geophysical characterization of the Chicxulub impact crater. Rev Geophys 51:31–52

Guo D, Liu J, Head III JW, Kreslavsky MA (2018) Orientale secondary craters: Insights into Orientale impact parameters and the largest secondary crater size of the South Pole-Aitken basin event. Lunar Planet Sci Conf 49:1866

Han S-C, Schmerr N, Neumann G, Holmes S (2014) Global characteristics of porosity and density stratification within the lunar crust from GRAIL gravity and Lunar Orbiter Laser Altimeter topography data. Geophys Res Lett 41:1882–1889

Harada Y, Goossens S, Matsumoto K, Yan J, Ping J, Noda H (2014) Strong tidal heating in an ultralow-viscosity zone at the core–mantle boundary of the Moon. Nat Geosci 7:569–572

Harada Y, Goossens S, Matsumoto K, Yan J, Ping J, Noda H, Haruyama J (2016) The deep lunar interior with a low-viscosity zone: Revised constraints from recent geodetic parameters on the tidal response of the Moon. Icarus 276:96–101

Hartmann WK, Kuiper GP (1962) Concentric structures surrounding lunar basins. Commun Lunar Planet Lab 1:51–66

Haruyama J, Hioki K, Shirao M, Morota T, Hiesinger H, van der Bogert CH, Miyamoto H, Iwasaki A, Yokota Y, Ohtake M, Matsunaga T, Hara S, Nakanotani S, Pieters CM (2009) Possible lunar lava tube skylight observed by SELENE cameras. Geophys Res Lett 36:L21206

Haskin LA (1998) The Imbrium impact event and the thorium distribution at the lunar highlands surface. J Geophys Res 103:1679–1689

Hauber E, Grott M, Kronberg P (2010) Martian rifts: Structural geology and geophysics. Earth Planet Sci Lett 294:393–410

Hawke BR (2003) Distribution and modes of occurrence of lunar anorthosite. J Geophys Res 108:5050

Head III JW (1974) Orientale multi-ringed basin interior and implications for petrogenesis of lunar highland samples. Moon 11:327–356

Head III JW (1977) Origin of outer rings in lunar multi-ringed basins: Evidence from morphology and ring spacing, *In:* Roddy DJ, Pepin RO, Merrill RB (eds) Impact and Explosion Cratering, Pergamon Press, p 563–573

Head JW, Wilson L (1992) Lunar mare volcanism: Stratigraphy, eruption conditions, and the evolution of secondary crusts. Geochim Cosmochim Acta 56:2155–2175

Head III JW, Wilson L (2017) Generation, ascent and eruption of magma on the Moon: New Insights into source depths, magma supply, intrusions and effusive/explosive eruptions (Part 2: Predicted emplacement processes and observations). Icarus 283:146–175

Head III JW, Wilson L, Hiesinger H, van der Bogert C, Chen Y, Dickson JL, Gaddis LR, Haruyama J, Jawin ER, Jozwiak LM, Li C, Liu J, Morota T, Needham DH, Ostrach LR, Pieters CM, Prissel TC, Qian Y, Qiao L, Rutherford MR, Scott DR, Whitten JL, Xiao L, Zhang F, Ziyuan O (2023) Lunar mare basaltic volcanism: Volcanic features and emplacement processes. Rev Mineral Geochem 89:453–507

Hess PC, Parmentier EM (1995) A model for the thermal and chemical evolution of the Moon's interior: implications for the onset of mare volcanism. Earth Planet Sci Lett 134:501–514

Hess PC, Parmentier EM (2001) Thermal evolution of a thicker KREEP liquid layer. J Geophys Res 106:28023–28032

Hiesinger H, Head III JW, Wolf U, Jaumann R, Neukum G (2003) Ages and stratigraphy of mare basalts in Oceanus Procellarum, Mare Nubium, Mare Cognitum, and Mare Insularum. J Geophys Res 108:5065

Hiesinger H, Head III JW, Wolf U, Jaumann R, Neukum G (2010) Ages and stratigraphy of lunar mare basalts in Mare Frigoris and other nearside maria based on crater size–frequency distribution measurements. J Geophys Res 115:E03003

Hiesinger H, Head III JW, Wolf U, Jaumann R, Neukum G (2011) Ages and stratigraphy of lunar mare basalts: A synthesis. Geol Soc Amer Spec Pap 477:1–51

Hood LL (1986) Geophysical constraints on the lunar interior. *In*: Origin of the Moon, Hartmann WK, Phillips RJ, Taylor GJ (eds), p 361–410

Hood LL (2011) Central magnetic anomalies of Nectarian-aged lunar impact basins: Probable evidence for an early core dynamo. Icarus 211:1109–1128

Hood LL, Sonett CP (1982) Limits on the lunar temperature profile. Geophys Res Lett 9:37–40

Hood LL, Herbert F, Sonnett CP (1982) The deep lunar electrical conductivity profile: Structural and thermal inferences. J Geophys Res 87:5311–5326

Hood L, Mitchell L, Lin P, Acuna H (1999) Initial measurements of the lunar induced magnetic dipole moment using Lunar Prospector magnetometer data. Geophys Res Lett 26:2327–2330

Huang Q, Wieczorek MA (2012) Density and porosity of the lunar crust from gravity and topography. J Geophys Res 117:E05003

Hurwitz DM, Kring DA (2014) Differentiation of the South Pole-Aitken basin impact melt sheet: Implications for lunar exploration. J Geophys Res Planets 119:1110–1133
Hurwitz DM, Head JW, Hiesinger H (2013) Lunar sinuous rilles: Distribution, characteristics, and implications for their origin. Planet Space Sci 79–80:1–38
James PB, Smith DE, Byrne PK, Kendall JD, Melosh HJ, Zuber MT (2019) Deep Structure of the Lunar South Pole-Aitken Basin. Geophys Res Lett 46:5100–5106
Jansen JC, Andrews-Hanna JC, Li Y, Lucey PG, Taylor GJ, Goossens S, Lemoine FG, Mazarico E, Head JW, Milbury C, Kiefer WS, Soderblom JM, Zuber MT (2017) Small-scale density variations in the lunar crust revealed by GRAIL. Icarus 291:107–123
Jansen JC, Andrews-Hanna JC, Milbury C, Head JW, Li Y, Melosh HJ, Zuber MT (2019) Radial gravity anomalies associated with the ejecta of the Orientale Basin. Icarus 319:444–458
Jeffreys H (1915) Certain hypotheses as to the internal structure of the Earth and Moon. Mem R Astron Soc 60:187–217
Jeffreys H (1937) On the figure of the Earth and Moon. Geophys J 4:1–13
Jeffreys H (1948) The figures of the Earth and Moon (Third Paper). Geophys J 5:219–247
Jeffreys H (1961) On the figure of the Moon. Mon Not R Astron Soc 122:421–432
Jeffreys H (1976) The Earth: Its Origin, History, And Physical Constitution. Cambridge University Press
Jianguo Y, Jinsong P, Fei L, Jianfeng C, Qian H, Lihe F (2010) Chang'E-1 precision orbit determination and lunar gravity field solution. Adv Space Res 46:50–57
Johnson BC, Blair DM, Collins GS, Melosh HJ, Freed AM, Taylor GJ, Head III JW, Wieczorek MA, Andrews-Hanna JC, Nimmo F, Keane JT, Miljković K, Soderblom JM, Zuber MT (2016) Formation of the Orientale lunar multiring basin. Science 354:441–444
Jolliff BL, Gillis JJ, Haskin LA, Korotev RL, Wieczorek MA (2000) Major lunar crustal terranes: Surface expressions and crust–mantle origins. J Geophys Res 105:4197–4216
Jozwiak LM, Head III JW, Wilson L (2015) Lunar floor-fractured craters as magmatic intrusions: Geometry, modes of emplacement, associated tectonic and volcanic features, and implications for gravity anomalies. Icarus 248:424–447
Jutzi M, Asphaug E (2011) Forming the lunar farside highlands by accretion of a companion moon. Nature 476:69–72
Kaku T, Haruyama J, Miyake W, Kumamoto A, Ishiyama K, Nishibori T, Yamamoto K, Crites ST, Michikami T, Yokota Y, Sood R, Melosh HJ, Chappaz L, Howell KC (2017) Detection of intact lava tubes at Marius Hills on the Moon by SELENE (Kaguya) lunar radar sounder. Geophys Res Lett 44:10,155–10,161
Kamata S, Sugita S, Abe Y, Ishihara Y, Harada Y, Morota T, Namiki N, Iwata T, Hanada H, Araki H, Matsumoto K, Tajika E (2013) Viscoelastic deformation of lunar impact basins: Implications for heterogeneity in the deep crustal paleo-thermal state and radioactive element concentration. J Geophys Res Planets 118:398–415
Kamata S, Sugita S, Abe Y, Ishihara Y, Harada Y, Morota T, Namiki N, Iwata T, Hanada H, Araki H, Matsumoto K, Tajika E, Kuramoto K, Nimmo F (2015) The relative timing of Lunar Magma Ocean solidification and the Late Heavy Bombardment inferred from highly degraded impact basin structures. Icarus 250:492–503
Karato S (2013) Geophysical constraints on the water content of the lunar mantle and its implications for the origin of the Moon. Earth Planet Sci Lett 384:144–153
Kattoum YN, Andrews-Hanna JC (2013) Evidence for ring-faults around the Orientale basin on the Moon from gravity. Icarus 226:694–707
Kawamura T, Kobayashi N, Tanaka S, Lognonné P (2015) Lunar Surface Gravimeter as a lunar seismometer: Investigation of a new source of seismic information on the Moon. J Geophys Res Planets 120:343–358
Kawamura T, Lognonné P, Nishikawa Y, Tanaka S (2017) Evaluation of deep moonquake source parameters: Implication for fault characteristics and thermal state. J Geophys Res Planets 122:1487–1504
Keane JT, Matsuyama I (2014) Evidence for lunar true polar wander and a past low-eccentricity, synchronous lunar orbit. Geophys Res Lett 41:6610–6619
Khan A, Mosegaard K (2002) An inquiry into the lunar interior: A nonlinear inversion of the Apollo lunar seismic data. J Geophys Res 107:5036
Khan A, Mosegaard K, Rasmussen KL (2000) A new seismic velocity model for the Moon from a Monte Carlo inversion of the Apollo lunar seismic data. Geophys Res Lett 27:1591–1594
Khan A, Connolly JAD, Olsen N, Mosegaard K (2006) Constraining the composition and thermal state of the moon from an inversion of electromagnetic lunar day-side transfer functions. Earth Planet Sci Lett 248:579–598
Khan A, Connolly JAD, Maclennan J, Mosegaard K (2007) Joint inversion of seismic and gravity data for lunar composition and thermal state. Geophys J Int 168:243–258
Khan A, Connolly JAD, Pommier A, Noir J (2014) Geophysical evidence for melt in the deep lunar interior. J Geophys Res Planets 119:2197–2221
Kiefer WS (2013) Gravity constraints on the subsurface structure of the Marius Hills: The magmatic plumbing of the largest lunar volcanic dome complex. J Geophys Res Planets 118:733–745
Kiefer WS, Macke RJ, Britt DT, Irving AJ, Consolmagno GJ (2012) The density and porosity of lunar rocks. Geophys Res Lett 39:L07201

Kiefer WS, Taylor GJ, Andrews-Hanna JC, Head III JW, Jansen JC, Patrick J, Robinson KL, Wieczorek MA, Zuber MT (2016) The bulk density of the small lunar volcanos Gruithuisen Delta and Hansteen Alpha: Implications for volcano composition and petrogenesis. Lunar Planet Sci Conf 47:1722

Konopliv AS, Park RS, Yuan DN, Asmar SW, Watkins MM, Williams JG, Fahnestock E, Kruizinga G, Paik M, Strekalov D, Harvey N, Smith DE, Zuber MT (2014) High-resolution lunar gravity fields from the GRAIL primary and extended missions. Geophys Res Lett 41:1452–1458

Kopal Z (1965) Possible effects of convection on lunar moments of inertia. Icarus 4:173–176

Kopal Z (1967) The shape of the Moon, its internal structure, and moments of inertia. Proc R Soc London Ser A 296:254–265

Korotev RL (2000) The great lunar hot spot and the composition and origin of the Apollo mafic ("LKFM") impact-melt breccias. J Geophys Res 105:4317–4345

Korotev RL, Jolliff BL, Zeigler RA, Gillis JJ, Haskin LA (2003) Feldspathic lunar meteorites and their implications for compositional remote sensing of the lunar surface and the composition of the lunar crust. Geochim Cosmochim Acta 67:4895–4923

Kreslavsky MA, Head III JW (2012) New observational evidence of global seismic effects of basin-forming impacts on the Moon from lunar reconnaissance orbiter lunar orbiter laser altimeter data. J Geophys Res 117:E00H24

Kuskov OL, Kronrod VA, Kronrod EV (2014) Thermo-chemical constraints on the interior structure and composition of the lunar mantle. Phys Earth Planet Inter 235:84–95

Kuskov OL, Kronrod EV, Kronrod VA (2019) Geochemical constraints on the cold and hot models of the Moon's interior: 2—Three-layer mantle. Sol Syst Res 53:75–90

Lambeck K, Pullan S (1980) The lunar fossil bulge hypothesis revisited. Phys Earth Planet Inter 22:29–35

Laneuville M, Wieczorek MA, Breuer D, Tosi N (2013) Asymmetric thermal evolution of the Moon. J Geophys Res Planets 118:1435–1452

Langseth MG, Clark SP, Chute JL, Keihm SJ, Wechsler AE (1972) Heat-flow experiment *In*: Apollo 15 Preliminary Science Report, NASA SP-289, p 11-1–11-23

Langseth MG, Keihm SJ, Chute JL (1973) Heat flow experiment. *In*: Apollo 17 Preliminary Science Report, NASA SP-330, p 9-1–9-24

Langseth MG, Keihm SJ, Peters K (1976) Revised lunar heat-flow values. Proc Lunar Sci Conf 7:3143–3171

Laplace PS (1798) "On the motion of the Moon about its centre of gravity." Chapter 2 *In:* Celestial Mechanics, Book 5. Hillard, Gray, Little, Wilkins (eds) Translated by N. Bowditch in 1839, Boston

Lawrence DJ, Feldman WC, Barraclough BL, Binder AB, Elphic RC, Maurice S, Thomsen DR (1998) Global elemental maps of the moon: the Lunar Prospector gamma-ray spectrometer. Science 281:1484–1489

Le Bars M, Wieczorek MA, Karatekin O, Cebron D, Laneuville M (2011) An impact-driven dynamo for the early Moon. Nature 479:215–218

Lin Y, Tronche EJ, Steenstra ES, van Westrenen W (2017a) Experimental constraints on the solidification of a nominally dry lunar magma ocean. Earth Planet Sci Lett 471:104–116

Lin Y, Tronche EJ, Steenstra ES, van Westrenen W (2017b) Evidence for an early wet Moon from experimental crystallization of the lunar magma ocean. Nat Geosci 10:14–18

Lock SJ, Stewart ST, Petaev MI, Leinhardt Z, Mace MT, Jacobsen SB, Ćuk M (2018) The origin of the Moon within a terrestrial synestia. J Geophys Res Planets 123:910–951

Lognonné P, Gagnepain-Beyneix J, Chenet H (2003) A new seismic model of the Moon: Implications for structure, thermal evolution and formation of the Moon. Earth Planet Sci Lett 211:27–44

Lognonné P, Johnson CL (2015) Planetary seismology. *In*: Schubert GBT, Treatise on Geophysics. Elsevier, Oxford, p 65–120

Lognonné P, Mosser B (1993) Planetary seismology. Surv Geophys 14:239–302

Loper DE (2002) On lunar asymmetries 1. Tilted convection and crustal asymmetry. J Geophys Res 107(E6):5046

Mallik A, Ejaz T, Shcheka S, Garapic G (2019) A petrologic study on the effect of mantle overturn: Implications for evolution of the lunar interior. Geochim Cosmochim Acta 250:238–250

Martinot M, Flahaut J, Besse S, Quantin-Nataf C, van Westrenen W (2018) Compositional variations in the vicinity of the lunar crust–mantle interface from Moon Mineralogy Mapper data. J Geophys Res Planets 123:3220–3237

Matsumoto K, Yamada R, Kikuchi F, Kamata S, Ishihara Y, Iwata T, Hanada H, Sasaki S (2015) Internal structure of the Moon inferred from Apollo seismic data and selenodetic data from GRAIL and LLR. Geophys Res Lett 42:7351–7358

Matsuyama I (2013) Fossil figure contribution to the lunar figure. Icarus 222:411–414

Matsuyama I, Manga M (2010) Mars without the equilibrium rotational figure, Tharsis, and the remnant rotational figure. J Geophys Res Planets 115:E12020

Matsuyama I, Nimmo F, Keane JT, Chan NH, Taylor GJ, Wieczorek MA, Kiefer WS, Williams JG (2016) GRAIL, LLR, and LOLA constraints on the interior structure of the Moon. Geophys Res Lett 43:8365–8375

Maurice M, Tosi N, Samuel H, Plesa A-C, Hüttig C, Breuer D (2017) Onset of solid-state mantle convection and mixing during magma ocean solidification. J Geophs Res Planets 122:577–598

Maurice M, Tosi N, Schwinger S, Breuer D, Kleine T (2020) A long-lived magma ocean on a young Moon. Sci Adv 6:eaba8949

Melosh HJ, Freed AM, Johnson BC, Blair DM, Andrews-Hanna JC, Neumann GA, Phillips RJ, Smith DE, Solomon SC, Wieczorek MA, Zuber MT (2013) The origin of lunar mascon basins. Science 340:1552–1556

Melosh HJ, Kendall J, Horgan B, Johnson BC, Bowling T, Lucey PG, Taylor GJ (2017) South Pole–Aitken basin ejecta reveal the Moon's upper mantle. Geology 45:1063–1066

Meyer J, Elkins-Tanton L, Wisdom J (2010) Coupled thermal-orbital evolution of the early Moon. Icarus 208:1–10

Michaut C, Pinel V (2018) Magma ascent and eruption triggered by cratering on the Moon. Geophys Res Lett 45:6408–6416

Milbury C, Johnson BC, Melosh HJ, Collins GS, Blair DM, Soderblom JM, Nimmo F, Bierson CJ, Phillips RJ, Zuber MT (2015) Preimpact porosity controls the gravity signature of lunar craters. Geophys Res Lett 42:9711–9716

Miljković K, Wieczorek MA, Collins GS, Laneuville M, Neumann GA, Melosh HJ, Solomon SC, Phillips RJ, Smith DE, Zuber MT (2013) Asymmetric distribution of lunar impact basins caused by variations in target properties. Science 342:724–726

Miljković K, Wieczorek MA, Collins GS, Solomon SC, Smith DE, Zuber MT (2015) Excavation of the lunar mantle by basin-forming impact events on the Moon. Earth Planet Sci Lett 409:243–251

Mimoun D, Wieczorek MA, Alkalai L, Banerdt WB, Baratoux D, Bougeret J-L, Bouley S, Cecconi B, Falcke H, Flohrer J, Garcia RF, Grimm R, Grott M, Gurvits L, Jaumann R, Johnson CL, Knapmeyer M, Kobayashi N, Konovalenko A, Lawrence D, Le Feuvre M, Lognonné P, Neal CR, Oberst J, Olsen N, Röttgering H, Spohn T, Vennerstrom S, Woan G, Zarka P (2012) Farside explorer: unique science from a mission to the farside of the moon. Exp Astron 33:529–585

Mohit PS, Phillips RJ (2006) Viscoelastic evolution of lunar multiring basins. J Geophys Res 111:E12001

Morbidelli A, Marchi S, Bottke WF, Kring DA (2012) A sawtooth-like timeline for the first billion years of lunar bombardment. Earth Planet Sci Lett 355–356:144–151

Moriarty DP, Watkins RN, Valencia SN, Kendall JD, Evans AJ, Dygert N, Petro NE (2021) Evidence for a stratified upper mantle preserved within the South Pole–Aitken Basin. J Geophys Res Planets 121:e2020JE006589

Muller PM, Sjogren WL (1968) Mascons: lunar mass concentrations. Science 161:680–684

Nagihara S, Hedlund M, Zacny K, Taylor PT (2014) Improved data reduction algorithm for the needle probe method applied to in-situ thermal conductivity measurements of lunar and planetary regoliths. Planet Space Sci 92:49–56

Nagihara S, Kiefer WS, Taylor PT, Williams DR, Nakamura Y (2018) Examination of the long-term subsurface warming observed at the Apollo 15 and 17 sites utilizing the newly restored heat flow experiment data from 1975 to 1977. J Geophys Res Planets 123:1125–1139

Nahm AL, Öhman T, Kring DA (2013) Normal faulting origin for the Cordillera and Outer Rook rings of Orientale basin, the Moon. J. Geophys. Res Planets 118:190–205

Nahm AL, Watters TR, Johnson CL, Banks ME, van der Bogert CH, Weber RC, Andrews-Hanna JC (2023) Tectonics of the Moon. Rev Mineral Geochem 89:691–727

Nakamura Y (1983) Seismic velocity structure of the lunar mantle. J Geophys Res 88:677–686

Nakamura Y (2003) New identification of deep moonquakes in the Apollo lunar seismic data. Phys Earth Planet Inter 139:197–205

Nakamura Y (2005) Farside deep moonquakes and deep interior of the Moon. J Geophys Res 110:E01001

Nakamura Y (2011) Timing problem with the Lunar Module impact data as recorded by the LSPE and corrected near-surface structure at the Apollo 17 landing site. J Geophys Res Planets 116:E12005

Nakamura Y, Latham G, Lammlein D, Ewing M (1974) Deep lunar interior inferred from recent seismic data. Geophys Res Lett 1:137–140

Nakamura Y, Latham GV, Dorman HJ (1982) Apollo lunar seismic experiment - Final summary. Proc Lunar Planet Sci Conf 13. J Geophys Res 87:A117–A123

Nakamura R, Matsunaga T, Ogawa Y, Yamamoto S, Hiroi T, Saiki K, Hirata N, Arai T, Kitazato K, Takeda H, Sugihara T, Kodama S, Ohtake M, Haruyama J, Yokota Y (2009) Ultramafic impact melt sheet beneath the South Pole-Aitken basin on the Moon. Geophys Res Lett 36:7–11

Nakamura R, Yamamoto S, Matsunaga T, Ishihara Y, Morota T, Hiroi T, Takeda H, Ogawa Y, Yokota Y, Hirata N, Ohtake M, Saiki K (2012) Compositional evidence for an impact origin of the Moon's Procellarum basin. Nat Geosci 5:775–778

Namiki N, Iwata T, Matsumoto K, Hanada H, Noda H, Goossens S, Ogawa M, Kawano N, Asari K, Tsuruta S, Ishihara Y, Liu Q, Kikuchi F, Ishikawa T, Sasaki S, Aoshima C, Kurosawa K, Sugita S, Tadashi T (2009) Farside gravity field of the Moon. Science 323:900–905

Neal CR, Banerdt WB, Beghein C, Chi P, Currie D, Del'Agnello S, Garrick-Bethell I, Grimm R, Grott M, Haviland H, Kedar S, Nagihara S, Panning M, Petro N, Schmerr N, Siegler M, Weber R, Wieczorek M, Zacny K (2019) The Lunar Geophysical Network Mission. Lunar Planet Sci Conf 50:2455

Neal CR, Banerdt WB, Beghein C, Bergman D, Chi P, Currie D, Dell'Agnello S, Delory D, Espley J, Garcia R, Garrick-Bethell I, Grimm R, Grott M, Haviland H, Indyk S, Johnson C, Kawamura T, Kedar S, Lognonne P, Nagihara S, Nakamura Y, Nunn C, Ostrach L, Panning M, Petro N, Schmerr N, Siegler M, Watters T, Wellnitz D, Wieczorek M, Williams J, Wu C, Zacny K, Adams M, Cardif E, Ginyard A, Hughes K, Jerry C, Jones A, Lynch R, Nicoletti A, Palace D, Parsay K, Rakow G, Sarli B, Segura M, Spitzer T, Steinfeld D, Zuby J (2020) LGN Decadal Study Final Report, https://science.nasa.gov/files/science-pink/s3fs-public/atoms/files/Lunar%20Geophysical%20Network.pdf

Neumann GA, Zuber MT, Smith DE, Lemoine FG (1996) The lunar crust: Global structure and signature of major basins. J Geophys Res 101:16,841–16,843

Neumann GA, Zuber MT, Wieczorek MA, McGovern PJ, Lemoine FG, Smith DE (2004) Crustal structure of Mars from gravity and topography. J Geophys Res 109:E08002

Neumann GA, Zuber MT, Wieczorek MA, Head III JW, Baker DMH, Solomon SC, Smith DE, Lemoine FG, Mazarico E, Sabaka TJ, Goossens SJ, Melosh HJ, Phillips RJ, Asmar SW, Konopliv AS, Williams JG, Sori MM, Soderblom JM, Miljković K, Andrews-Hanna JC, Nimmo F, Kiefer WS (2015) Lunar impact basins revealed by Gravity Recovery and Interior Laboratory measurements. Sci Adv 1:e1500852

Nimmo F, Faul UH, Garnero EJ (2012) Dissipation at tidal and seismic frequencies in a melt-free Moon. J Geophys Res 117:E09005

Ohtake M, Matsunaga T, Haruyama J, Yokota Y, Morota T, Honda C, Ogawa Y, Torii M, Miyamoto H, Arai T, Hirata N, Iwasaki A, Nakamura R, Hiroi T, Sugihara T, Takeda H, Otake H, Pieters CM, Saiki K, Kitazato K, Abe M, Asada N, Demura H, Yamaguchi Y, Sasaki S, Kodama S, Terazono J, Shirao M, Yamaji A, Minami S, Akiyama H, Josset J-L (2009) The global distribution of pure anorthosite on the Moon. Nature 461:236–240

Ojakangas GW, Stevenson DJ (1989) Polar wander of an ice shell on Europa. Icarus 241:220–241

Ono T, Kumamoto A, Nakagawa H, Yamaguchi Y, Oshigami S, Yamaji A, Kobayashi T, Kasahara Y, Oya H (2009) Lunar radar sounder observations of subsurface layers under the nearside maria of the Moon. Science 323:909–912

Osinski GR, Melosh HJ, Andrews-Hanna J, Baker D, Denevi B, Dhingra D, Ghent R, Hayne PO, Hill P, James PB, Jaret S, Johnson B, Kenkmann T, Kring D, Mahanti P, Minton D, Neish CD, Neumann G, Plescia J, Potter RWK, Richardson J, Silber EA, Soderblom JM, Zanetti M, Zellner N (2023) Lunar impact features and processes. Rev Mineral Geochem 89:339–371

Parmentier EM, Zhong S, Zuber MT (2002) Gravitational differentiation due to initial chemical stratification: Origin of lunar asymmetry by the creep of dense KREEP? Earth Planet Sci Lett 201:473–480

Peeples WJ, Sill WR, May TW, Ward SH, Phillips RJ, Jordan RL, Abbott EA, Killpack TJ (1978) Orbital radar evidence for lunar subsurface layering in Maria Serenitatis and Crisium. J Geophys Res Solid Earth 83:3459–3468

Petro NE, Pieters CM (2008) The lunar-wide effects of basin ejecta distribution on the early megaregolith. Meteorit Planet Sci 43:1517–1529

Phillips RJ, Adams GF, Brown WE, Eggleton RE, Jackson P, Jordan R, Linlor WI, Peeples WJ, Porcello LJ, Ryu J, Schaber G, Sill WR, Thompson TW, Ward SH, Zelenka JS (1973) Apollo Lunar Sounder Experiment. *In*: Apollo 17 Preliminary Science Report, NASA-SP-330, p 22-1–22-26

Ping J, Huang Q, Yan J, Cao J, Tang G, Shu R (2009) Lunar topographic model CLTM-s01 from Chang'E-1 laser altimeter. Sci China Ser G Physics Mech Astron 52:1105–1114

Porco CC, Baker E, Barbara J, Beurle K, Brahic A, Burns JA, Charnoz S, Cooper N, Dawson DD, Del Genio AD, Denk T, Dones L, Dyudina U, Evans MW, Giese B, Grazier K, Helfenstein P, Ingersoll AP, Jacobson RA, Johnson TV, McEwen A, Murray CD, Neukum G, Owen WM, Perry J, Roatsch T, Spitale J, Squyres S, Thomas PC, Tiscareno M, Turtle E, Vasavada AR, Veverka J, Wagner R, West R (2005) Cassini Imaging Science: Initial results on Phoebe and Iapetus. Science 307:1237–1242.

Potter RWK, Kring DA, Collins GS, Kiefer WS, Mcgovern PJ (2012) Estimating transient crater size using the crustal annular bulge: Insights from numerical modeling of lunar basin-scale impacts. Geophys Res Lett 39:L18203

Potter RWK, Kring DA, Collins GS, Kiefer WS, Mcgovern PJ (2013) Numerical modeling of the formation and structure of the Orientale impact basin. J Geophys Res 118:963–979

Potter RWK, Head III JW, Guo D, Liu J, Xiao L (2018) The Apollo peak-ring impact basin: Insights into the structure and evolution of the South Pole–Aitken basin. Icarus 306:139–149

Pritchard ME, Stevenson DJ (2000) Thermal aspects of a lunar origin by giant impact. *In*: Origin of the Earth and Moon. Canup RM, Richter K (eds) University of Arizona Press, p 179–196

Qin C, Muirhead AC, Zhong S (2012) Correlation of deep moonquakes and mare basalts: Implications for lunar mantle structure and evolution. Icarus 220:100–105

Qin C, Zhong S, Phillips R (2018) Formation of the lunar fossil bulges and its implication for the early Earth and Moon. Geophys Res Lett 45:1286–1296

Rapp JF, Draper DS (2018) Fractional crystallization of the lunar magma ocean: Updating the dominant paradigm. Meteorit Planet Sci 53:1432–1455

Rasmussen KL, Warren PH (1985) Megaregolith thickness, heat flow, and the bulk composition of the Moon. Nature 313:121–124

Reindler L (2001) The compensation state of intermediate size lunar craters. Icarus 153:71–88

Ricard Y (2007) Physics of mantle convection. Treatise Geophys 7:31–87

Robinson MS, Ashley JW, Boyd AK, Wagner RV, Speyerer EJ, Ray Hawke B, Hiesinger H, van der Bogert CH (2012) Confirmation of sublunarean voids and thin layering in mare deposits. Planet Space Sci 69:18–27

Robuchon G, Choblet G, Tobie G, Čadek O, Sotin C, Grasset O (2010) Coupling of thermal evolution and despinning of early Iapetus. Icarus 207:959–971

Roy A, Wright JT, Sigurðsson S (2014) Earthshine on a young Moon: Explaining the lunar Farside Highlands. Astrophys J 788:L42

Rufu R, Aharonson O, Perets HB (2017) A multiple-impact origin for the Moon. Nat Geosci 10:89–94

Runcorn SK (1967) Convection in the Moon and the existence of a lunar core. Proc R Soc London Ser A 296:270–284

Runcorn SK (1983) Lunar magnetism, polar displacements and primeval satellites in the Earth–Moon system. Nature 304:589–596
Saal AE, Hauri EH, Cascio ML, Van Orman JA, Rutherford MC, Cooper RF (2008) Volatile content of lunar volcanic glasses and the presence of water in the Moon's interior. Nature 454:192–195
Salmon J, Canup RM (2012) Lunar accretion from a roche-interior fluid disk. Astrophys J 760:83
Salmon J, Canup RM (2014) Accretion of the Moon from non-canonical discs. Phil Trans R Soc A 372:20130256
Scheinberg A, Soderlund KM, Schubert G (2015) Magnetic field generation in the lunar core : The role of inner core growth. Icarus 254:62–71
Schubert G, Lichtenstein BR, Coleman PJ, Russell CT (1974) Simultaneous Explorer 35 and Apollo 15 orbital magnetometer observations: Implications for lunar electrical conductivity inversions. J Geophys Res 79:2007–2013
Schultz PH (1976) Floor-fractured lunar craters. Moon 15:241–273
Sedgwick WF (1898) On the oscillations of a heterogeneous compressible liquid sphere and the genesis of the Moon; and on the figure of the Moon. Messenger Math 27:159–173
Shearer C, Neal CR, Glotch TD, Prissel TC, Bell AS, Assis Fernandes V, Gaddis LR, Jolliff BL, Laneuville M, Magna T, Simon J (2023) Magmatic evolution II: A new view of post-differentiation magmatism. Rev Mineral Geochem 89:147–205
Shimizu H, Matsushima M, Takahashi F, Shibuya H, Tsunakawa H (2013) Constraint on the lunar core size from electromagnetic sounding based on magnetic field observations by an orbiting satellite. Icarus 222:32–43
Siegler MA, Smrekar SE (2014) Lunar heat flow: Regional prospective of the Apollo landing sites. J Geophys Res Planets 119:47–63
Siegler MA, Miller RS, Keane JT, Laneuville M, Paige DA, Matsuyama I, Lawrence DJ, Crotts A, Poston MJ (2016) Lunar true polar wander inferred from polar hydrogen. Nature 531:480–484
Sjogren WL, Smith JC (1976) Quantitative mass distribution models for Mare Orientale. Proc Lunar Sci Conf 7:2639–2648
Smith DE, Zuber MT, Neumann GA, Lemoine FG, Mazarico E, Torrence MH, McGarry JF, Rowlands DD, Head III JW, Duxbury TH, Aharonson O, Lucey PG, Robinson MS, Barnouin OS, Cavanaugh JF, Sun X, Liiva P, Mao DD, Smith JC, Bartels AE (2010) Initial observations from the Lunar Orbiter Laser Altimeter (LOLA). Geophys Res Lett 37:L18204
Snyder GA, Taylor A, Neal CR (1992) A chemical model for generating the sources of mare basalts : Combined equilibrium and fractional crystallization of the lunar magmasphere. Geochim Cosmochim Acta 56:3809–3823
Soderblom JM, Evans AJ, Johnson BC, Melosh HJ, Miljković K, Phillips RJ, Andrews-Hanna JC, Bierson CJ, Head III JW, Milbury C, Neumann GA, Nimmo F, Smith DE, Solomon SC, Sori MM (2015) The fractured Moon: Production and saturation of porosity in the lunar highlands from impact cratering. Geophys Res Lett 42:6939–6944
Solomon SC (1977) The relationship between crustal tectonics and internal evolution in the Moon and Mercury. Phys Earth Planet Inter 15:135–145
Solomon SC, Chaiken J (1976) Thermal expansion and thermal stresses in the Moon and terrestrial planets. Lunar Sci Conf 7:825–827
Solomon SC, Head III JW (1979) Vertical movement in mare basins: Relation to mare emplacement, basin tectonics, and lunar thermal history. J Geophys Res 84:1667–1682
Solomon SC, Head III JW (1980) Lunar mascon basins—Lava filling, tectonics, and evolution of the lithosphere. Rev Geophys Space Phys 18:107–141
Sonett CP (1982) Electromagnetic induction in the Moon. Rev Geophys Space Phys 20:411–455
Sonnett CP, Smith BF, Colburn DS, Schubert G, Schwartz K (1972) The induced magnetic field of the Moon: Conductivity profiles and inferred temperature. Proc Lunar Sci Conf 3:2309–2336
Sood R, Chappaz L, Melosh HJ, Howell KC, Milbury C, Blair DM, Zuber MT (2017) Detection and characterization of buried lunar craters with GRAIL data. Icarus 289:157–172
Sori MM, Zuber MT, Head JW, Kiefer WS (2016) Gravitational search for cryptovolcanism on the Moon: Evidence for large volumes of early igneous activity. Icarus 273:284–295
Spera FJ (1992) Lunar magma transport phenomena. Geochim Cosmochim Acta 56:2253–2265
Spohn T (2001) The longevity of lunar volcanism: Implications of thermal evolution calculations with 2D and 3D mantle convection models. Icarus 149:54–65
Stegman DR, Jellinek AM, Zatman SA, Baumgardner JR, Richards MA (2003) An early lunar core dynamo driven by thermochemical mantle convection. Nature 421:143–146
Stevenson DJ (1980) Lunar asymmetry and paleomagnetism. Nature 287:520–521
Stewart ST (2012) Impact basin formation and structure from 3D simulations. Lunar Planet Sci Conf 43:2865.
Takahashi F, Tsunakawa H, Shimizu H, Shibuya H, Matsushima M (2014) Reorientation of the early lunar pole. Nat Geosci 7:409–412
Taylor GJ, Wieczorek MA (2014) Lunar bulk chemical composition: a post-gravity recovery and interior laboratory reassessment. Phil Trans R Soc A 372:20130242
Thorey C, Michaut C, Wieczorek M (2015) Gravitational signatures of lunar floor-fractured craters. Earth Planet Sci Lett 424:269–279
Tian Z, Wisdom J, Elkins-Tanton L (2017) Coupled orbital-thermal evolution of the early Earth–Moon system with a fast-spinning Earth. Icarus 281:90–102

Tikoo SM, Weiss BP, Shuster DL, Suavet C, Wang H, Grove TL (2017) A two-billion-year history for the lunar dynamo. Sci Adv 3:e1700207

Toksöz, MN (1975) Lunar and planetary seismology. Rev Geophys 13:306–311

Toksöz MN (1979) Planetary seismology and interiors. Rev Geophys Space Phys 17:1641–1655

Toksöz MN, Anderson K, Dainty AM, Latham G, Ewing M, Dorman J, Lammlein D, Sutton G, Duennebier F, Nakamura Y (1972) Lunar crust: Structure and composition. Science 176:1012–1016

Toksöz MN, Dainty AM, Solomon SC, Anderson KR (1974) Structure of the Moon. Rev Geophys Space Phys 12:539–567

Tyburczy JA (2007) 2.21—Properties of rocks and minerals—The electrical conductivity of rocks, minerals and the Earth. *In*: Schubert G (ed) Treatise on Geophysics, Elsevier, Amsterdam, p 631–642

Uemoto K, Ohtake M, Haruyama J, Matsunaga T, Yamamoto S, Nakamura R, Yokota Y, Ishihara Y, Iwata T (2017) Evidence of impact melt sheet differentiation of the lunar South Pole-Aitken basin. J Geophys Res Planets 122:1672–1686, doi:10.1002/2016JE005209.

Vaughan WM, Head III JW (2014) Impact melt differentiation in the South Pole-Aitken basin: Some observations and speculations. Planet Space Sci 91:101–106

Vermeesch PM, Morgan JV (2008) Structural uplift beneath the Chicxulub impact structure. J Geophys Res 113:B07103

Warren PH, Rasmussen KL (1987) Megaregolith insulation, internal temperatures, and bulk uranium content of the Moon. J Geophys Res 92:3453–3465

Warren PH, Wasson JT (1979) The Origin of KREEP. Rev Geophys Space Phys 17:73–88

Wasson JT, Warren PH (1980) Contribution of the mantle to the lunar asymmetry. Icarus 44:752–771

Watters TR, Robinson MS, Beyer RA, Banks ME, Bell JF, Pritchard ME, Hiesinger H, van der Bogert CH, Thomas PC, Turtle EP, Williams NR (2010) Evidence of recent thrust faulting on the Moon revealed by the Lunar Reconnaissance Orbiter Camera. Science 329:936–940

Weber RC, Bills BG, Johnson CL (2009) Constraints on deep moonquake focal mechanisms through analyses of tidal stress. J Geophys Res 114:E05001

Weber RC, Lin P-Y, Garnero EJ, Williams Q, Lognonné P (2011) Seismic detection of the lunar core. Science 331, 309–312

Weber RC, Cohen B, Lawrence S, Boyce J, Collier M, Fassett C, Gaddis L, Gruener J, Heldmann J, Petro N, Young K, Fagan A, Gross J, Pieters C, Bleacher J, Draper D, McCubbin F, Mitchell J, Nahm A, Needham D, Noble S, Sato K, Spann J (2020) Artemis III Science Definition Team Report, NASA SP 20205009602, https://www.nasa.gov/sites/default/files/atoms/files/artemis-iii-science-definition-report-12042020c.pdf

Weiss BP, Tikoo SM (2014) The lunar dynamo. Science 346:1246753

Whitaker EA (1981) The lunar Procellarum basin. *In*: Schultz PH, Merrill RB (eds), Multi-Ring Basins, Pergamon, p 105–111

Whitten J, Head III JW, Staid M, Pieters CM, Mustard J, Clark R, Nettles J, Klima RL, Taylor L (2011) Lunar mare deposits associated with the Orientale impact basin: New insights into mineralogy, history, mode of emplacement, and relation to Orientale Basin evolution from Moon Mineralogy Mapper (M3) data from Chandrayaan-1. J Geophys Res 116:E00G09

Wieczorek MA (2018) Strength, depth, and geometry of magnetic sources in the crust of the Moon from localized power spectrum analysis. J Geophys Res Planets 123:291–316

Wieczorek MA, Phillips RJ (1998) Potential anomalies on a sphere: Applications to the thickness of the lunar crust. J Geophys Res 103:1715–1724

Wieczorek MA, Phillips RJ (1999) Lunar multiring basins and the cratering process. Icarus 139:246–259

Wieczorek MA, Phillips RJ (2000) The "Procellarum KREEP Terrane": Implications for mare volcanism and lunar evolution. J Geophys Res 105:20,417–20,430

Wieczorek MA, Weiss BP, Stewart ST (2012) An impactor origin for lunar magnetic anomalies. Science 335:1212–1215

Wieczorek MA, Neumann GA, Nimmo F, Kiefer WS, Taylor GJ, Melosh HJ, Phillips RJ, Solomon SC, Andrews-Hanna JC, Asmar SW, Konopliv AS, Lemoine FG, Smith DE, Watkins MM, Williams JG, Zuber MT (2013) The crust of the Moon as seen by GRAIL. Science 339:671–675

Wieczorek MA, Weiss BP, Breuer D, Cébron D, Fuller M, Garrick-Bethell I, Gattacceca J, Halekas JS, Hemingway DJ, Hood LL, Laneuville M, Nimmo F, Oran R, Purucker ME, Rückriemen T, Soderlund KM, Tikoo1 SM (2023) Lunar magnetism. Rev Mineral Geochem 89:207–241

Wilhelms D (1987) The Geologic History of the Moon, U.S. Geol Surv Prof Pap 13

Williams KK, Zuber MT (1998) Measurement and analysis of lunar basin depths from Clementine altimetry. Icarus 131:107–122

Williams JG, Konopliv AS, Boggs DH, Park RS, Yuan D-NN, Lemoine FG, Goossens S, Mazarico E, Nimmo F, Weber RC, Asmar SW, Melosh H, Neumann GA, Phillips RJ, Smith DE, Solomon SC, Watkins MM, Wieczorek MA, Andrews-Hanna JC, Head III JW, Kiefer WS, Matsuyama I, McGovern PJ, Taylor GJ, Zuber MT, Melosh HJ, Neumann GA, Phillips RJ, Smith DE, Solomon SC, Watkins MM, Wieczorek MA, Andrews-Hanna JC, Head III JW, Kiefer WS, Matsuyama I, McGovern PJ, Taylor GJ, Zuber MT (2014) Lunar interior properties from the GRAIL mission. J Geophys Res Planets 119:1546–1578

Wilson L, Head III JW (2017) Generation, ascent, and eruption of magma on the Moon: New insights into source depths, magma supply, intrusions and effusive/explosive eruptions (Part 1: Theory). Icarus 286:146–175

Yamada R, Garcia RF, Lognonné P, Kobayashi N, Takeuchi N, Nébut T, Shiraishi H, Calvet M, Ganepain-Beyneix J (2013) On the possibility of lunar core phase detection using new seismometers for soft-landers in future lunar missions. Planet Space Sci 81:18–31

Yamamoto S, Nakamura R, Matsunaga T, Ogawa Y, Ishihara Y, Morota T, Hirata N, Ohtake M, Hiroi T, Yokota Y, Haruyama J (2010) Possible mantle origin of olivine around lunar impact basins detected by SELENE. Nat Geosci 3:533–536

Yamamoto S, Nakamura R, Matsunaga T, Ogawa Y, Ishihara Y, Morota T, Hirata N, Ohtake M, Hiroi T, Yokota Y, Haruyama J (2012) Massive layer of pure anorthosite on the Moon. Geophys Res Lett 39:L13201

Zhang N, Parmentier EM, Liang Y (2013a) Effects of lunar cumulate mantle overturn and megaregolith on the expansion and contraction history of the Moon. Geophys Res Lett 40:5019–5023

Zhang N, Parmentier EM, Liang Y (2013b) A 3-D numerical study of the thermal evolution of the Moon after cumulate mantle overturn: The importance of rheology and core solidification. J Geophys Res Planets 118:1789–1804

Zhang N, Dygert NJ, Liang Y, Parmentier EM (2017) The effect of ilmenite viscosity on the dynamics and evolution of an overturned lunar cumulate mantle. Geophys Res Lett 44: 9216–9224

Zhao D, Arai T, Liu L, Ohtani E (2012) Seismic tomography and geochemical evidence for lunar mantle heterogeneity: Comparing with Earth. Glob Planet Change 91:29–36

Zhong S, Zuber MT (2000) Long-wavelength topographic relaxation for self-gravitating planets and implications for the time-dependent compensation of surface topography. J Geophys Res 105:4153–4164

Zhong S, Parmentier EM, Zuber MT (2000) A dynamic origin for the global asymmetry of lunar mare basalts. Earth Planet Sci Lett 177:131–140

Zhu M-H, Wünnemann K, Potter RWK, Kleine T, Morbidelli A (2019) Are the Moon's nearside–farside asymmetries the result of a giant impact? J Geophys Res Planets 124:2117–2140

Ziethe R, Seiferlin K, Hiesinger H (2009) Duration and extent of lunar volcanism : Comparison of 3D convection models to mare basalt ages. Planet Space Sci 57:784–796

Zuber MT, Smith DE, Lemoine FG, Neumann GA (1994) The shape and internal structure of the moon from the clementine mission. Science 266:1839–1843

Zuber MT, Smith DE, Neumann GA, Goossens S Zuber MT, Smith DE, Watkins MM, Asmar SW, Konopliv AS, Lemoine FG, Melosh HJ, Neumann GA, Phillips RJ, Solomon SC, Wieczorek MA, Williams JG, Goossens SJ, Kruizinga G, Mazarico E, Park RS, Yuan D-N (2013) Gravity field of the Moon from the Gravity Recovery and Interior Laboratory (GRAIL) Mission. Science 668:1–5

Zuber MT, Smith DE, Neumann GA, Goossens S, Andrews-Hanna JC, Head III JW, Kiefer WS, Asmar SW, Konopliv AS, Lemoine FG, Matsuyama I, Melosh HJ, Mcgovern PJ, Nimmo F, Phillips RJ, Solomon SC, Taylor GJ, Watkins MM, Wieczorek MA, Williams JG, Jansen JC, Johnson BC, Keane JT, Mazarico E, Miljković K, Park RS, Soderblom JM, Yuan D (2016) Gravity field of the Orientale basin from the Gravity Recovery and Interior Laboratory Mission. Science 354:438–444

ELECTRONIC ANNEX

Figures and tables referred to by the prefix "EA" are in an electronic annex available at https://apenninus.u-aizu.ac.jp/NVM2-EA.html